Wearable Sensor Scanner using Electrical Impedance Tomography

Yao, Yongjia

Award date:
2012

Awarding institution:
University of Bath

Wearable Sensor Scanner using Electrical Impedance Tomography

Yongjia (Allen) Yao

Department of Electronic & Electrical Engineering

University of Bath

A thesis submitted to the Department of Electronic & Electrical Engineering,

University of Bath, in fulfillment of the requirements for the degree of

Doctor of Philosophy in Electrical Engineering

Bath, September 2012

Declaration

I declare that this thesis is my own, unaided work. It is being submitted for the degree of Doctor of Philosophy in Electrical Engineering at the University of Bath. It has not been submitted before for any degree or examination at any other university.

Signature of Author…….

Bath, United Kingdom

26 September 2012

Abstract

Electrical impedance tomography (EIT) is an imaging system that can generate a map of electrical conductivity. The aim of this project is to develop a pressure mapping imaging device, which we also call Wearable Scanners using EIT (WSEIT) system. WSEIT are being developed based on electrical conductivity imaging of the conductive area generated in a fabric structure. This thesis demonstrates the application of conductive fabric as a pressure mapping imaging device together with the EIT imaging system. For the first time, multiple-deformation and pressure points are detected. This thesis will also show quantitative analysis of this pressure mapping imaging solution. We envisage a number of applications for WSEIT, especially in the areas of robotics and bio-mechanics. In this project, we are interested in measuring the pressure that has been applied to a 2D surface. There are three major parts to this project: the sensor design, the hardware electronics and, finally, tomographic image reconstruction. The sensors are elastomeric conductive areas that can be integrated in a number of ways into a garment. It will be shown that the conductivity of the area will change as the surface topology changes; as pressure is applied, the electrical impedances of the sensor area are measured from a number of peripheral points. The impedance data is then transferred to the image reconstruction software. Finally, the inversion technique is applied to the data to generate a pressure and deformation map of the body. The measurement system has been developed using a multiplexer circuit and a USB-based DAQ card, from National Instruments (NI). The performance of the EIT system was tested using traditional saline phantoms. Several different types of materials have been considered and tested for the design of fabric based pressure sensor.

To my beloved wife and parents

Acknowledgements

I would like to dedicate this work to my wife, Rachel Chen, both my parents, Yong Yao and Hongping Liang, and my parents-in-law, Liping Chen and Guoqing Lu. It would not have been possible without their love, support and encouragement.

I would also like to thank my core supervisor, Dr. Manuchehr Soleimani, for his friendship, ideas, guidance, and assistance throughout the entire study. I also wish to express my thanks to my secondary supervisor, Prof. Cathryn Mitchell, for her kindness and support.

Special thanks go to the research technicians from the Engineering & Design Technical Services Department: Jamie Lee, David Parker, and Andrew Matthews. The project would not have seen completion without the hardware support from them.

Finally, many thanks go to my research colleagues, Joe Kinrade, Julian Rose, Lu Ma, Hsinyu Wei, Qiu Wei, Chuanli Yang and Zhuoyi Ye. These four years of studying have been a greatly valuable and enjoyable experience because of your support.

Contents

List of Figures

List of Tables

List of Principal Symbols

A - Magnetic potential, which has the SI units of weber/ meter - (Wbm^{-1})

B - Magnetic field, which has the SI units of teslas - (T)

D - Electric displacement

E - Electric field, which has the SI units of volts/meter - (Vm^{-1})

L - Magnetic inductance, which has the sI units of henry - (H)

H - Magnetic field intensity, which has the SI units of amperes/meter - (Am^{-1})

J - Electric current density, which has the SI units of amperes/square meter - (Am^{-2})

ε - Electrical permittivity - (Fm^{-1})

μ - Electrical permeability - (Hm^{-1})

σ - Electrical conductivity - (Sm^{-1})

Acronyms

DAQ - Data Acquisition

ECT - Electrical Capacitance Tomography

EIT - Electrical Impedance Tomography

EMT - Electro-Magnetic Tomography

FEM - Finite Element Method

MIT - Magnetic induction Tomography

NI - National Instrument

SVD - Singular Value Decomposition

SNR - Signal-to-Noise Ratio

Chapter 1

1. Introduction

Electrical impedance tomography (EIT) is an imaging system that generates maps of electrical conductivity over a certain measuring area, which can be either in 2D or 3D. This thesis proposes the EIT imaging on a conductive fabric for pressure mapping imaging. The imaging of a conductive area in a garment can be potentially used to create a wearable scanner. One of the major advantages of an EIT system is that it does not require any wiring within the subject being measured; only measurements around the boundaries are required.

1.2 Background of EIT

In terms of history, EIT is a relatively mature imaging method, which has managed to draw interest from scientists from a wide range of disciplines[1]. This includes mathematicians with an interest in uniqueness proofs and inverse problems, physicists interested in bio-impedance, electronics engineers and clinicians with particular clinical problems, who are attracted by its unique portability, safety and low cost.

EIT is one member of a whole class of imaging techniques in which the common objective is to non-invasively determine certain physical parameters within a region

of interest. The common techniques include X-ray computed tomography, nuclear magnetic resonance imaging, B-scan ultrasound and positron emission tomography. A comprehensive comparative review of these methods was carried out by Bates in 1983[2].

Electrical impedance imaging began as an alternative for traditional imaging systems such as X-ray computed tomography, aimed to overcoming the disadvantages of being expensive and posing a biological hazard to the patient being imaged. The first attempt[3] was started by making the theoretical assumption that electric currents flow in straight lines, in the same manner that beams of X-rays[4] do. Since the initial attempt at impedance imaging, a whole range of image reconstruction techniques have been developed. The first successful EIT image was reported by Barber and Brown[5], who used the Sheffield mark 1 system[6] with a single frequency. A single frequency system provides only limited information regarding the electrical characteristics of the test object. Using alternating current for a certain range of frequencies would allow a more comprehensive probe of the object's properties[7]. One of the successors of the Sheffield mark 1 is the Sheffield mark 3.5, marketed by Maltron Inc. as the Pulmonary Scan mark 3.5. It is a multi-frequency, eight-electrode system, specifically designed for neonatal use, where the space available for electrodes is limited. It operates on frequencies in the range of 2 kHz to 1.6 MHz, which may enable tissue characterisation in the future. Its data collection speed is 25 frames per second. Signal-to-noise ratio was significantly reduced in comparison to the mark 1 version[8]. Another developed system is the *DSP Based Multi-Frequency 3D Electrical Impedance Tomography System* by M. Goharian from McMaster University, Canada[7]. This system operates in a way that is comparable to the Sheffield mark 1, but with substantial noise reduction[9]. The success in designing

better EIT systems resulted in a wave of enthusiasm and prototype systems were developed in more than ten different clinical areas. Successful pilot studies were carried out, which showed a good correlation with gold standard techniques in imaging lung ventilation. Over the next few years, new developments were made, such as imaging for breast cancer and brain function. Isaacson[10], back in 1992, published a review of these different techniques. Many of these remained theoretical methods until 1991, when *in vivo* images were produced. A more comprehensive study of the evolution of EIT can be found in Knight[11]. Compared to other tomography methods, EIT suffers from severe limitations that may prevent its adoption for routine medical diagnosis. For example, EIT is not suitable for anatomical imaging in the way that Magnetic Resonance Imaging (MRI) or Computed Tomography (CT) is due to its large variability of images between subjects. Also, its low spatial resolution and susceptibility to noise and electrode errors makes the matter even worse. However, EIT does show promise as a diagnostic tool for medical clinicians. It has the advantage of a low cost which, can save thousands of pounds, compared to the others like MRI and CT or even Positron Emission Tomography (PET)[12]. Furthermore, EIT is non-invasive and safe. Comparatively, when it comes to size, it is very small and portable. Thus, until this point, most of the applications for EIT were clinical-based, but since then, new directions for the technology, within industry, have been considered. The basic aim of modern tomography is to determine the distribution of materials in some region of interest by obtaining a set of measurements using sensors that are distributed around the periphery. Electrical tomography has motivated applications in process design and validation, online monitoring and control. This can, for instance, lead to improved product quality and process efficiency, accompanied by improved profits

through a reduction of time and waste. Typical fields of application in the early years of development included two-phase flow, fluidised beds, mixing and environmental monitoring[13-16]. In the next section, applications of EIT in each field will be discussed.

1.3 Electrical Impedance Tomography Applications

In general, electrical impedance tomography has three primary application fields:

- Industrial: The applications include pipeline fluid monitoring imaging, the measurement of fluid distribution in mixing vessels, and non-destructive testing such as crack detection[17, 18].
- Geophysical: The applications include geophysical prospecting, cross borehole measurement and surface measurement[19, 20].
- Medical: EIT is very widely studied in medical field for all sorts of monitoring purposes, for example, for monitoring lung and cardiac functions, measurement of brain function, detection of internal bleeding in tissue, measurement of gastric imaging, identification and classification of tumours in breast or brain tissue, and also thorax functional imaging[21-29].

1.3.1 Industrial Application

In industrial applications, process tomography uses EIT to image conducting fluids within vats or flowing within pipes[30] and capacitance tomography for dielectric material[31].

The aim of process imaging is to determine the distributions of quantities of interest so that inferences can be made on processes taking place in various environments such as pipes, tanks and vessels. It is typically used as a monitoring method in

inhomogeneities, chemical reactions, spatial and temporal concentration variations, as well as phase fractions in mass flows and various mixing and separation processes. Detailed examples have been discussed in [32-34].

1.3.2 Geophysical Application

For geophysical applications, it is typically used for obtaining core sample data, geophysical probing, i.e. mineral detection at the earth's surface, and borehole scanning. Some even apply the technique for groundwater contamination assessment[35]. One of the major points of applying EIT in this area is for imaging the inner structures of geological objects. Take rock, for example; its resistivity can vary by several orders of magnitude depending on the rock nature, porosity and water content. To do that, the EIT system in this field is normally equipped with an array of regularly spaced electrodes and the geometrical factor is usually calculated to quickly represent the apparent conductivities. In this way, it allows the control of data quality in the aftermath of their acquisition. The distance between electrodes defines the spatial resolution and the penetration depth. By standard, the spatial resolution of the method in geophysics is of the order of meters and the penetration depth can reach 500m.

1.3.3 Medical Application

EIT medical imaging is established on the fact that biological tissues can be recognised from their conductivity or permittivity[36, 37], which in turn vary according to its state of health as well as during physiological organ functioning[38]. This has been reported by investigators studying the applications of differences in the electrical properties of tumours for their clinical aspects. The electrical properties of malignant breast tumours have been investigated in [39] and [40] where the study

shows significantly higher permeability of the tumour tissue at 20 kHz compared to that of normal or non-malignant tissues. Others have come to similar conclusions like [41-44]. Another medical application of EIT in terms of bioimpedances is evaluation of the global states of biological systems, for example: cardiac and respiratory functions and quantities of body fluid and tissue compositions[45, 46]. In order to obtain more detail on the evaluations of the tissue for diagnoses, bioimpedance measurements are applied to specific local tissues, such as tumours, mammary glands and subcutaneous tissues[47, 48]. By taking one or more 2D slices through a patient, an image can be obtained, thus combining traditional mechanical ventilation, lung recruitment, and EIT imaging provides a comprehensive physiological model[49]. Therefore, in the medical field, the chief interest lies in imaging body organs (e.g. the brain[50] and lungs[51]), bones or other tissues like breast tumours, that have different characteristic impedances[52].

1.4 Potential applications for wearable EIT

While 3D imaging is the more popular topic among researchers, this dissertation focuses on a 2D EIT monitoring system where fabric sensors are used. This particular technology enables touch sensitive applications on robotic skin since conventional point based sensor mapping is almost impossible to implement at complex geometries like hand and face. In order to highlight the direction this dissertation takes with regard to pressure sensing and monitoring in EIT application, it is worth noting other conventional pressure sensing and monitoring techniques.

1.4.1 Pressure mapping imaging methods

Apart from the applications introduced above, the EIT as a pressure mapping imaging method is relatively new in the research field. Traditional sensing techniques like capacitive sensing and piezoresistive sensing have been widely studied. In table 1, a comparison is made between the pros and cons of conventional sensing techniques and fabric based EIT pressure sensors.

Type	Data	Pros	Cons
Capacitive[53, 54]	Change in capacitance	Excellent sensitivity, Good spatial resolution, Large dynamic range	Stray capacitance, Noise susceptible, Complexity of measurement electronics
Piezoresistive[55, 56]	Change in resistance	High spatial resolution, High scanning rate in mesh, Structured sensors	Lower repeatability, Hysteresis, Higher power consumption
Piezo-electric Strain (stress) polarization[57, 58]	Strain (stress) polarization	High frequency response, High sensitivity, High dynamic range	Poor spatial resolution, Dynamic sensing only
Inductive Linear variable differential transformer (LVDT)[59, 60]	Change in magnetic coupling	Linear output, Uni-directional measurement, High dynamic range	Moving parts, Low spatial resolution, Bulky
Optoelectric[61]	Light intensity/spectrum change	Good sensing range, Good reliability, High repeatability, High spatial resolution, Immunity from EMI	Bulky in size, Non-conformable
Strain gauges[62, 63]	Change in resistance	Sensing range, Sensitivity, Low cost, Established product Calibration, Susceptible to temperature changes	Susceptible to humidity, Design complexity, EMI induced errors, Non-linearity
Multi-component sensors[64-66]	Coupling of multiple intrinsic parameters	Ability to overcome certain limitations via combination of intrinsic parameters, Discrete assembly,	Higher assembly costs

Fabric based EIT pressure sensor[67]	Change in electrical impedance	Scalable, versatile, low cost, low power consumption, no mechanical parts, no wiring in sensing pad, conformable, design simplicity, low assembly costs, good sensing range, good reliability, high repeatability, immunity from EMI, sensing range, sensitivity	Spatial resolution

Table 1: Pros and cons of conventional sensors vs Fabric based EIT pressure sensor

As shown in the table, fabric based EIT pressure sensors overcome the disadvantages of most conventional sensing methods apart from its low spatial resolution.

1.4.2 Pressure monitoring application

The original idea of applying EIT based pressure sensing for pressure ulcers[68] was initially introduced by Fulton and Lipczynski back in 1993[69]. However, the experimental trials failed to identify a suitable conductive material for the EIT pressure sensor. Additionally, the idea of taking advantage of the enhanced flexibility and stretch potential of the fabric based EIT sensor was not considered at the time and so the work was eventually dropped. Recent developments from [70] have shown promising results with regard to the flexibility and stretch potential of these sensors and their integration in robotics as an artificial skin interface. Together with various new conductive materials, like pressure sensitive and conductive rubber CS57-7RSC (PCR technical, japan) [71] as well as many other fabric based materials developed over the years, it is certainly a good time to restart the programme.

1.4.3 Robotic Skin application

As human beings, we have been trying to replicate ourselves for almost a century. Despite the success around the world among developers, people still struggle to find a good solution for human interaction with robots. Traditional matrix based point sensors solve the problem for most even surfaces on the robot but locations with more complex geometry, like the face and hand, still seem far too challenging in terms of sensor implementation. By involving different conductive materials with deformation and a pressure sensing ability, it is much easier to implement on complex geometries since it does not require any wiring with the sensing area[72, 73]. It also enables robots to detect multi-touch stimuli in addition to detecting pressure with the sensor's deformation sensing ability. A comprehensive review of tactile sensors that are used for robotic interactions was made in [74].

1.5 Aim & Objectives

This project aims to develop a novel prototype imaging system that can measure various deformations and pressure over a 2D surface for both medical and robotic applications. As discussed in the medical application section, applications like pressure monitoring are one of our main interest areas. In order to achieve this goal, a system that has the following three parts is required:

- Measurement system
- Image reconstruction programme
- Fabric based sensor

Due to the ill-posed nature of the EIT technique, the system hardware design plays a crucial role, as all the proposed image reconstruction methods in this thesis needed

to be verified using experimental validation. In this thesis, several different EIT systems have been developed and modified for different proposed schemes.

In terms of the reconstruction programme, it is another important challenge in making a fully functional EIT system that fits our purpose. And to do this, an in-depth knowledge of Matlab and LabVIEW programming are essential.

For the fabric based sensor, several different designs have been carried out involving different numbers of electrodes, different materials and even different shapes. This thesis will show that by comparing the performance of all these different approaches a good solution will eventually converge.

As will be seen in this thesis, a thorough study of EIT has been carried out and it is believed the ideas and results presented in this thesis can certainly have a positive impact on the general EIT research community.

1.6 Organisation of thesis

The research presented in this thesis is organised into eight chapters. Chapter 1 discusses the history and various applications of EIT. Chapter 2 presents the main body of this thesis by starting with imaging reconstruction algorithms, followed by details about the mathematical model of the forward and inverse problems that are involved in the process of obtaining an image. The measurement system, which consists of a multiplexing circuit and a PC based control programme, is mostly hardware building and is explained in Chapter 3. In Chapter 4, a standard preliminary experiment for the EIT hardware is described, where the EIT Phantom Test is introduced, and the phantom test results are shown and analysed at the end of the chapter. Chapter 5 contains the deformation sensitive fabric sensor design

and test results with the previously built 16 electrode system. In chapter 6, the pressure sensitive fabric sensor is introduced and its test results are included at the end. Chapter 7, which is similar to the two sensor design chapters before, focuses on the square shaped fabric sensor, and, as part of the standard procedure, test results are included at the end of the chapter. Finally, the conclusion and discussion of future work will be presented in Chapter 8. Please note, each chapter, from chapter 2 onward, will have a self-conclusion at the end.

Various parts of this thesis have been published or are in the process of publication. The background information about EIT in Chapter 1, along with preliminary results from the EIT phantom test in Chapter 4 and the deformation sensitive fabric sensor in Chapter 5, have been published in one journal.

Chapter 2

2. EIT Image Reconstruction

The purpose of having an EIT system is to obtain the internal structural image of the measuring body. In this chapter, the image reconstruction software will be introduced and a brief overview of the Mathematical modelling of the EIT image reconstruction mechanism will be presented.

2.1 Reconstruction Algorithm

There are many different reconstruction algorithms and so far they can be categorised into four main classes, each with different aspects of impedance:

1. Time Difference Imaging systems are used to produce images of the change in impedance over a time interval. It is done by taking a set of measurement data V_1 at t_1 and another set of measurement data V_2 at a later time t_2 . The algorithm then calculates the conductivity change between t_1 and t_2 . The method is widely used for imaging temporal phenomena in medical applications, such as impedance changes during respiration [75, 76]. One of the main advantages of Time Difference Imaging is its ability to improve reconstructed image stability in the presence of problems such as unknown contact impedance, inaccurate electrode positions, poorly known boundary

shape, non-linearity, and the use of 2D approximations for 3D electrical fields[75, 76]. To calculate the change of conductivity, a series of iterative nonlinear reconstruction algorithms are used since it is a non-linear problem being dealt with.

2. Absolute or static systems are used to produce images of the absolute impedance distribution.
3. Multi-frequency imaging systems are used to produce an image for frequency-dependent impedance changes. For example, measurements from two different frequencies can be compared on the impedance change and produce an image[75, 76]. Also, injecting currents at a range of frequencies (9.6kHz to 1.2 MHz) and using different deriving parameters (Cole-Cole parameters) can produce interesting results[77, 78].
4. Dynamic imaging systems are best used for cases where fast conductivity changes are involved. When the conductivity changes, the acquisition interval can seem slow compared to the conductivity changing rate but the acquisition period of a frame of data is much faster[79].

2.2 Forward Problem

In order to solve the EIT Inverse problem, the forward problem needs solving, which is the model of the measurement process[80]. As defined previously[81], under low frequency assumptions, the full Maxwell's equations can be simplified to the complex valued Laplace equation, which will be derived.

The forward problem of EIT calculates boundary potentials with the given electrical conductivity or permittivity distribution, the first step is to construct a physical model for observation. This means that equations have to be derived, which connects

measured voltages, injected currents and a conductivity distribution. Starting from basic Maxwell's equations of electromagnetism, the equations for this physical model can be derived.

Maxwell's equations in inhomogeneous medium can be written in the form:

$$\text{(Faraday's Law of induction) } \nabla \times E = -\frac{\partial B}{\partial t} \tag{1}$$

$$\text{(Ampere's Law) } \nabla \times H = J + \frac{\partial D}{\partial t} \tag{2}$$

Where E is electric field, H is magnetic field, B is magnetic induction, D is electric displacement and J is electric current density.

If the injected currents are time-harmonic with frequency ω the electric and magnetic fields are of the form:

$$E = Ee^{j\omega t} \tag{3}$$

$$B = Be^{j\omega t} \tag{4}$$

Moreover, in linear isotropic medium the following relations are valid:

$$D = \varepsilon E \tag{5}$$

$$B = \mu H \tag{6}$$

$$J = \sigma E \tag{7}$$

Where ε is the permittivity, μ is the permeability, and σ is the conductivity of the medium. In EIT, the bodies are usually approximated as isotropic.

Using the relations (5-7) and assuming that the injected currents are time harmonic, the equations (1,2) can be written in the form:

$$\nabla \times E = -j\omega\mu H \tag{8}$$

$$\nabla \times H = J + j\omega\varepsilon E \tag{9}$$

In EIT, there are current sources that are denoted here with J_s. Therefore the current density is divided into two components$J = J_c + J_s$, where $J_c = \sigma E$ is the so-called conduction current. Now the equations (8,9) can be written in the form:

$$\nabla \times E = -j\omega\mu H \tag{10}$$

$$\nabla \times H = J_s + (\sigma + j\omega\varepsilon)E \tag{11}$$

These are the full Maxwell equations. In EIT, some simplifications for these full equations are made. The first one is the assumption of static conditions. This means that from the exact derivation of E,

$$E = -\nabla\varphi - \frac{\partial A}{\partial t} \tag{12}$$

Where φ is the electric potential and A is the magnetic vector potential, the latter is neglected. This means that the effect of magnetic induction that causes the induced electric field is neglected. This approximation is justified[82, 83] if:

$$\omega\varphi\sigma L_c \left(1 + \frac{\omega\varepsilon}{\sigma}\right) \ll 1 \tag{13}$$

Where L_c is a characteristic distance over which E varies significantly, therefore the effect of magnetic induction can be neglected.

Another approximation that is quite often made in EIT is that the capacitive effects ($j\omega\varepsilon E$ in 9) are neglected. This approximation is valid[84] if:

$$\frac{\omega\varepsilon}{\sigma} \ll 1 \tag{14}$$

With the above approximations, the modified Maxwell's equations in linear, isotropic medium under quasi-static conditions are:

$$E = -\nabla\varphi \tag{15}$$

$$\nabla \times H = J_s + \sigma E \tag{16}$$

Taking the divergence on both sides of equation (16) and substituting (15) into (16) the equation becomes:

$$\nabla \cdot (\sigma\nabla\varphi) = 0 \tag{17}$$

This is true since there is no source inside the body $J_s = 0$.

Since the conductivity σ and potential vary φ over the object, we denote them as $\sigma(\mathrm{x})$ and $\varphi(\mathrm{x})$, where x represents any point within or on the surface of the object.

Then equation (17) can be written as:

$$\nabla \cdot \big(\sigma(\mathrm{x})\nabla\varphi(\mathrm{x})\big) = 0 \tag{18}$$

The complete electrode model takes into account both the shunting effect of the electrodes and the contact impedances between the electrodes and the body. The complete electrode model consists of the equation (17) and the boundary conditions, as shown below[4]:

$$\varphi(\mathrm{x}) + Z_l \frac{\partial \varphi(x)}{\partial v}\Big|_x = \Phi_l \quad x \in e_l\,, l = 1,2,3,\dots,L \tag{19}$$

$$\int_{e_l} \sigma \frac{\partial \varphi}{\partial v}\Big|_x ds = I_l \;\; x \in e_l, l = 1,2,3,\dots,L \tag{20}$$

$$\sigma(x) \frac{\partial \varphi}{\partial v}\Big|_x = 0 \;\; x \notin {}_{l=1}^{L} e_l \tag{21}$$

Where z_l is effective contact impedance between the l th electrode and the body. In addition, the following two conditions for the injected current and measured voltages are needed to ensure the existence and uniqueness of the result.

$$\sum_{l=1}^{L} I_l = 0 \tag{22}$$

$$\sum_{l=1}^{L} \Phi_l = 0 \tag{23}$$

The forward problem must be solved multiple times. The potential $\varphi(x)^k$ and ${\Phi_l}^k$ can be set up by the given conductivity distribution $\sigma(x)$ and boundary condition I_l.

2.3 Finite Element Method

The Finite Element Method (FEM) is a numerical analysis technique for obtaining approximate solutions to a wide variety of engineering problems. It was originally developed as a tool for aircraft design but has since been extended to many other fields including the modelling of electromagnetic and electrostatic fields[4]. Due to its ability to model arbitrary geometries and various boundary conditions, the Finite Element Method is the most common method currently used for the numerical solution of EIT problems[5]. The following paragraphs are heavily based on [85].

In a continuum problem of any dimension, the field variable, such as the electric potential in EIT, is defined over an infinite number of values because it is a function of the infinite number of points in the body. The finite element method first discretises the medium under analysis into a finite number of elements collectively called a finite element mesh. Within each element, the field variable is approximated by simple functions that are defined only within the individual element. The approximating functions (sometimes called interpolation or shape functions) are defined in terms of the values of the field variables at specified points on the element called nodes. Most EIT work uses linear shape functions in which all nodes lie on the element boundaries where adjacent elements are connected. Higher order shape functions will have interior nodes. In summary, the finite element method reduces a continuum problem of infinite dimension to a discrete problem of finite dimension in which the nodal values of the field variable and the interpolation functions for the elements completely define the behaviour of the field variable within the elements and the individual elements collectively define the behaviour of the field over the entire medium.

There are three different methods typically used to formulate Finite Element problems:

1. Direct approach. The Direct approach is so called because of its origins in the direct stiffness method of structural analysis. Although the method is limited, it is the most intuitive way to understand the finite element method.

2. Variational approach. Element properties obtained by the direct approach can also be determined by the Variational approach which relies on the calculus of variations and involves extremising a functional such as the potential energy. The

variational approach is necessary to extend the finite element method to a class of problems that cannot be handled by direct methods. For example, problems involving elements with non-constant conductivity, problems using higher order interpolation functions, and for element shapes other than triangles and tetrahedrons.

3. Method of Weighted Residuals (MWR). The most versatile approach to deriving element properties is the Method of Weighted Residuals. The weighted residuals approach begins with the governing equations of the problem and proceeds without relying on a variational statement. This approach can be used to extend the finite element method to problems where no functional is available. The method of weighted residuals is widely used to derive element properties for non-structural applications such as heat transfer and fluid mechanics.

Regardless of the particular finite element method selected, the solution of a continuum problem by the finite element method proceeds with the following general sequence of operations:

1. Discretise the continuum. The FE method consists of discretising the spatial domain, denoted, into a number of non-uniform, non-overlapping, elements connected via nodes. Triangles and rectangles are used in 2D problems while tetrahedral and hexahedral elements are used for 3D. Additionally meshes using a mixture of different types of elements are possible. In this thesis, only simplices (triangles for 2D) are used. Figure 2.1 shows a 2D mesh constructed of triangles.

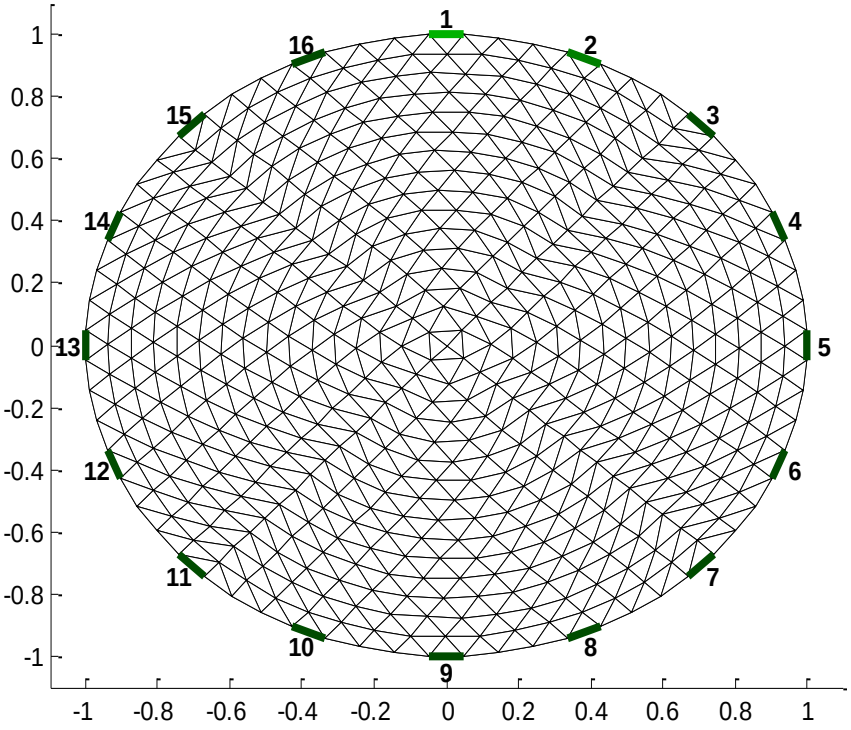

Figure 2.1: 2D mesh with 16 electrodes

2. Select interpolation functions. The field variable is approximated within each element by an interpolating function that is defined by the values of the field variable at the nodes of the element. Interpolation functions can be any piecewise polynomial function defined at a number of nodes. Linear interpolation functions are used for most of the work in this thesis. Other interpolation functions have been used with EIT, for example Marko et al use quadratic interpolation functions in [86, 87].

3. Find the element properties. This means calculating the local matrix for each element.

The symbol Y, with appropriate subscripts, is used to denote the components of local matrices throughout this thesis.

4. Assemble the element properties to obtain a system equation. This means combining the local matrices into a single master or global matrix. The symbol Y or A, without subscripts, are used throughout to denote the global matrix.

5. Impose the Boundary Conditions (BC). Boundary conditions can be fixed (also known as Type I, Dirichlet, or essential boundary conditions), derivative (also known as Type II, Neumann, or natural boundary conditions), or a combination of both (mixed, also known as Type III boundary conditions). With Dirichlet boundary conditions, the value of the field variable is prescribed for selected boundary nodes. For Neumann conditions, the derivative of the field variable is prescribed at selected boundary nodes.

6. Solve the system of equations. The algebraic system is of the form YV = I. The system is solved by Linear Algebra software such as Matlab.

7. Make additional computations, if desired. This would be required for iterative algorithms, algorithms that use adaptive currents and adaptive mesh refinement.

The finite element method converts the measured subject into a number of triangular elements and creates a finite element mesh [fig1]. Inside the mesh, the conductivity is assumed to be constant and the voltage distribution is linear.

The figure below shows an individual element from the modelled mesh [fig2][88] and its vertices are denoted by $1(x_1, y_1)$, $2(x_2, y_2)$, $3(x_3, y_3)$with corresponding shape function N1, N2, N3 respectively and nodal potentials φ_1, φ_2, φ_3.

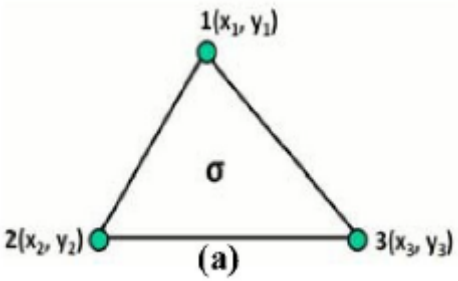

Figure 2.2 An individual element from the mesh[84]

2.3.1 Derivation of Linear Interpolation Functions

In order to fully understand the Method of Weighted Residuals we must derive the linear interpolation functions of the field variable. The following derivation is based on [89].

Since, in a 2-D domain, we consider the triangle potentials to vary linearly within all the elements therefore nodal potential can be written as:

$$\varphi(x,y) = p + qx + ry = [1 \quad x \quad y][p \quad q \quad r]^T \tag{24}$$

Hence,

$$\varphi_1(x_1,y_1) = \varphi_1 = p + qx_1 + ry_1 \tag{25}$$

$$\varphi_2(x_2,y_2) = \varphi_2 = p + qx_2 + ry_2 \tag{26}$$

$$\varphi_3(x_3,y_3) = \varphi_3 = p + qx_3 + ry_3 \tag{27}$$

Using (25, 26, 27), equation (24) yields,

$$\varphi(x,y) = \frac{1}{D}\left[\begin{vmatrix}\varphi_1 & x_1 & y_1\\ \varphi_2 & x_2 & y_2\\ \varphi_3 & x_3 & y_3\end{vmatrix} + \begin{vmatrix}1 & \varphi_1 & y_1\\ 1 & \varphi_2 & y_2\\ 1 & \varphi_3 & y_3\end{vmatrix}.x + \begin{vmatrix}1 & x_1 & \varphi_1\\ 1 & x_2 & \varphi_2\\ 1 & x_3 & \varphi_3\end{vmatrix}\cdot y\right]$$

Where, $D = 2 \times Area\ of\ the\ element(A) = 2\begin{vmatrix}1 & x_1 & y_1\\ 1 & x_2 & y_2\\ 1 & x_3 & y_3\end{vmatrix}$

$$\varphi(x,y) = \frac{1}{D}[\varphi_1\{(x_2y_2 - y_2x_3) + (y_2 - y_3)x + (x_3 - x_2)y\} + \varphi_2\{(x_3y_1 - x_1y_3) + (y_3 - y_1)x + (x_1 - x_3)y\} + \varphi_3\{(x_1y_2 - x_2y_1) + (y_1 - y_2)x + (x_2 - x_1)y\}] \tag{28}$$

Hence, $\varphi(x,y) = \sum_{i=1}^{3} \frac{1}{D}(a_i + b_i x + c_i y)\varphi_i$ (29)

Thus, the potential within a typical triangular element in a 2D mesh can be approximated by:

$$\varphi(x,y) = \sum_{i=1}^{3} N_i \varphi_i \quad (30)$$

N_i is called the shape function which can be defined as:

$$N_i = \frac{1}{D}(a_i + b_i x + c_i y) = \frac{1}{2A}(a_i + b_i x + c_i y) \quad (31)$$

Therefore, the shape functions at the three nodes of the element as expressed as:

$$N_1 = \frac{1}{2A}\{(x_2 y_2 - y_2 x_3) + (y_2 - y_3)x + (x_3 - x_2)y\} \quad (32)$$

$$N_2 = \frac{1}{2A}\{(x_3 y_1 - x_1 y_3) + (y_3 - y_1)x + (x_1 - x_3)y\} \quad (33)$$

$$N_3 = \frac{1}{2A}\{(x_1 y_2 - x_2 y_1) + (y_1 - y_2)x + (x_2 - x_1)y\} \quad (34)$$

Shape functions are interpolatory on the three vertices of the triangle. Each function, N_i is zero at all vertices except one where its value is one:

$$N_i(x_j, y_j) = \begin{cases} 1 & i = j \\ 0 & i \neq j \end{cases} \quad (35)$$

i = 1,2,3 and j = 1,2,3

Equation (30) completely defines the potential within the triangular element as a function of the values of the potential at the element's three nodes.

2.3.2 Method of Weighted Residuals (MWR)

There are several different methods used in weighted residuals including Collocation, Least Squares, and Galerkin with the latter method being the most common.

In order to solve equation (25), we can use $\nabla \cdot \sigma \nabla \varphi_{fem} = R$ (36)

Where R is called the "Residual"

To solve the equation, R has to be zero, hence,

$$\int_{\Omega} WRd\Omega = 0 \quad (37)$$

Where, W = Weighting function which is defined as:

$$W(\vec{x}) = \sum_{i=1}^{n} \omega_i N_i(\vec{x}) \quad (38)$$

ω_i are the coefficients that weigh the interpolation functions N_i. By applying equation (36) and (37) :

$$\int_{\Omega} W(\nabla \cdot \sigma \nabla \varphi_{fem}) d\Omega = 0 \quad (39)$$

For a scalar function α, and a vector function B, the "vector derivative identity"[89] equation (39) yields,

$$\int_{\Omega} [\nabla \cdot (W\sigma \nabla \varphi_{FEM})] d\Omega = \int_{\Omega} [\sigma \nabla \varphi_{FEM} \cdot \nabla W] d\Omega \quad (40)$$

To introduce the boundary condition we need to involve Gauss' Theorem on equation (40)

$$\int_{\Omega} W\sigma \nabla \varphi_{FEM} \cdot \hat{n} d\Gamma = \int_{\Omega} [\sigma \nabla \varphi_{FEM} \cdot \nabla W] d\Omega \quad (41)$$

Where, $\nabla\varphi \cdot \hat{n} = \frac{\partial\varphi}{\partial n}$ and $\Gamma = \ d\Omega$ represents the boundary. Therefore to rewrite equation (40)

$$\int_{\Omega} \sigma\nabla\varphi_{FEM} \cdot \nabla W d\Omega = \int_{\Omega} W\sigma \frac{\partial\varphi}{\partial\hat{n}} d\Gamma \tag{42}$$

Since the boundary integral only needs to be carried out for elements underneath electrodes. The left side of equation (42) is for the entire mesh. When examined for a single triangular 2D element, k, the left hand side of the equation (42) is given by:

$$\int_{E_k} \sigma_k \nabla\varphi \cdot \nabla W \, d\Omega \tag{43}$$

Substituting the definitions of the interpolating versions of φ and W yields,

$$\int_{E_k} \sigma_k \nabla\varphi \cdot \nabla W \, d\Omega = \sigma_k \sum_{\mathrm{i}=1}^{3} \varphi_i \sum_{\mathrm{j}=1}^{3} \omega_j \int_{E_k} \nabla N_i \cdot \nabla N_j d\Omega \tag{44}$$

$$\int_{E_k} \sigma_k \nabla\varphi \cdot \nabla W \, d\Omega = \sigma_k \sum_{\mathrm{i}=1}^{3} \varphi_i \sum_{\mathrm{j}=1}^{3} \omega_j \, S_{ij}^{k} \tag{45}$$

Where, S_{ij} is called the local stiffness matrix and can be defined as:

$$S_{ij}^{k} = \int_{E_k} \nabla N_i \cdot \nabla N_j d\Omega \tag{46}$$

Thus, by applying Finite Element Method (FEM), we get a 3 x 3 matrix for each element of the mesh. This 3 x 3 matrix is known as the local stiffness matrix.

2.3.3 Jacobian Matrix

In the optimisation based methods it is often necessary to calculate the derivative of the voltage measurements with respect to a conductivity parameter. The complete matrix of partial derivatives of voltages with respect to conductivity parameters is the

Jacobian Matrix[85] and we call it J. It is also known as the sensitivity matrix or sensitivity maps in some medical and industrial EIT literature.

Since we adapted the Time Difference imaging algorithm to our system, to do the reconstruction two sets of measurements are required. The elements that formed the measurement set are voltage readings between electrodes and since there are 16 electrodes, there are 208 voltage readings in each set. The first set of measurement that does not have any inclusion or deformation is called the background measurement or reference frame and is taken at time t_1. The other sets of measurements that contains inclusion or deformation are called data frames and are taken at time t_2.

The difference between the measured voltage (with deformation or inclusion) and the background voltage is ΔV. J is the Jacobian Matrix with a size of 208×422 for example: 422 is the number of imaging pixels and 208 is the number of measurements. $\Delta\sigma = \sigma_2 - \sigma_1$ is the change of finite element conductivity distribution due to a change in difference signal, $\Delta V = V_2 - V_1$, over a time interval (t_1, t_2). Therefore, we obtain the following equation:

$$\Delta V = J\Delta\sigma + Noise \tag{47}$$

2.4 Inverse Problem

2.4.1 Singular Value Decomposition – SVD

The Singular Value Decomposition (SVD) is a factorisation of a real or complex matrix, it is also recognised as the generalisation to non-square matrix of orthogonal diagonalisation of the Hermittian matrix[85]. Since SVD does not require the matrix

to be either symmetric or have full rank, it is very useful in solving the inverse problems in EIT.

Let $A \in \mathcal{R}^{m\times n}$ be a rectangular matrix where $m \geq n$, then the SVD of A is in the form:

$$A = USV^T = \sum_{i=1}^{n} u_i \sigma_i {v_i}^T \tag{48}$$

Where $U = (u_1, \dots, u_n)$ and $V = (v_1, \dots, v_n)$ are matrices with orthonormal columns, $U^T U = V^T V = I_n$, and since $S = diag(\sigma_1, \dots, \sigma_n)$ has non-negative diagonal elements, which by convention, are arranged in non-increasing order such that

$$\sigma_1 \geq \cdots \geq \sigma_n \geq 0$$

σ_i are the singular values of A while u_i and v_i are the right and left singular vectors of A respectively.

If $rank(A) = k < n$ then the singular vectors $v_{k+1}, \dots, v_n$ form an orthonormal basis for null(A), whereas $u_1, \dots, u_k$ form a basis for range(A). On the other hand, if $k = rank(A) < m$, then $v_1, \dots, v_k$ form a basis for range(A^*), and $u_{k+1}, \dots, u_m$ form an orthonormal basis for null(A^*)

In summary:

$$Av_i = \sigma_i u_i \quad i \leq \min(m, n)$$

$$A^* u_i = \sigma_i v_i \quad i \leq \min(m, n)$$

$$Av_i = 0 \quad rank(A) < i \leq n$$

$$A^* u_i = 0 \quad rank(A) < i \leq m$$

$$u_i{}^* u_j = \delta_{ij}, v_i{}^* v_j = \delta_{ij}$$

$$\sigma_1 \geq \sigma_2 \geq \cdots \geq \sigma_n \geq 0$$

Since the condition number of a matrix is relative as it is related to the precision level of the computations and is a function of the size of the problem[1]. The condition number of A is equal to the ratio σ_1/σ_n. Generally, a problem with a low condition number is said to be well-conditioned, while a problem with a high condition number is said to be ill-conditioned.

2.4.2 Tikhonov Regularisation

When solving the inverse problem are usually ill-conditioned systems, we introduce regularisation methods to reduce the error effects by restoring continuity of the solution on the data[90].

Tikhonov Regularisation is one of the most widely used methods. The standard form of Tikhonov Regularisation, is rather than minimising $\|Ax - b\|$, minimises an expression of the form:

$$\hat{x} = \arg\min_x \{\|Ax - b\|^2 + \lambda^2 \|Rx\|^2\} \quad (49)$$

Where R is a regularisation matrix in many cases it is either an identity matrix or diagonal matrix. The expression $\lambda^2\|Rx\|^2$ represents prior information added for the conductivity. When > 0, since the expression is quadratic it is a guarantee for a unique solution.

In most cases of Tikhonov regularisation, the regularisation matrix R is chosen as the identity matrix $R = I$, giving preference to solution x is small, slowly changing or smooth.

In our case because J is not a square matrix (208×422), the system is underdetermined.

Since the Jacobian Matrix J is not square, in order to invert J, it is necessary to involve J^T. By applying J^T to both sides, hence:

$$J^T \Delta V = J^T J \Delta \sigma \tag{50}$$

Therefore:

$$\Delta \sigma = (J^T J)^{-1} J^T \Delta V \tag{51}$$

Because $(J^T J)^{-1}$ is ill-posed, we add λR which is the regularisation factor, hence:

$$\Delta \sigma = (J^T J + \lambda R)^{-1} J^T \Delta V \tag{52}$$

Adding λR helps to stabilise the equation. Therefore, it is possible to obtain a more stable solution.

2.4.3 L-curve method

Generally speaking, regardless of the form regularisation method that is used for an inverse problem they all face a trade-off between the "size" of the regularised solution and the quantity of the fit that it provides to the given data. Since each regularisation methods minimises this trade-off differently, it can be controlled by selecting a proper regularisation parameter. In this section, we will discuss the methods that have been developed to find the best value for the regularisation parameter.

There are three methods which have been developed for an optimal selection of the regularisation parameter:

- L-curve Method
- Discrepancy Principle
- Generalised cross validation method

Basically, the L-curve method is a log-log plot between the squared norm of the regularised solution and the squared norm of the regularised residual for a range of values of regularisation parameter. Below is the standard form of the L-curve:

$$L: = \{(\log\|Rx_\lambda\|\,, \log\|Ax_\lambda - b\|) : \lambda \geq 0\} \tag{53}$$

Where R is referred to as the regularisation matrix and $\lambda \geq 0$ as the regularisation parameter.

Since R is non-singular, the minimisation problem (49) has the unique solution:

$$x_\lambda = (A^T A + \lambda R^T R)^{-1} A^T b \tag{54}$$

Since we are dealing with λ^2 instead of λ, for any $\lambda > 0$ and λ is positive, we introduce:

$$\eta_\lambda \coloneqq \|Rx_\lambda\|^2, \;\; \rho_\lambda \coloneqq \|Ax_\lambda - b\|^2$$

And:

$$\bar{A} = AR^{-1}, \qquad \bar{x} = Rx$$

Hence:

$$\eta_\lambda \coloneqq \|\bar{x}_\lambda\|^2 = b^T \bar{A}(\bar{A}^T \bar{A} + \lambda I)^{-2} \bar{A}^T b \tag{55}$$

$$\rho_\lambda : = \|\bar{A}\bar{x}_\lambda - b\|^2 = \lambda^2 b^T (\bar{A}\bar{A}^T + \lambda I)^{-2} b \tag{56}$$

Let:

$$\hat{\eta}_\lambda := \log \eta_\lambda \,,\ \hat{\rho}_\lambda := \log \rho_\lambda \tag{57}$$

Then the point on the L-curve associated with the value λ of the regularisation parameter is given by $P_\lambda = \frac{1}{2}(\hat{\eta}_\lambda, \hat{\rho}_\lambda)$. The curvature of the L-curve at P_λ is:

$$\kappa_\lambda = 2\frac{\hat{\rho}_\lambda{}''\hat{\eta}_\lambda{}' - \hat{\rho}_\lambda{}'\hat{\eta}_\lambda{}''}{\left((\hat{\rho}_\lambda{}')^2 + (\hat{\eta}_\lambda{}')^2\right)^{3/2}} \tag{58}$$

Where $'$ denotes differentiation with respect to λ. Simply follow from (57) and $\rho_\lambda{}' = -\lambda\eta_\lambda{}'$ so that:

$$\kappa_\lambda = 2\frac{\eta_\lambda\rho_\lambda}{\eta_\lambda{}'}\frac{\lambda\eta_\lambda{}'\rho_\lambda + \eta_\lambda\rho_\lambda + \lambda^2\eta_\lambda\rho_\lambda{}'}{(\lambda^2\eta_\lambda{}^2 + \rho_\lambda{}^2)^{3/2}} \tag{59}$$

2.5 Conclusion

This chapter gives a basic introduction to EIT image reconstruction algorithm used in our EIT system, then followed by basic forward and inverse problem theory, including the finite element method which is a common method for modelling in EIT field, and also the Jacobian matrix which is a key factor in solving the inverse problem. The next chapter will introduce the hardware part of our EIT system.

Chapter 3

3. Hardware System

The hardware section of our EIT system consists of three parts:

- Data Acquisition Card
- Multiplexing Circuit
- Current Source

In order to aid the understanding of the general flow of our system, the figure below was produced:

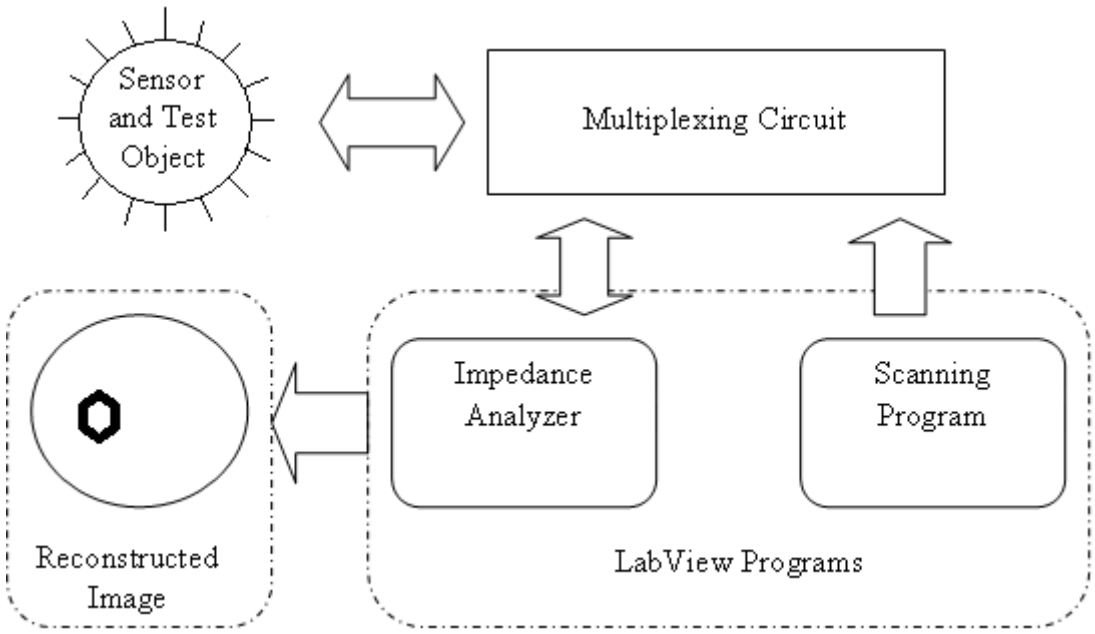

Figure 3.1: System Flow Chart

From fig 3.1 we can see, all switching actions of the Multiplexing Circuit are controlled by the LabVIEW programme, which is a PC based software through the Data Acquisition Card that acts as an Input / Output channel. Once the measurements are taken, they can then be saved and passed onto the reconstruction software for image reconstruction.

3.1 Data Acquisition

For data acquisition, we use the NI USB-6259 DAQ card (Fig 3.2) from National Instrument. This is a High-speed USB multifunction data acquisition module, optimised for high accuracy at a fast sampling rate. It is ideal for applications such as dynamic signal acquisition and sensor measurement. One of the reasons this module was chosen is because it has the data processing unit built in, hence it receives data, converts it to a digital signal, and transfers it to a PC without having to use additional hardware. Also, it is compatible with the Labview Software, which provides all the virtual instrument setups as well as taking control of the multiplexer switching pattern for the excitation and measurement system right from the PC.

Below is the detailed specification for NI-USB 6259:

Analogue Inputs: 32 (16-bit)
Analogue Outputs: 4 (16-bit)
Sampling rate: 1.25MS/s
Digital I/O ports: 48 (32 clocked and 2 32-bit counters)
Max voltage: -10V to 10V
Maximum I/O voltage: 5V
Maximum Current Supply: 5mA

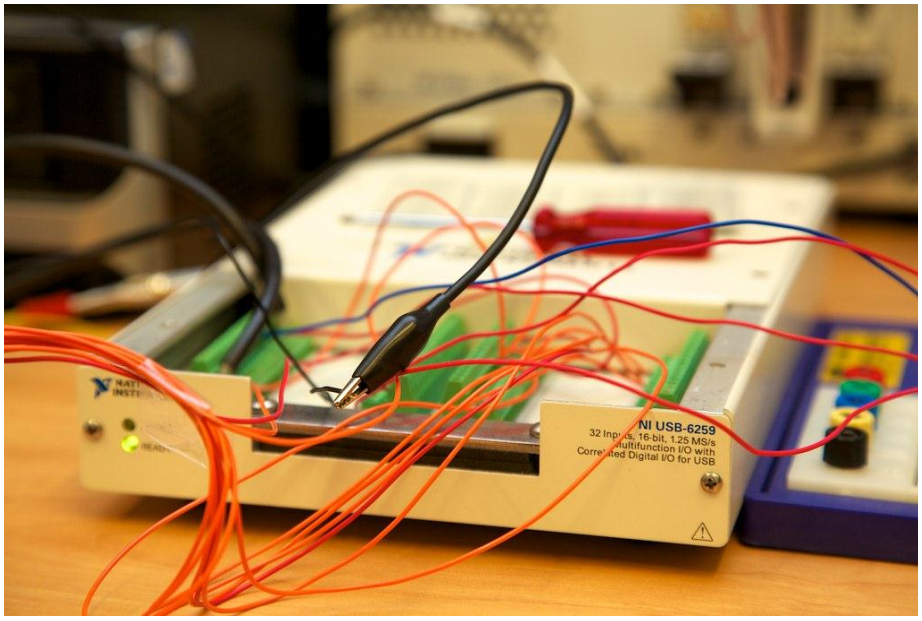

Figure 3.2: NI USB-6259 Data Acquisition Card

Figure 3.3 below is the pin out connectors for the data acquisition card.

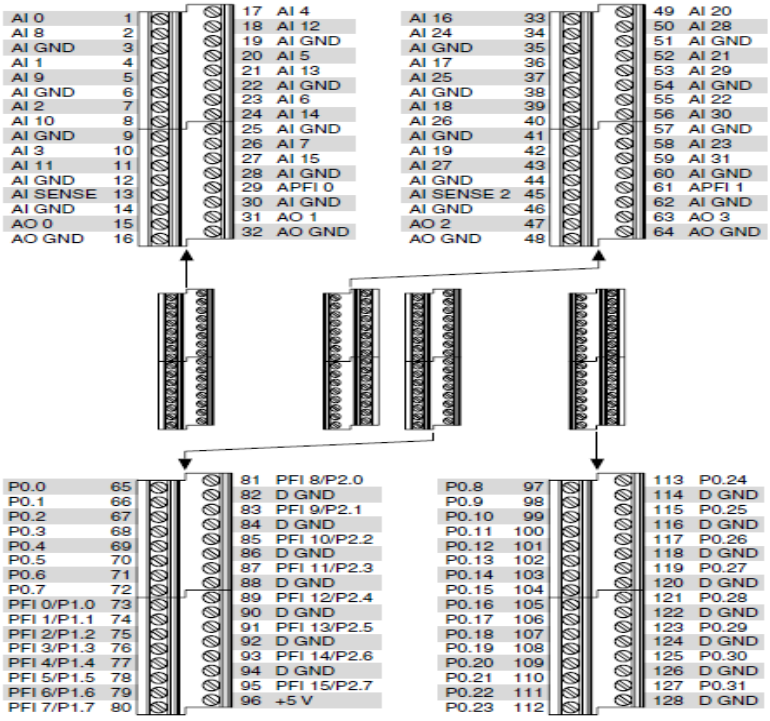

Figure 3.3: NI USB 6259 pin out connections

AI = Analog input
AIGND = Analog input ground
AO = Analog output
AO GND= Analog output ground
PO.X= digital output
D.GND= digital ground

3.2 EIT system 2D – 16 Electrodes

3.2.1 Adjacent Switching Pattern

The 16-Electrode 2D system uses the adjacent method for creating excitations and taking measurements. The adjacent pattern in our 16-electrode system works by injecting current through pairs of neighbouring electrodes, ie. (1-2), (2-3),…, (15-16),(16-1). For each of these current injection patterns, different potential distributions will occur, so that the voltage difference between the remaining pairs of neighbouring electrodes can be measured across the entire system. Figure 3.4 provides a more visualised explanation of the method.

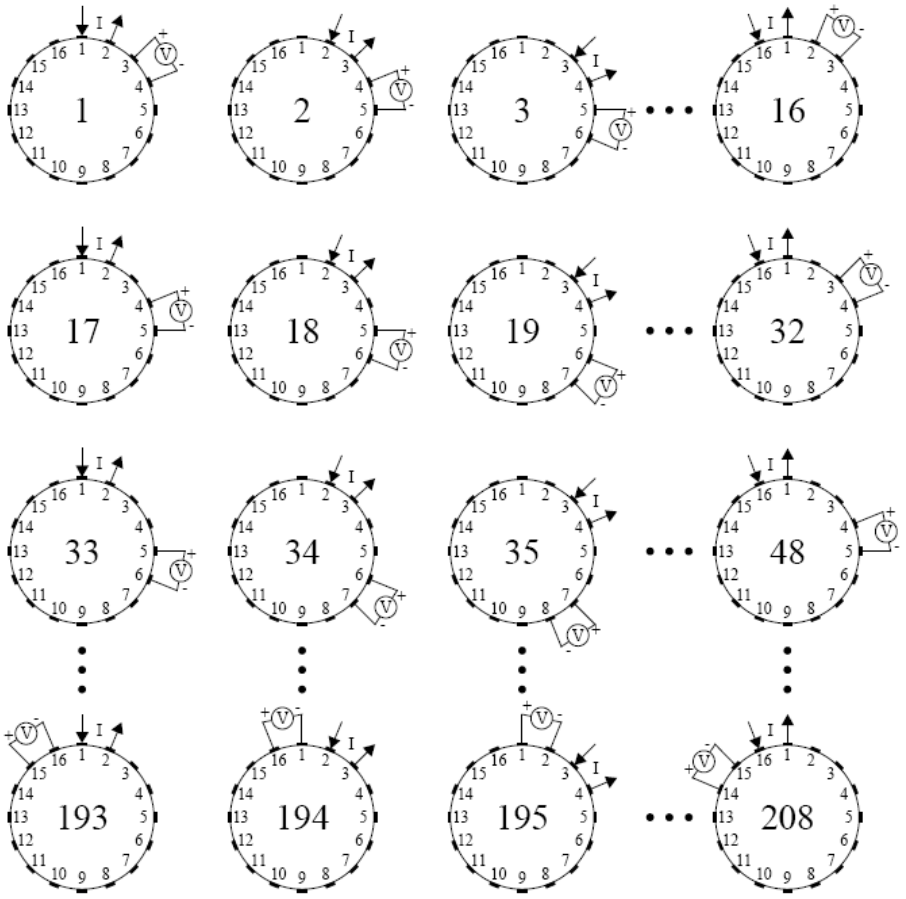

Figure 3.4: Adjacent Switching Pattern[91, 92]

Each injection pattern takes 13 voltage measurements. Since our system consists of 16 electrodes, there are 16 injection patterns; this result is 16x13 = 208 total measurements will be taken in a complete measurement cycle.

For the multiplexing system to understand those switching commands, we have to convert the number of electrodes into binary. For detailed conversion please refer to the table in Appendix A.

3.2.2 Multiplexing Chip

The multiplexing chip we use in our 16-electrode system is the ADG406BNZ from Analog Devices. This multiplexing chip is capable of transferring 20mA continuously and it has low input/output capacitance, which reduces the effect of stray capacitance. Figure 3.5 is the pin output for ADG406BNZ.

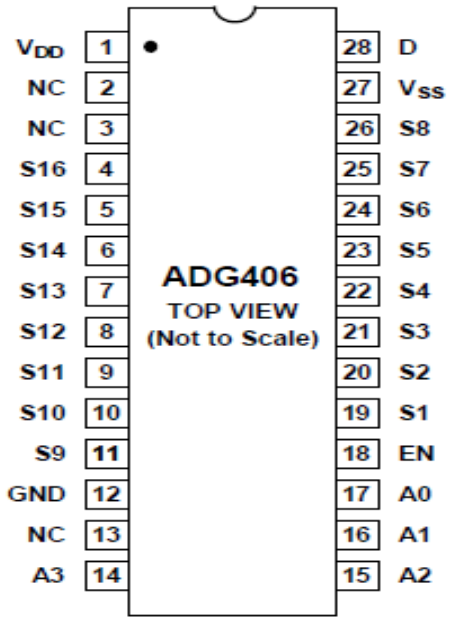

Figure 3.5: Pin configuration of ADG406BNZ

V_{DD}: Positive power supply rail

V_{SS}: Negative power supply rail

GND: Ground

D: Single input/output. When connected to DAQ it measures voltage, when connected to the excitation circuit it supplies current.

S1-S16: Multi-channel input output pins. For our 16-electrode system, these 16 pins are connected to phantom to measure the potential difference and transfer voltage to DAQ through D pin. They also supply current from D to Phantom electrode.

EN: Enable. The Multiplexer's ON/OFF pin.

A0-A3: Digital pin input from DAQ, binary codes are generated to enable the particular input/ output switching pattern.

Figure 3.6 is the circuit schematic diagram for our multiplexing circuit. Figure 3.7 is the PCB board diagram respectively. The pins are defined as follow:

Power Pin 1= +15V

Power Pin 2= Ground

Power Pin 3= -15V

C1-C4 = Decoupling Capacitors. These capacitors decouples the power supply from the multiplexer and reduces the noise produced. Each with a value of 100µf sets in parallel between power supply and multiplexer V_{DD}-GND

S1-S16= Connected to the 16 Electrodes.

EN= Connected to +15V supply which makes it always ON.

Digcon1 – Digicon4= Connected to A0-A3 which are the Digital pins of each Multiplexer chip.

Output 1: Connect to D pin of Multiplexer 1. It injects source current.
Output 2: Connect to D pin of Multiplexer 2. It sinks the current.
Output 3: Connect to D Pin of Multiplexer 3.
Output 4: Connect to D Pin of Multiplexer 4.
Output 3 and 4 takes the voltage measurement.

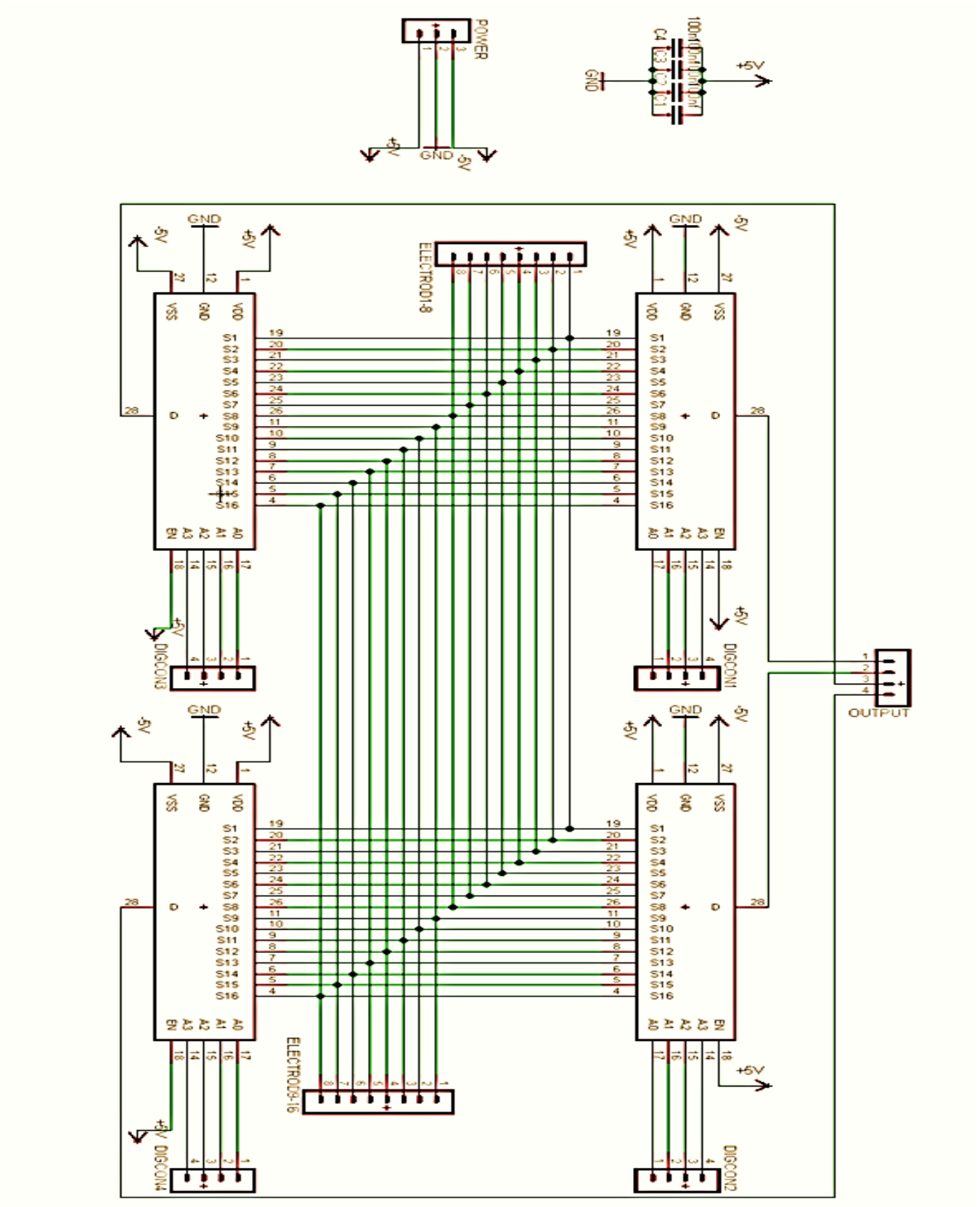

Figure 3.6: Schematic Diagram for the Multiplexing Circuit

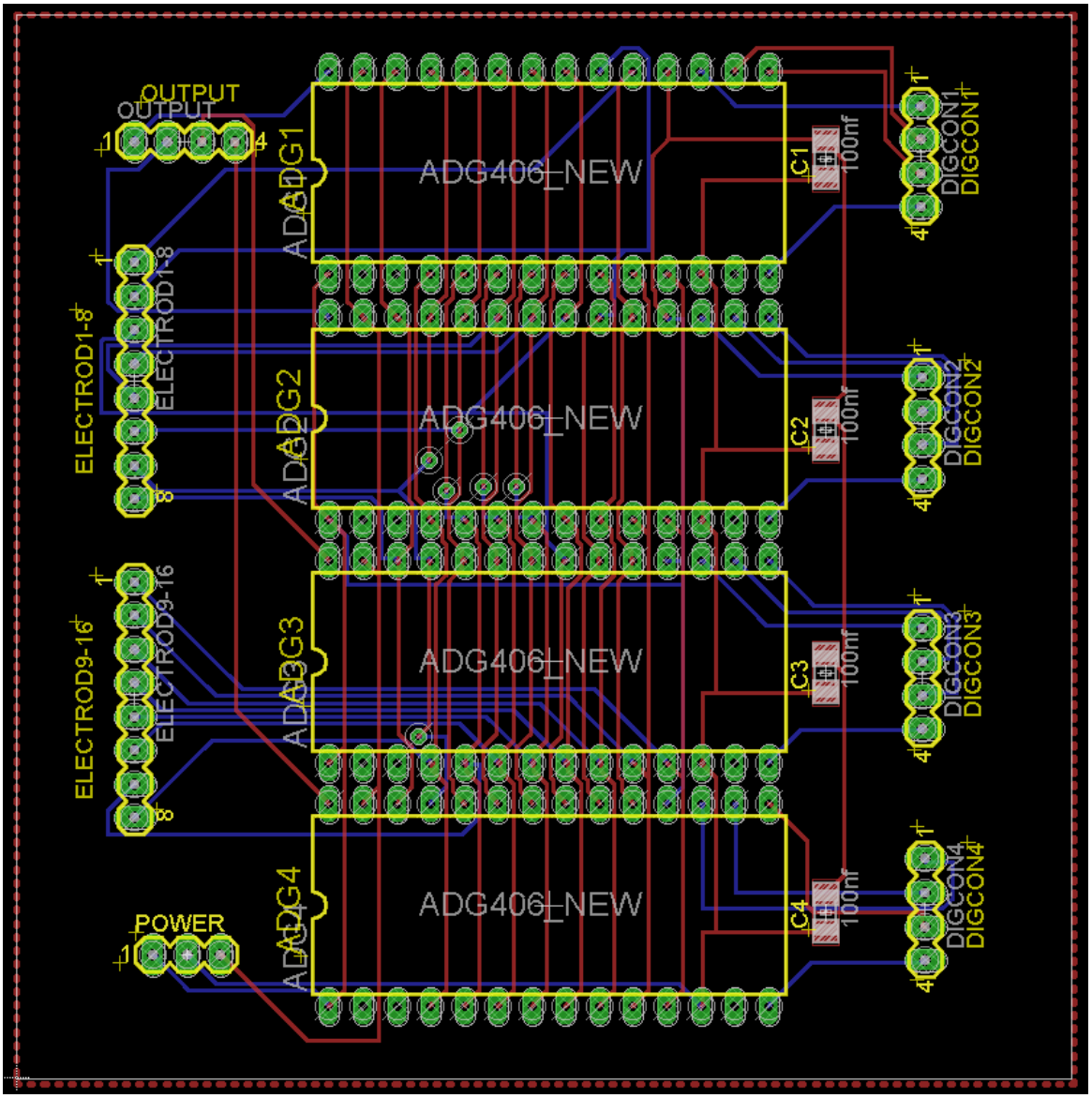

Figure 3.7: PCB Board diagram of the Multiplexing Circuit

3.2.2.1 LED Test for the LabVIEW switching code

To ensure a fully functional system, we test each part of the system by following the way the signal transmits. The multiplexer has four digital binary pins, these pins are used to switch between channels, the binary code generated by LabVIEW is sent to the digital output of the Data Acquisition card (NI USB-6259). In order to justify the correctness of these codes, we setup a 16 LED circuit, which simulates the 16 electrodes on an EIT system and provides visualised information. The LEDS are connected to the digital output pins of the Data Acquisition card.

Pins 1-4 are designed for current injection and pins 5-8 are designed for current sink. Pins 9-12 and pins 13-16 are designed for taking voltage measurement.

Figure 3.8 shows the LED test circuit.

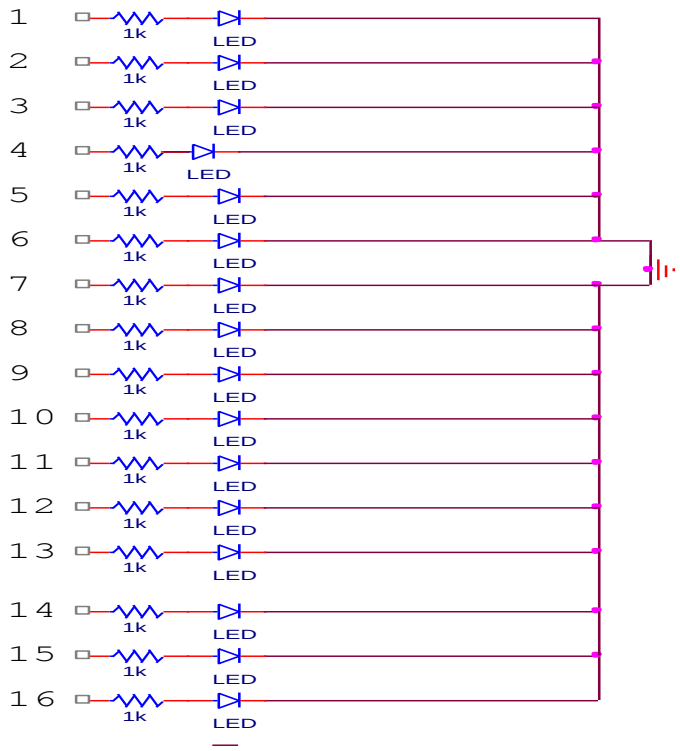

Figure 3.8: LED Test Circuit for Switching Code

To do the test, we first give the code: 0000 0000 0000 0000 to see if the LEDs are all OFF and then code: 1111 1111 1111 1111 to see if the LEDs are all ON. Once this test is passed, we simply run through the switching pattern which is generated with respect to the truth table of the multiplexing chip. For example, in the first excitation pattern, electrodes 1-2 are activated for current injection and sink, electrodes 3-4 are activated for voltage measurement. Hence we have 0000 = S1, 0001 = S2, 0010 = S3, 0011 = S4, then the code: 0000 0001 0010 0011 where LED 8, 11, 15, 16 will be ON.

3.2.3 Current Source

A current source is one of the most important circuits in Electrical Impedance Tomography (EIT) hardware systems. The existing LabVIEW based EIT system provides constant voltage as a form of excitation. The excitation creates an electromagnetic field within the test subject and the resulting voltage is measured by electrodes. The calculation of conductivity within the test subject is mathematically ill-posed and a large change in the conductivity distribution may result in a small change in the measured data. In order to minimise this error, the measurement and the excitation system must have maximum precision. Constant voltage based excitation may result in inaccurate data as supplied voltage can be varied by circuitry or resistive load. One example is shown in [90] where measured load current varies during the movement of the electrodes connected to the human body. The most common way to solve this problem is by designing a highly accurate current source which provides constant current up to the given load resistance:

- Contact resistance between electrode and skin can range between 100-2000Ω/m^2. For testing purposes, the phantom will be used as a test body. So the current source should be capable of providing precise current up to 10 kΩ load impedance.
- The current source must operate between 100Hz- 100 kHz.
- High output impedance so that all the currents are at the output.
- Capable of providing up to 5mA as it is the maximum allowable current for EIT application on the human body, but current source will be used by another imaging system within the research group so it must provide up to 20mA at low impedances.

Therefore, the most important and challenging feature of building an EIT system is to deliver a relatively large and constant current for a wide range of resistive loads while maintaining a high signal-to-noise ratio and a large bandwidth.

The current source is an electronic circuit that supplies constant current to each load regardless of its resistance. The supplied current is independent of voltage across the load[93]. Most EIT systems adopt Voltage Controlled Current Source (VCCS) where the circuit converts input voltage from the signal generator to the constant current. Figure 3.9 shows the circuit diagram of an ideal current source.

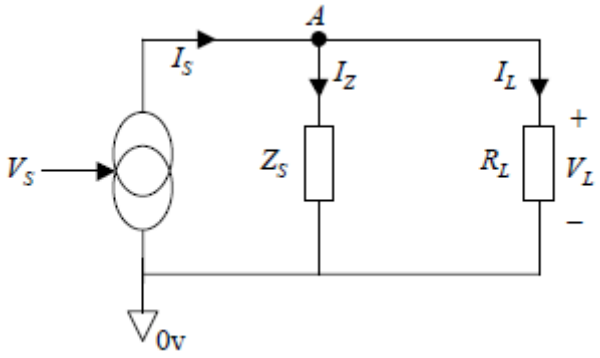

Figure 3.9: ideal current source model[94]

I_S= Output current

I_L= Load current

I_Z= Output Impedance current

Z_S= Output Impedance

R_L= Load Resistance

$$I_L = \frac{1}{1 + \frac{Z_L}{Z_s}} \times I_s \quad (60)$$

The equation proves that at infinite output impedance load current is equal to output current.

3.2.3.1 Howland Current Source

Conventional VCCSs that have been widely used in EIT are based on operational amplifiers with the most popular design being the Howland current source. The output current is determined by input voltage. Figure 3.10 shows the circuit diagram of a typical VCCS based on the Howland current source[95].

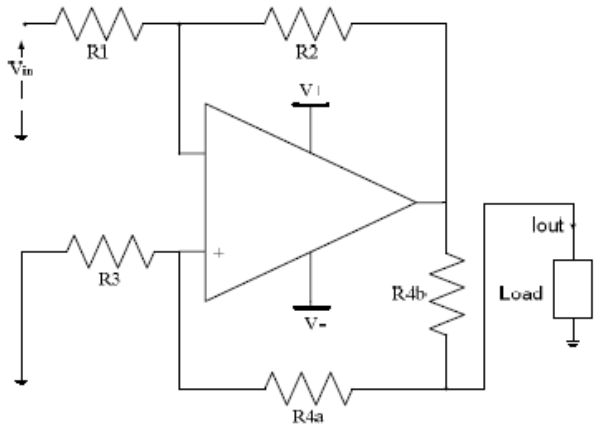

Figure 3.10: A VCCS based on the Howland current source[96]

Assuming the resistor R_{4b} is small and R_{4a} is large and the op-amp gain is very high, the output current I_o is thought to be injected to the load. Below is the relationship between the input voltage V_{in} and the output current I_o:

$$I_o = -\frac{R_2}{R_1 R_{4b}} V_{in} \tag{61}$$

The Output resistance of the circuit is given by:

$$R_o = \frac{R_1 R_{4b}(R_3 + R_{4a})}{R_2 R_3 - R_1(R_{4a} + R_{4b})} \tag{62}$$

Howland current source is capable of providing high output impedance. Its simple circuit design minimises noise and capacitance which usually is created by having larger circuits. Despite the advantages of simple design, an operational amplifier is

typically subject to non-linear limitations and the range of the power supply is limited. Another limitation is the slew rate which corresponds to the maximum rate of voltage change per time. When it reaches Maximum slew rate the output current tends to exhibit a triangular shape for a sinusoidal input voltage. After considering all these factors, the decision was made to adopt the improved version of Howland current source[96] and by adding two additional op-amp to give a much higher precision[95].

3.2.3.2 Triple op-amp current source circuit

The main objective of the current source is to maintain a stable potential across the sensing resistor R_5. Figure 3.11 shows the circuit diagram of the triple op-amped current source.

The circuit consists of three op-amps U1, U2 and U3 where U1 is the summing amplifier, U2 is the voltage follower and U3 is the inverter op-amp. The inverting input of U1 is connected to the input voltage V_{in} . The output of U1 is the sum of V_{in} and output of U3 inverted. The output of U3 is the inversion of the load voltage. Therefore the system sums the V_{in} with $-V_{load}$.

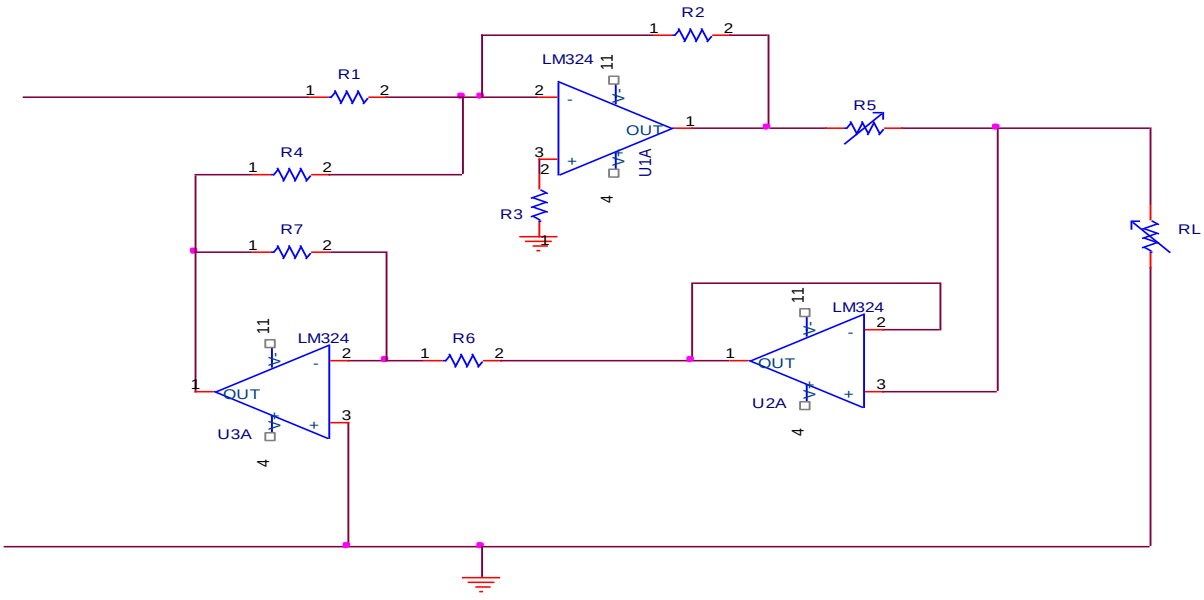

Figure 3.11: Circuit diagram of the Triple Op-Amped Current Source

Below is the derivation of the circuit operation[97]:

Since

$$V_6 = V_{load} \tag{63}$$

So

$$V_6 = \text{voltage at an output of U2}$$

Because U3 is the inverting amplifier, its output is the negative of its input.

$$V_4 = -V_6 = -V_{load} \tag{64}$$

So

$$V_4 = \text{voltage at U3 output}$$

Also because U1 is a summation amplifier, the voltage at output of U1 is

$$V_2 = -(V_{in} - V_{load}) = -V_{in} + V_{load} \tag{65}$$

So

$$V_2 = \text{voltage at U1 output}$$

Therefore the potential difference across R_5 will be:

$$V_{R5} = (-V_{in} + V_{load}) - V_{load} = -V_{in} \tag{66}$$

Hence the current supplied from output of U1 is

$$I_S = \frac{-V_{in}}{R_5} \tag{67}$$

I_S is the supplied current. From equation (32) and (33) we can assume I_S is equal to I_{load} when the input current to U2 is very small.

Finally the equation for I_{load} will yield as:

$$I_{load} = \frac{-V_{in}}{R_5} \quad (68)$$

The voltage at the left of R_5 is proportional to the load voltage. Maximum voltage drop across the load is limited by the input voltage V_{in} and the supply voltage of the amplifier. Other researchers suggest the current source is capable of maintaining constant current up to 10kΩ with output impedance of 0.7mΩ, the output impedance will be measured at testing stage[97].

3.2.3.3 Current Source Testing

In order to understand the performance level of the current source, a series of test have been put in place:

- Maximum Load
- Operational Frequency Range
- Output Impedance

In the initial design of the circuit, LM741 were used. But it soon became clear that it is not the most suitable component. Therefore, it was replaced with AD844AN, which is from Analog Devices. The reasons for this replacement were as follow[98]:

- Wider Bandwidth
- Larger Input impedance
- Greater Slew Rate

Fig 13 is the circuit diagram for the current source in Eagle CAD.

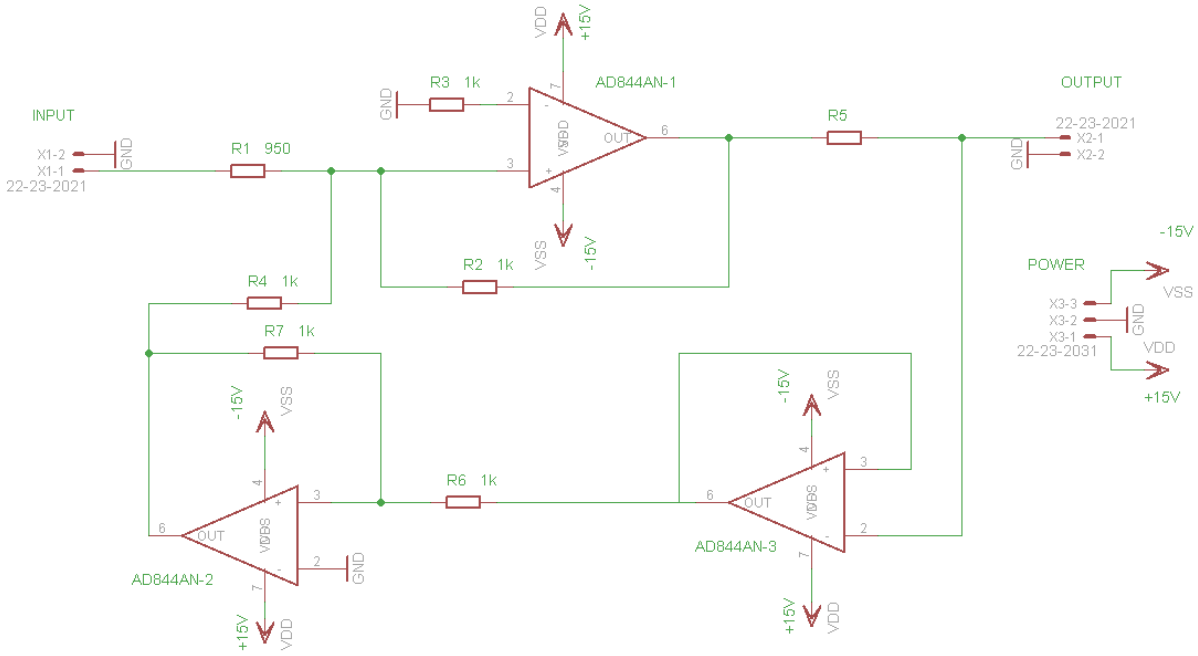

Figure 3.12: Circuit diagram for Current source

$R_1 = 950\Omega$ (Function Generator has output impedance of 50Ω

$R_2 = R_3 = R_4 = R_6 = R_7 = 1k\Omega$

R_5 = Variable dependent on the output current required

$V_{DD} = +15V$

$V_{SS} = -15V$

3.2.3.3.1 Maximum Load Test at 1mA, V_{IN}=1V, 1KHz

Since $I_{LOAD} = \frac{V_{IN}}{R_5}$, $I_{LOAD} = 1mA$, $V_{IN} = 1V$

Hence

$R_5 = 1K\Omega$ (Calculated value actual is approximately 950Ω

A 22KΩ variable resistor is used as a load resistor. The output current falls below 1mA after the load resistor was increased above 10.5KΩ. The output voltage enters saturation as it is set by the op-amp's supply voltage. Smaller input voltage was tested where it enables application for higher load resistance but the resulting signal was highly distorted.

3.2.3.3.2 Maximum Load Test at 5mA, V_{IN} =1V, 1KHz

Since $I_{LOAD} = \frac{V_{IN}}{R_5}$, $I_{LOAD} = 5mA$, $V_{IN} = 1V$

Hence,

$R_5 = 200\Omega$ (Calculated actual value is approximately 160Ω)

A 22KΩ variable resistor is used as load resistor. The output current falls below 5mA after the load resistor was increased above 2KΩ. The output voltage enters saturation due to the limitation of op-amp's supply voltage.

3.2.3.3.3 Maximum Operational Frequency Test

The aim of this test is to calculate the frequency range that the current source is capable of handling while maintaining a constant output current. The system was tested at 1mA output current with a 10KΩ load resistance and the output voltage indicated 10V.

Below is a table of multiple voltage measurements taken at various frequencies. Figure 3.13 shows the plot of the voltage measurements with respect to the frequency level.

frequency kHz	output voltage
0.1	9
1	9
5	9
10	9
15	9
20	9
25	9
35	9
50	8
85	7
100	6.8
160	5
500	2

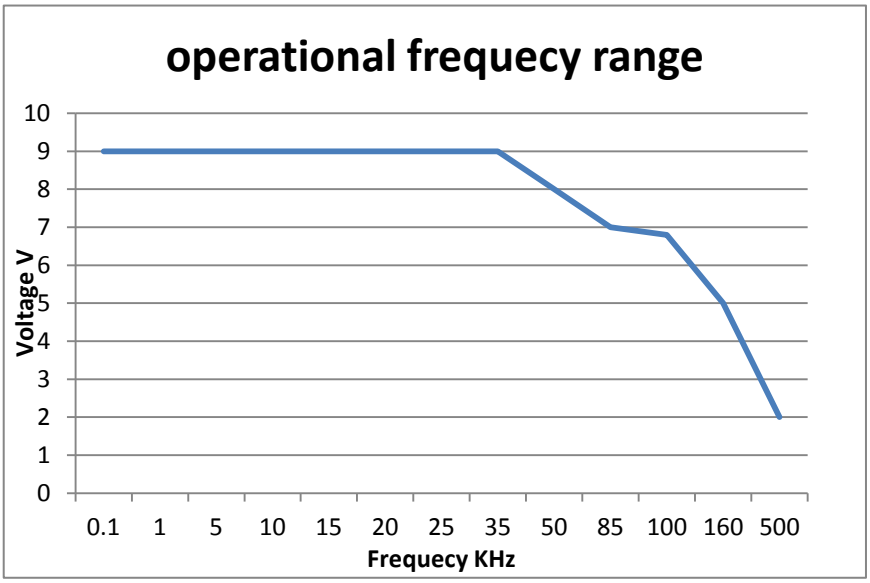

Figure 3.13: Load Voltage against Operational Frequency

From the results shown above, it is clear that our system fails to maintain a constant output after 35KHz. Therefore the operational frequency for this system is 0-35KHz.

3.2.3.3.4 Output Impedance Test

The output impedance provides an indication of the amount of generated voltage that is supplied as a load voltage. Figure 3.14 shows the circuit we used for calculating the Output Impedance. The circuit was tested at 1mA, V_{IN}=1V, 1KHz with 10KΩ Load.

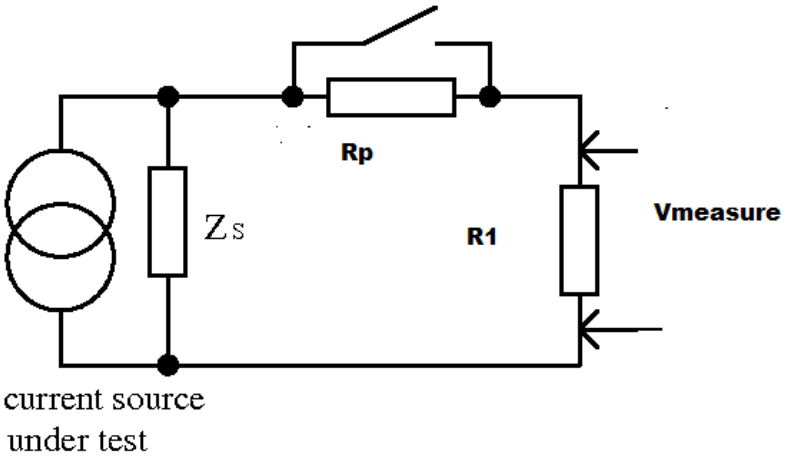

Figure 3.14: Output Impedance Calculation Circuit

From the data sheet of the oscilloscope it says the output impedance of the oscilloscope is 1MΩ. This means if we connect R_1 directly to the oscilloscope, this will result in large experimental errors. To minimise this error, $V_{MEASURE}$ which is the voltage measurement, was connected to a buffer amplifier with high input resistance and the output voltage was measured between the pin of op-amp and ground terminal. Below are the formulas used for output impedance calculation.

$$LOAD_{MAX} = R_p + R_1 \tag{69}$$

$$R_p > 100R_1 \tag{70}$$

From equation (69) and (70) we get:

$$R_p = 9910, R_1 = 90$$

Since

$$Z_s = \left(\frac{V_{open}}{V_{close} - V_{open}} \times R_p\right) - R_1 \tag{71}$$

The Output Impedance of our current source is 700KΩ.

3.3 Conclusion

In this chapter, we introduced the three major parts of our hardware system. The data acquisition card from National Instrument acts as an input/output device between the PC based controlling program, LabVIEW, and the multiplexing circuit which follows the adjacent switching pattern. The current source is another key element in our system hardware, since it provides a continuous constant driving signal to help us maintain a steady feedback from the sensor. The next chapter moves onto the most important experiment for the hardware system calibration - the phantom test.

Chapter 4

4. EIT Phantom Test

The EIT Phantom test is an effective way of determining the performance of a given EIT measurement system. It is also the first step in characterising an EIT system. In this chapter, the calibration and characterisation of the EIT system will be discussed using EIT Phantom.

4.1 Phantom Construction

To do the phantom test, we first need to build a phantom. The phantom that was built is an acrylic cylindrical pipe with 16 identical stainless steel stripes attached to its inner side. These stainless steel stripes act as electrodes so they are evenly spaced in between. The pipe sits on an acrylic board and is sealed at the bottom with silicon and hot glue to prevent leakage. Figure 4.1 is picture of the phantom.

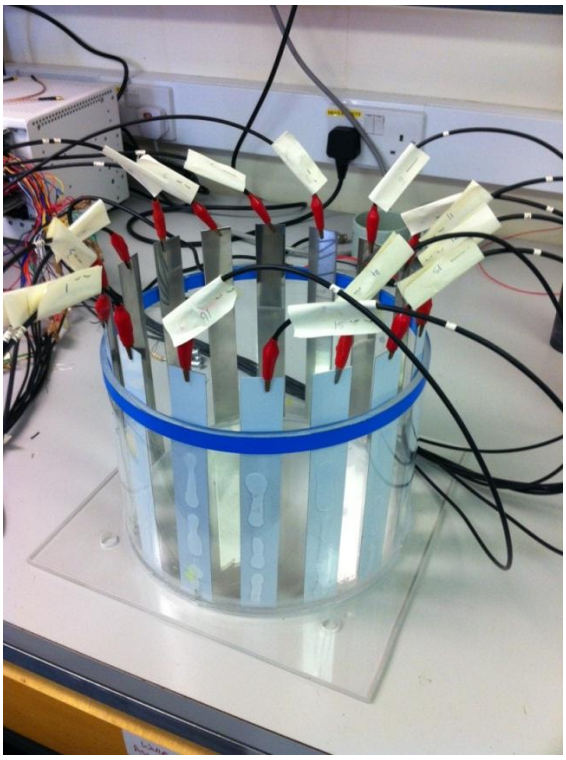

Figure 4.1: 16 Electrodes EIT Phantom

4.2 System Calibration Procedure

In order to eliminate any experimental errors due to mistakes in setup, a series of test procedures were developed.

- Same saline solution for all experiments.
- Identical data acquisition parameters, such as sampling rate and number of samples are maintained throughout all systems.
- Test subjects are placed in the same locations in the phantom for image reconstruction.
- Several iterations for each test cycle for experimental error elimination.

4.3 Signal to Noise Ratio Test

Signal-to-noise ratio (SNR) has been widely used for system performance categorisation. It compares the level of signal to the level of background. By putting this into formula we have:

$$SNR = \frac{Signal\ Power}{Noise\ Power} \tag{61}$$

To calculate the SNR of our system, we first need to measure the background for 40 frames of 208 channels. Here's the formula been used[99]:

$$SNR = 20 \log 10 \frac{|E[mi]|}{\sqrt{VAR[mi]}} \tag{62}$$

E[mi] = Mean Measurement

Var[mi] =Variance of Measurement

4.3.1 SNR for 16 Electrode System using LabVIEW based voltage source at 1V

Mean SNR = 26.45 dB

Peak SNR = 37 dB

Peak measured voltage: 5mV

Mean measured Voltage: 1.56mV

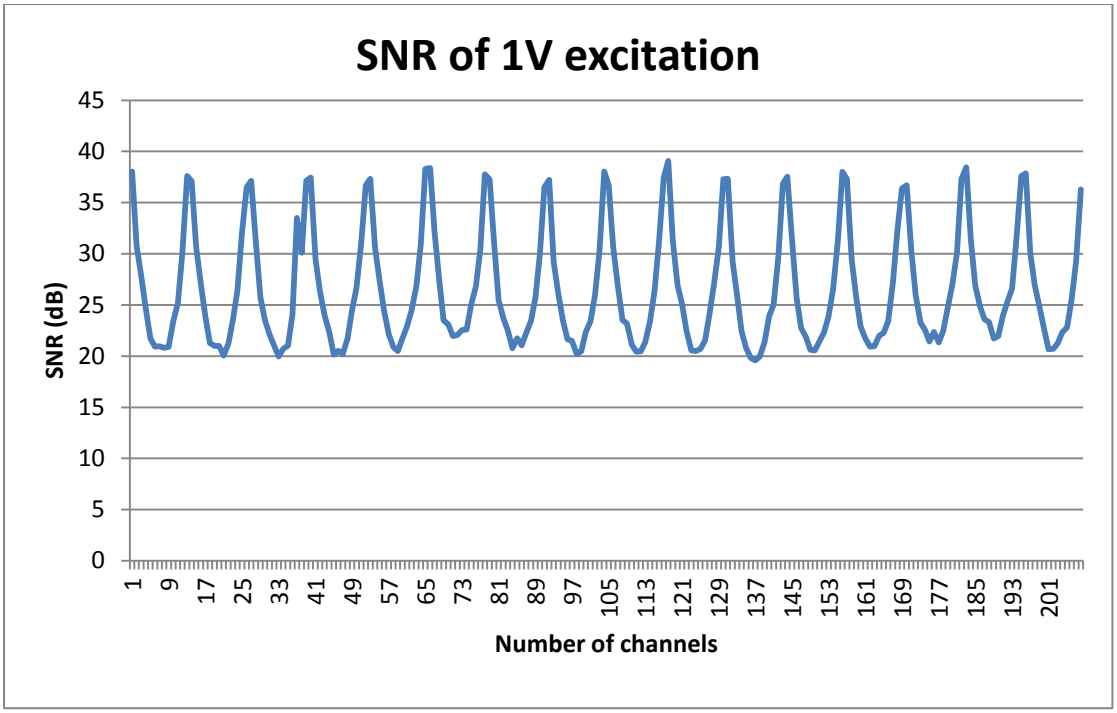

Figure 4.2: Signal to noise ratio for LabVIEW based voltage source at 1V

4.3.2 SNR for 16-Electrode system using LabVIEW based voltage source at 1.5V

Mean SNR = 32.38 dB

Peak SNR = 42 dB

Peak Measured Voltage: 13 mV

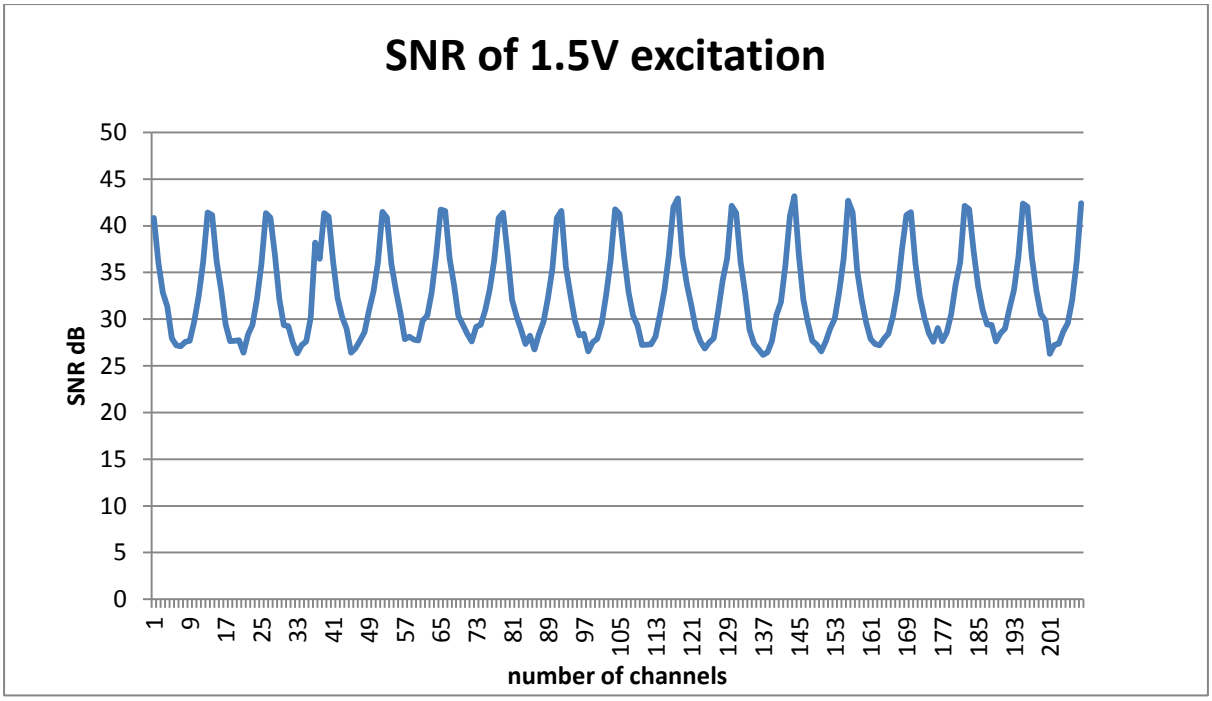

Figure 4.3: Signal to noise ratio for LabVIEW based voltage source at 1.5V

4.3.3 SNR for 16-Electrode system using current Source circuit at 1mA

Mean SNR = 22.3 dB

Peak SNR = 35 dB

Peak Measured Voltage: 3.7 mV

Mean Measured Voltage: 1mV

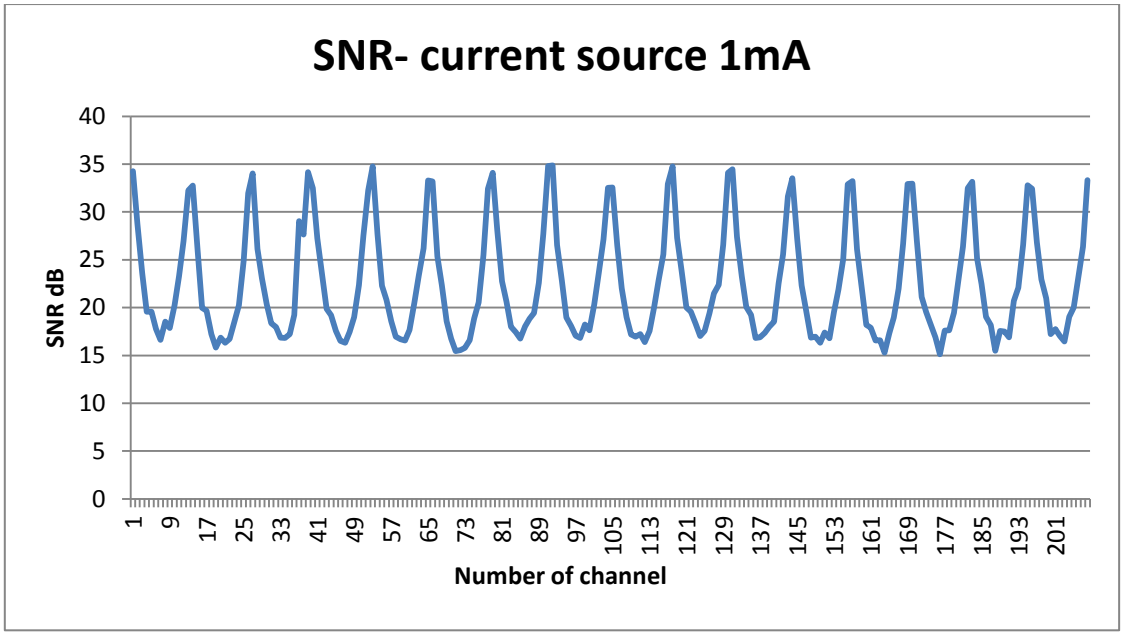

Figure 4.4: Signal to Noise ratio for current Source at 1mA

4.3.4 SNR for 16-Electrode system using current source circuit at 5mA

Mean SNR = 34.76 dB

Peak SNR = 48 dB

Peak Measured Voltage: 16 mV

Mean Measured Voltage: 4 mV

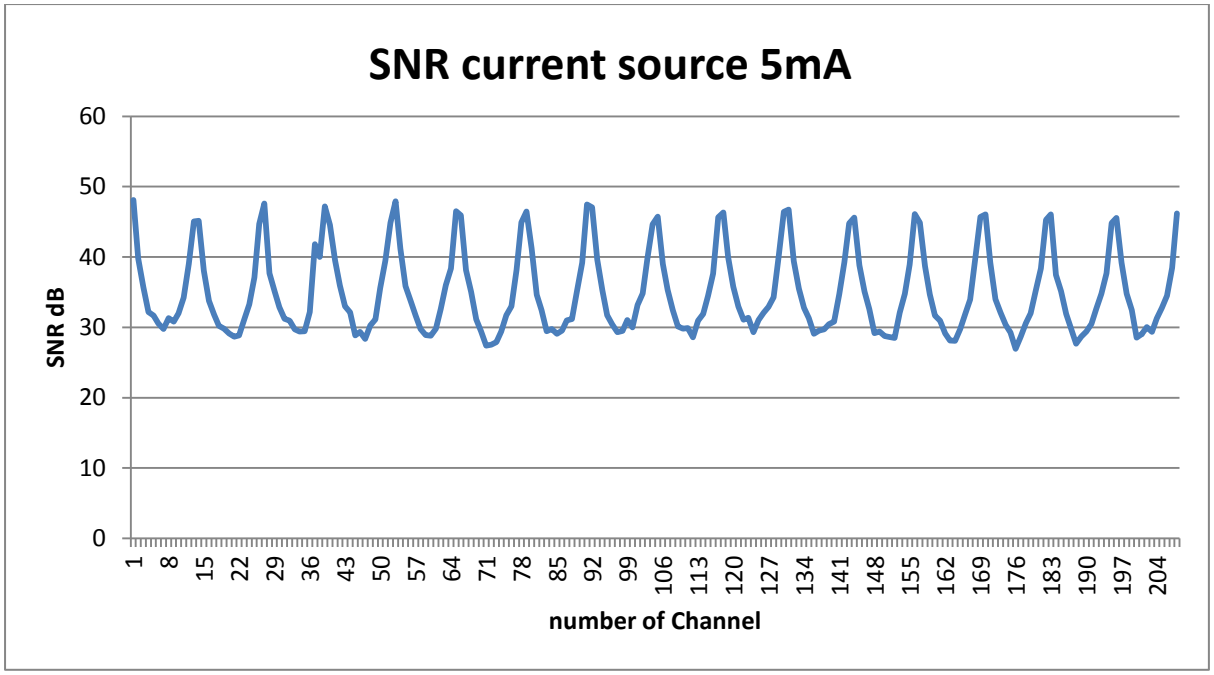

Figure 4.5: Signal to Noise ratio for current source at 5mA

In general, the results shown above indicated that signal-to-noise ratio is proportional to the excitation voltage used. 5mA current provides acceptable SNR considering that the test phantom and wiring is not perfect. One thing worth mentioning is, although the result may seem similar between the voltage driven system and current driven system, it is due to the test phantom's fixed boundary conditions and fixed impedance.

4.4 Phantom test Image reconstruction results

During this stage, all parts of the system are put through the test. The aim is to discover the system's adaptation with image reconstruction software and compare the results with further field test conditioned results.

4.4.1 Testing Method

For each experiment, two sets of measurements were taken for image reconstruction. The first set of measurements was a background reading, where the phantom was

only filled with saline solution. The second set of measurements was the data where the object/objects are placed within the phantom. The final reconstructed image was formed by comparing the background measurement and the data measurement.

Four experiment conditions were applied for every object layout:

1. 16-Electrode EIT System using LabVIEW based voltage source at 1V, 250Hz
2. 16-Electrode EIT System using LabVIEW based voltage source at 1.4V, 250Hz
3. 16-Electrode EIT System using current source circuit at 1mA, 250Hz
4. 16-Electrode EIT System using current source circuit at 5mA, 250Hz

High resistivity objects were placed into the phantom and images of these objects were created by using measured data from the phantom. The same objects were used for all experiments and maintained at the same location for accurate comparison.

Seven different object layouts were performed:

Test 1: Single object placed on the edge of the phantom

Test 2: Single object centred

Test 3: Two objects placed at far ends of the phantom

Test 4: Two objects 1cm apart

Test 5: Three objects

Test 6: Four objects

Test 7: Five objects

4.4.2 Results for 16-Electrode system using LabVIEW based voltage source at 1V 250Hz

In order to speed up the experiment process, the background reading was only performed once, which was at the very beginning of the experiment. Figure 21 shows the plot of background measurements.

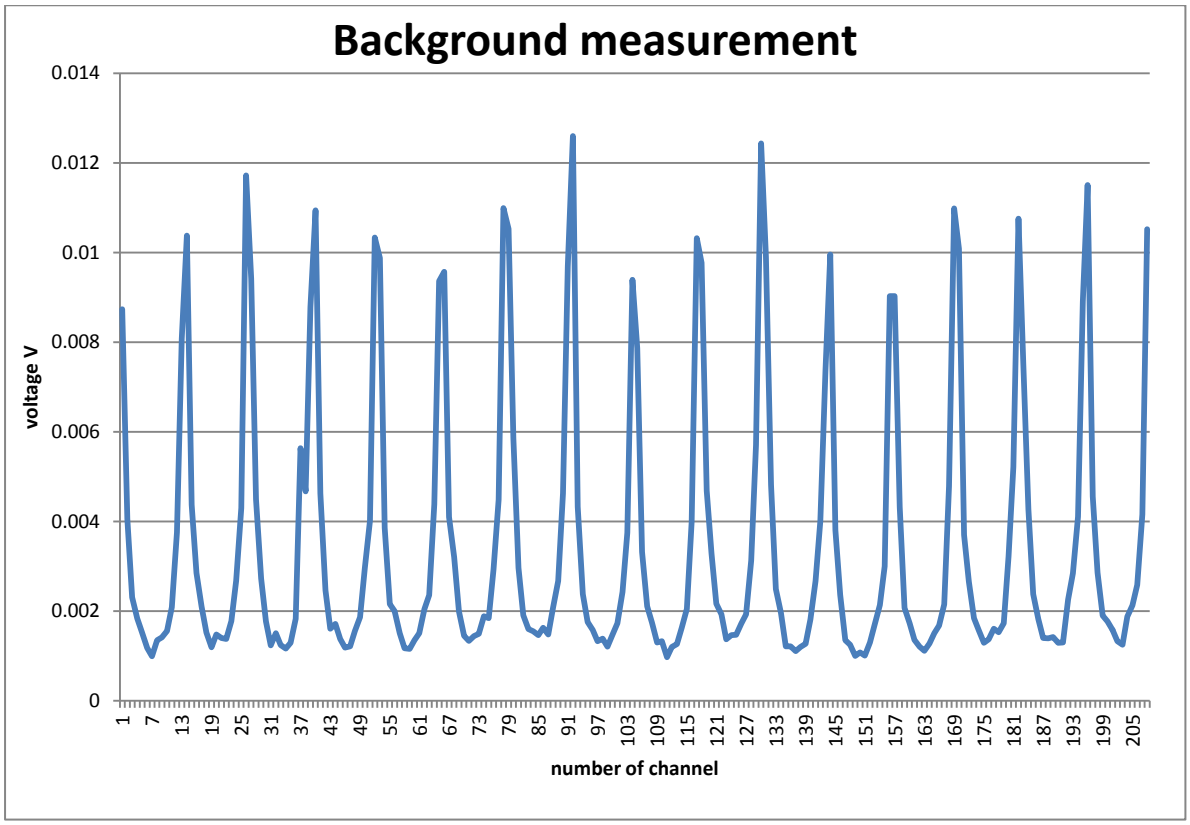

Figure 4.6: Background measurement for 16 Electrode system using LabVIEW based voltage source at 1V 250Hz

TEST	Reconstructed Image
Background	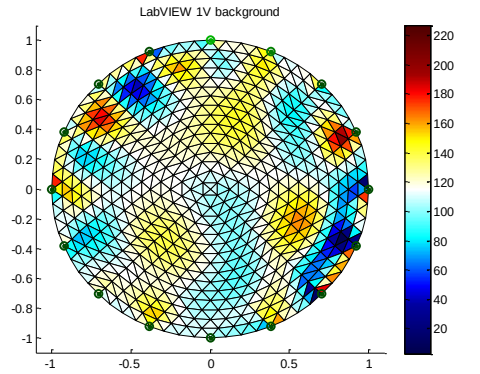
Test 1 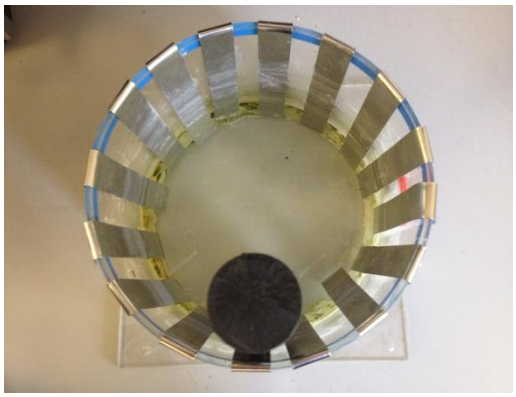	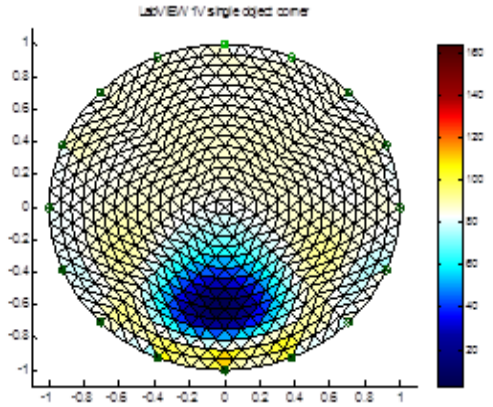
Test 2 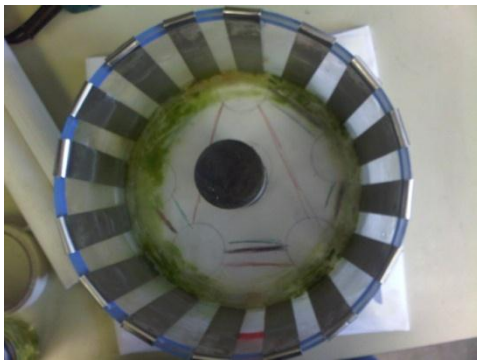	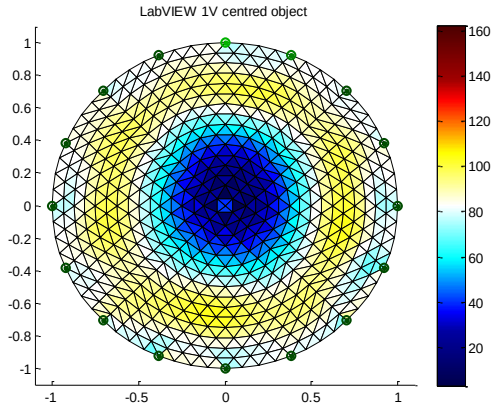

Test 3: 	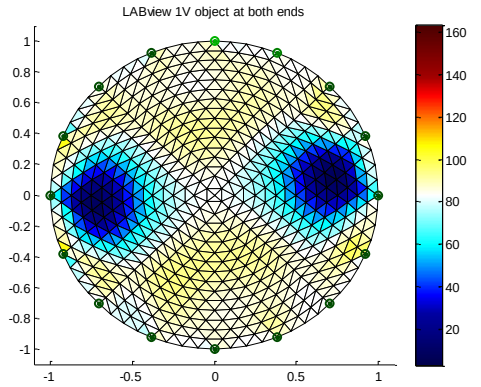
Test 4: 	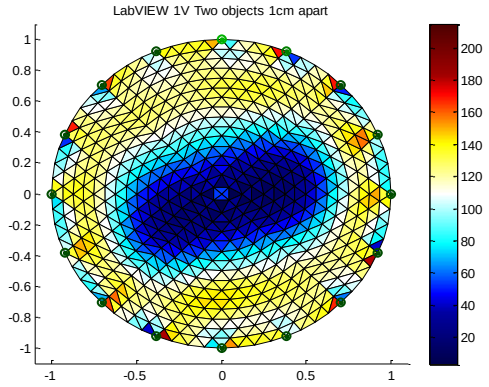
Test 5: 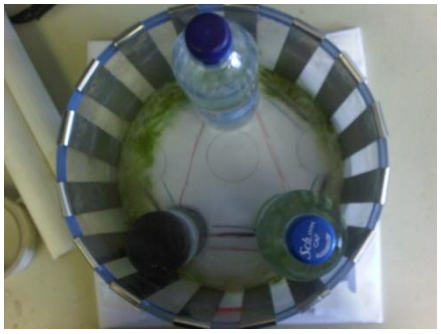	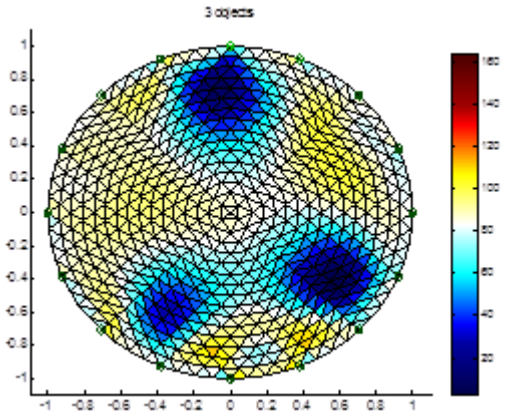

Test 6 – four objects 	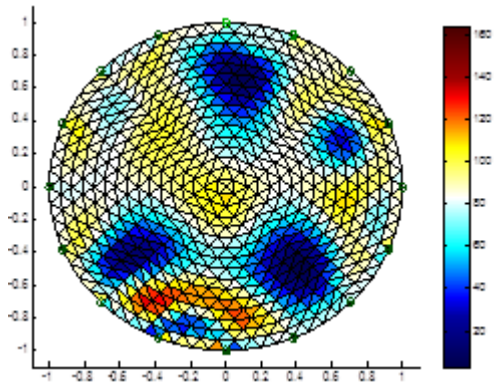
Test 7- five objects 	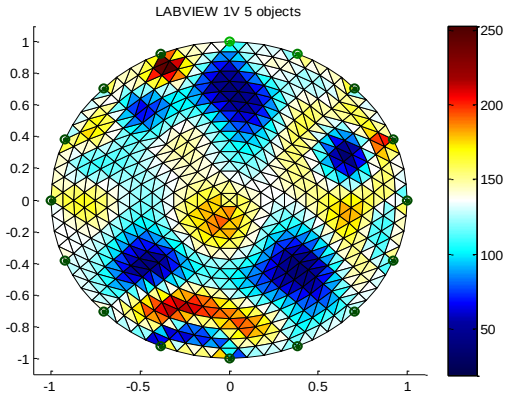

4.4.3 Results for 16-Electrode system using LabVIEW based voltage source at 1.4V 250Hz

Figure 4.7 shows the background measurement plot using LabVIEW based voltage source at 1.4V

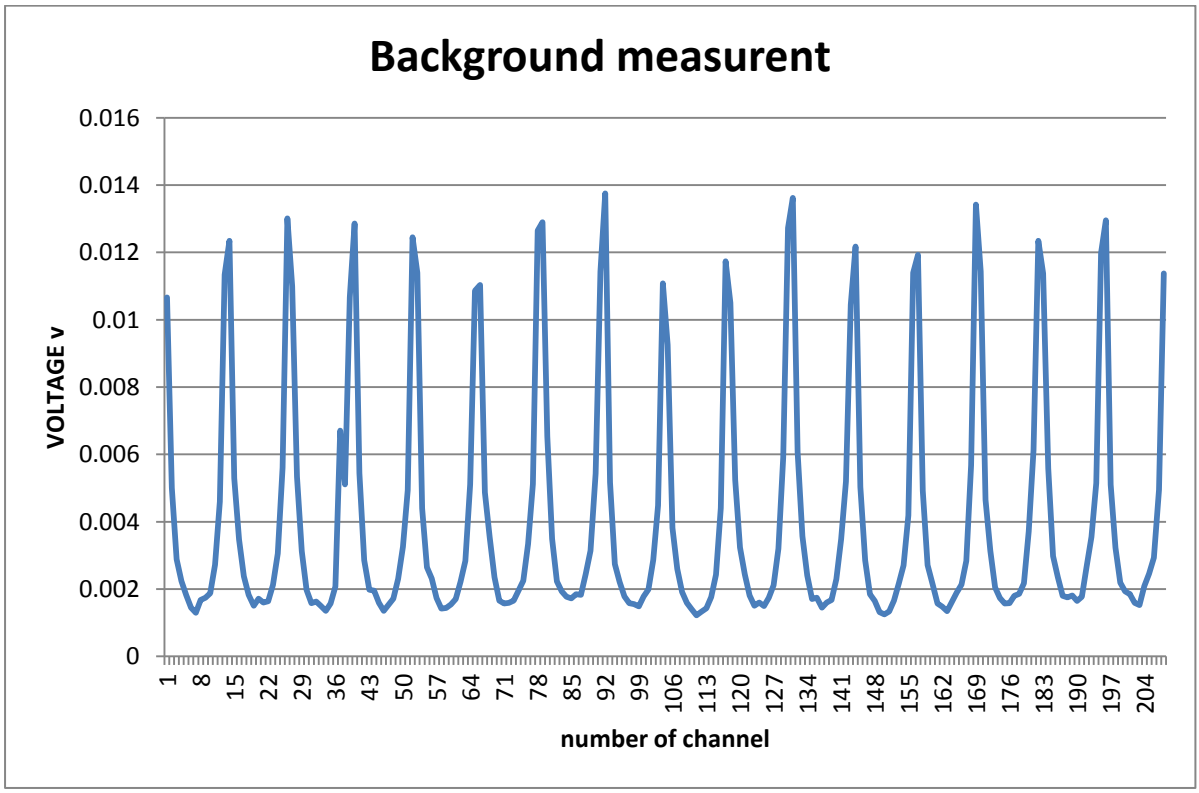

Figure 4.7: Background measurement for 16 Electrode system using LabVIEW based voltage source at 1.4V 250Hz

TEST	Reconstructed Image
Background graph	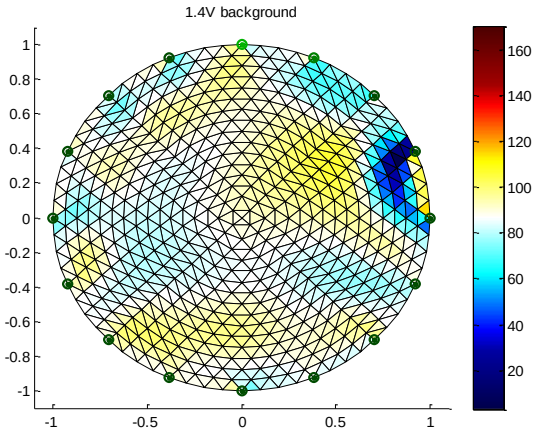
Test 1 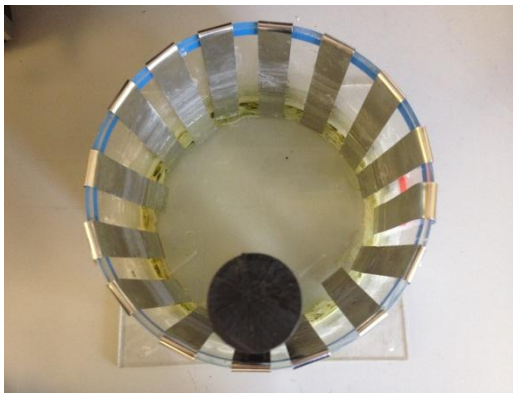	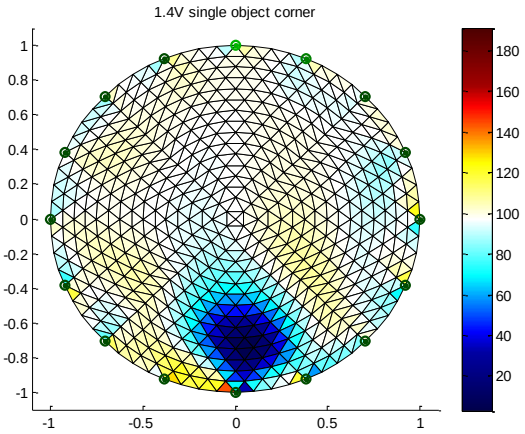
Test 2 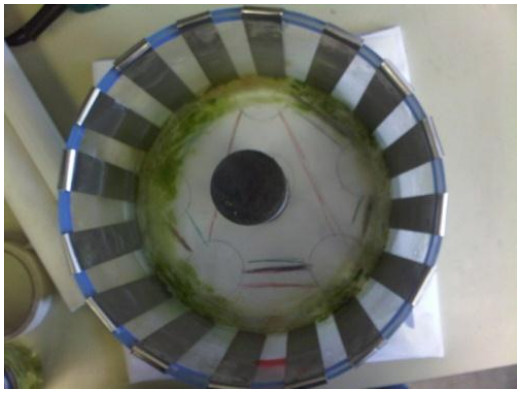	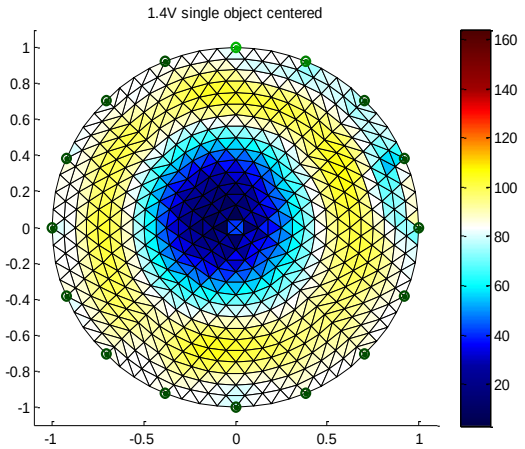

Test 3:

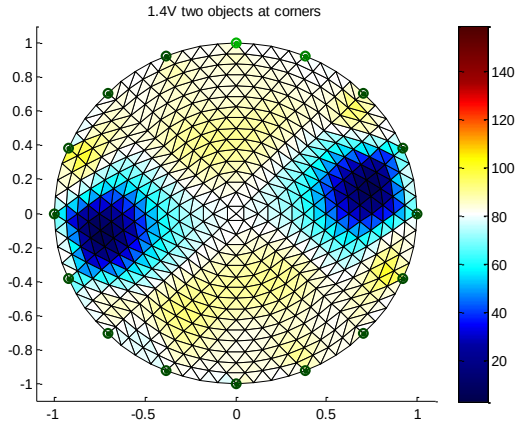

Test 4:

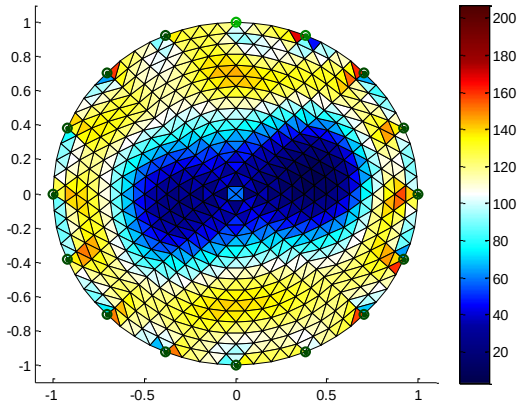

Test 5:

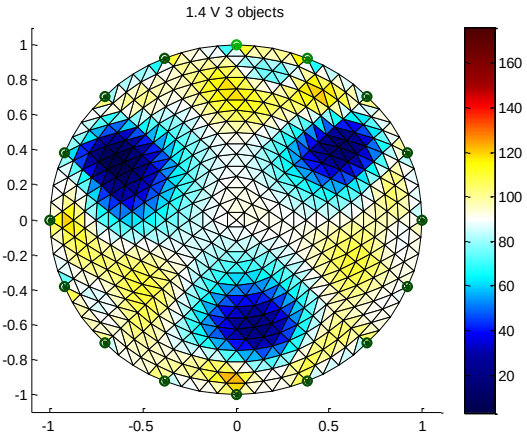

Test 6 – four objects 	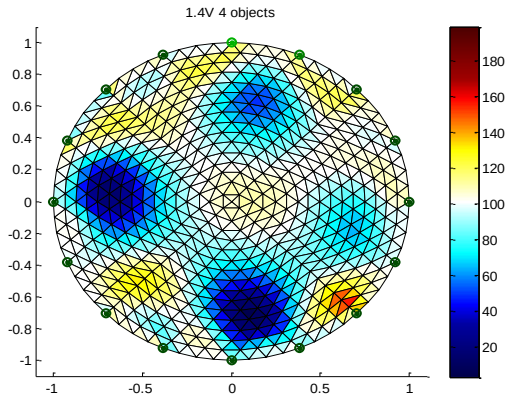
Test 7- five objects 	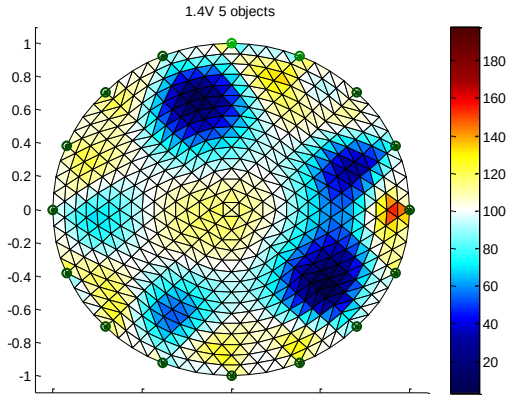

4.4.4 Results for 16-Electrode system current source circuit at 1mA 250Hz

Figure 4.8 shows the background measurement plot at 1mA

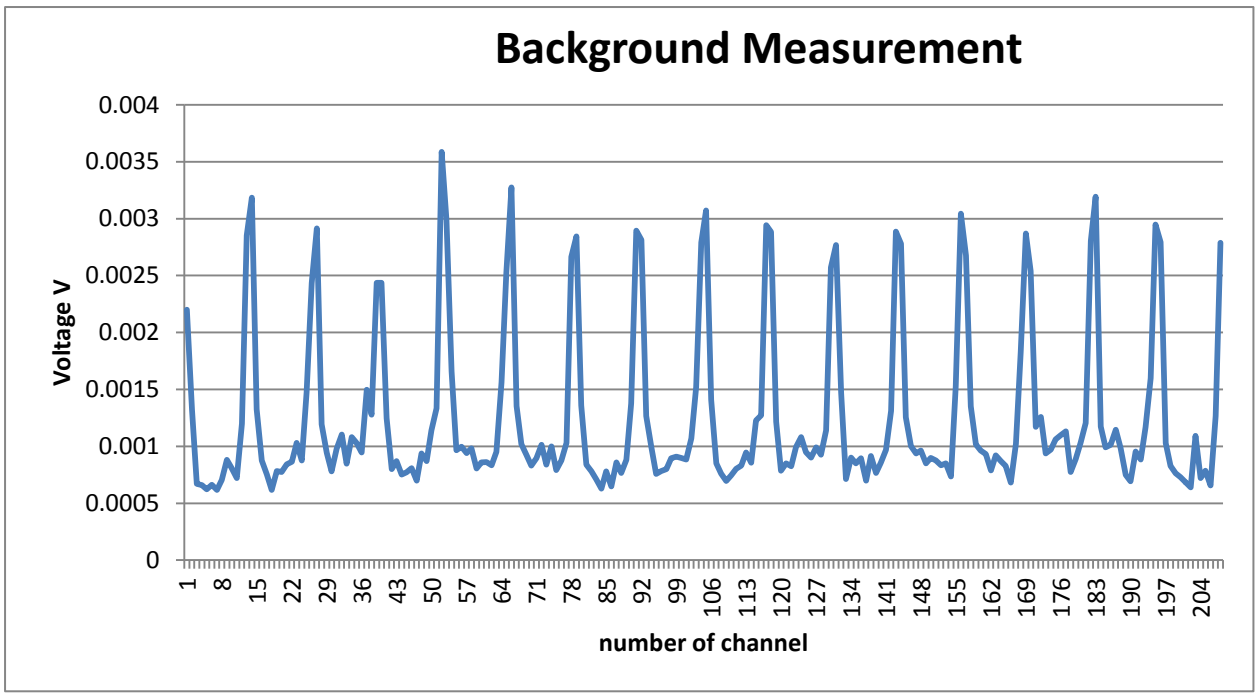

Figure 4.8: Background measurement for 16 Electrode system current source circuit at 1mA 250Hz

TEST	Reconstructed Image
Background graph	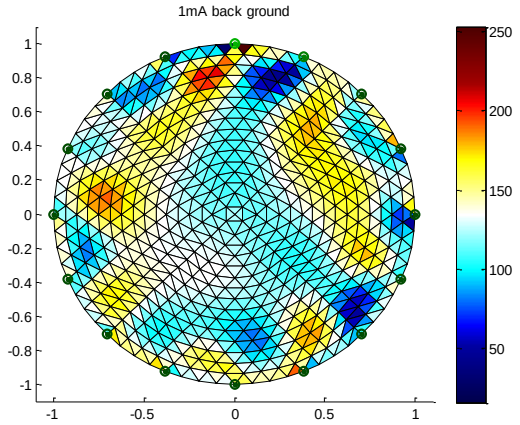
Test 1 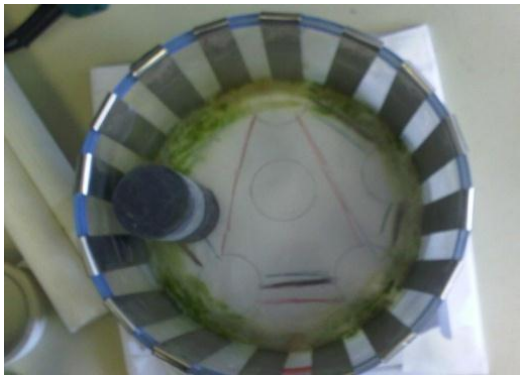	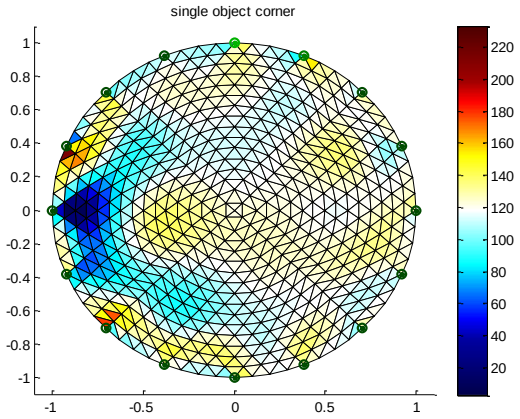
Test 2 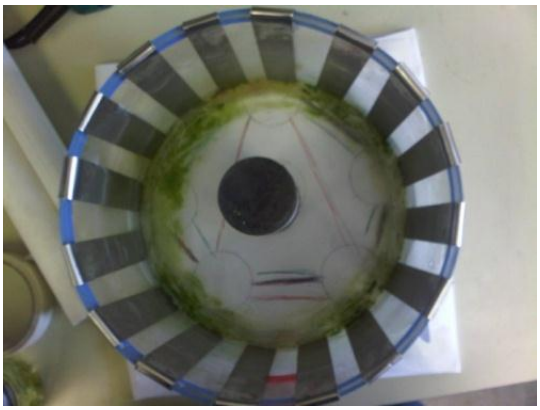	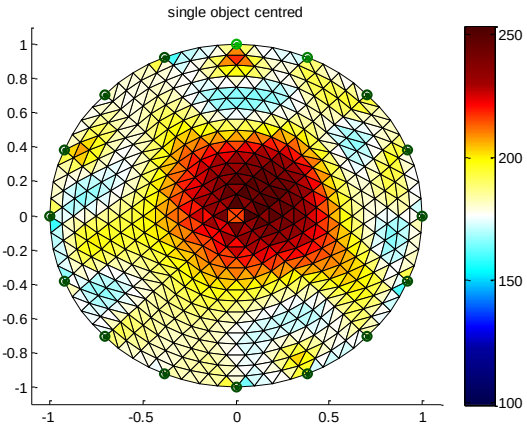

Test 3:

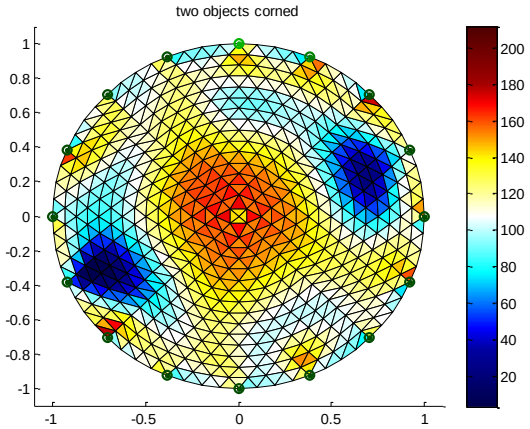

Test 4:

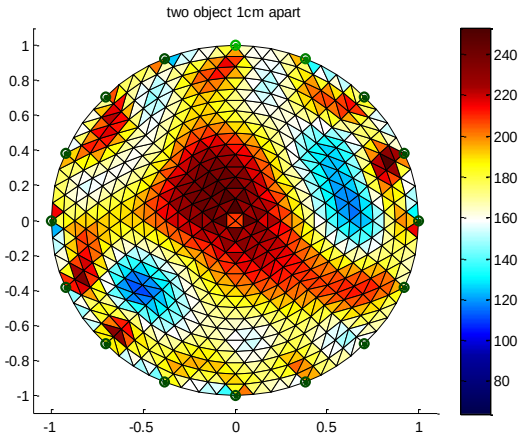

Test 5:

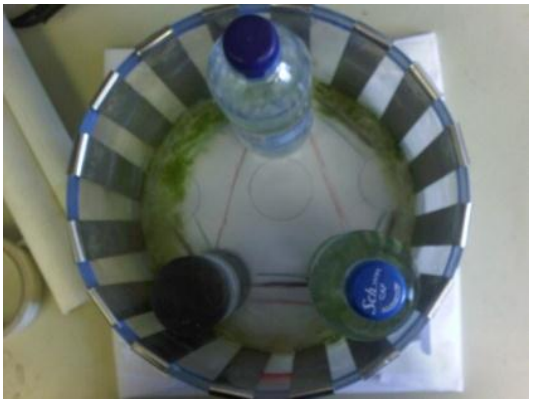

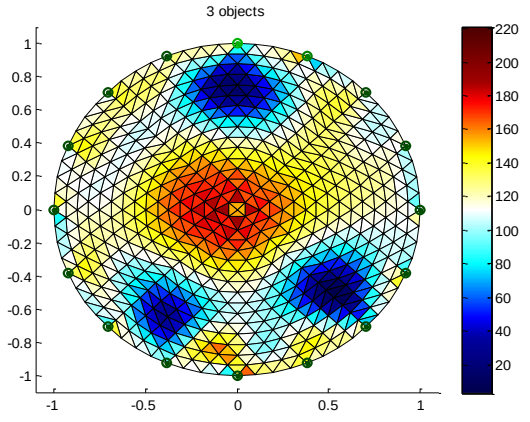

Test 6 – four objects 	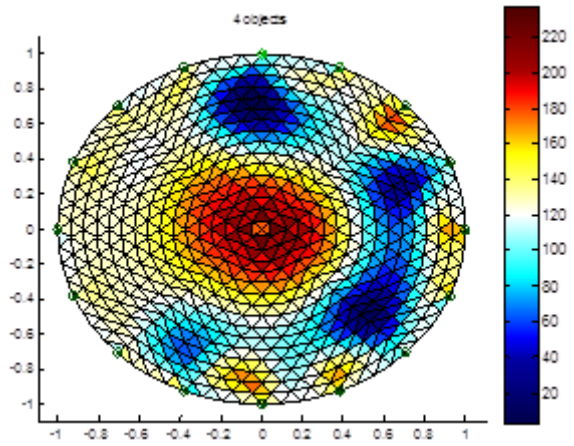
Test 7- five objects 	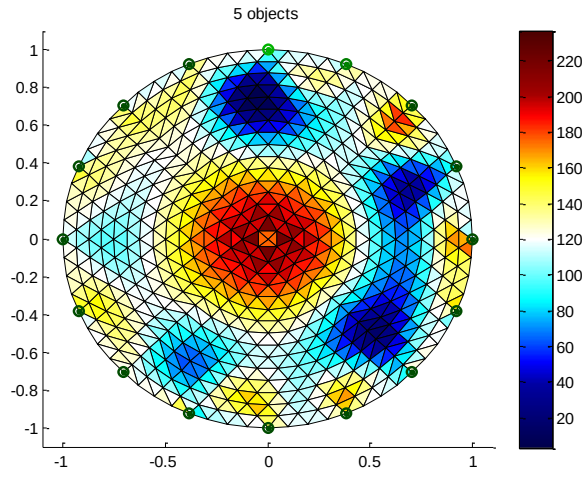

4.4.5 Results for 16-Electrode system current source circuit at 5mA 250Hz

Figure 4.9 shows the background measurement current source circuit at 5mA

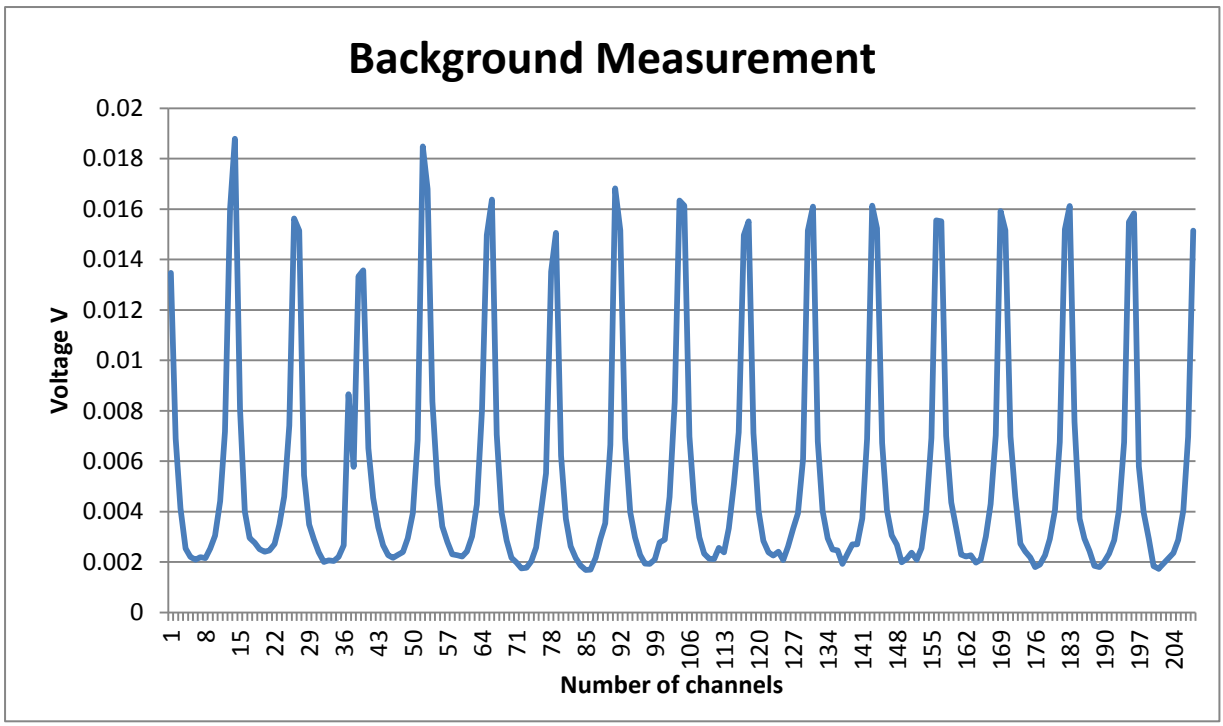

Figure 4.9: Background measurement for 16 Electrode system current source circuit at 5mA 250Hz

TEST	Reconstructed Image
Background graph	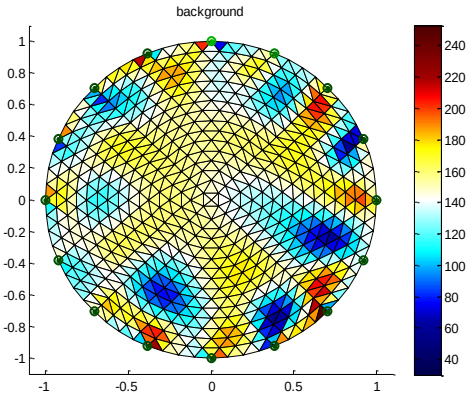

Test 1 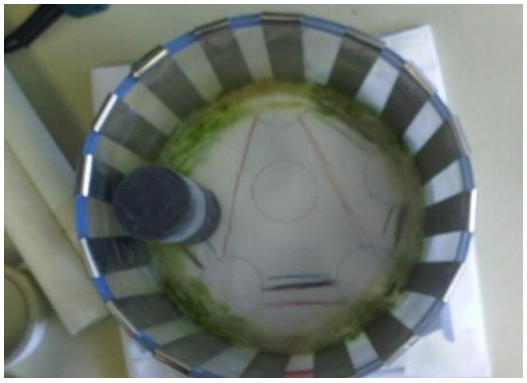	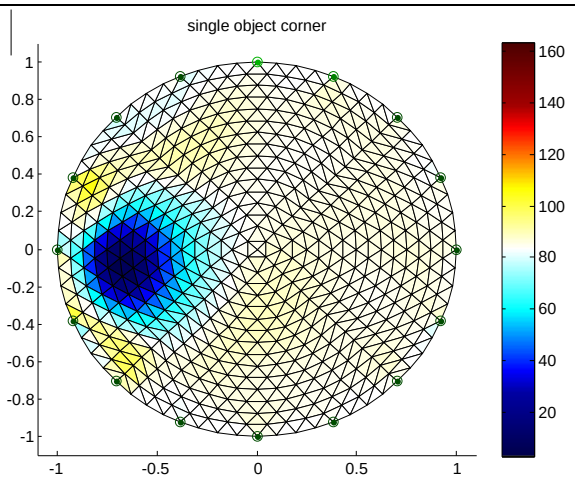
Test 2 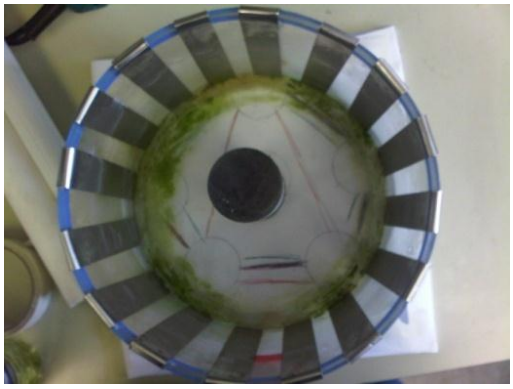	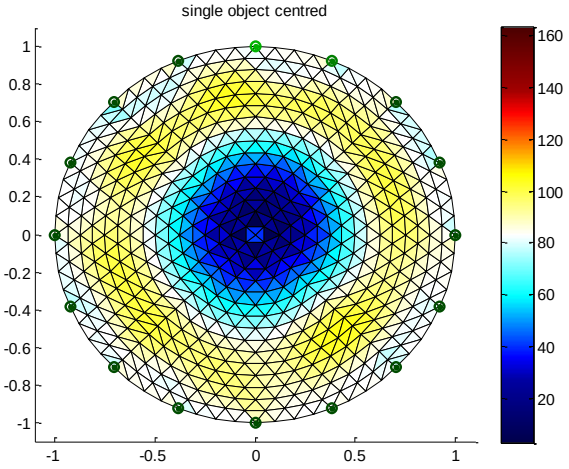
Test 3: 	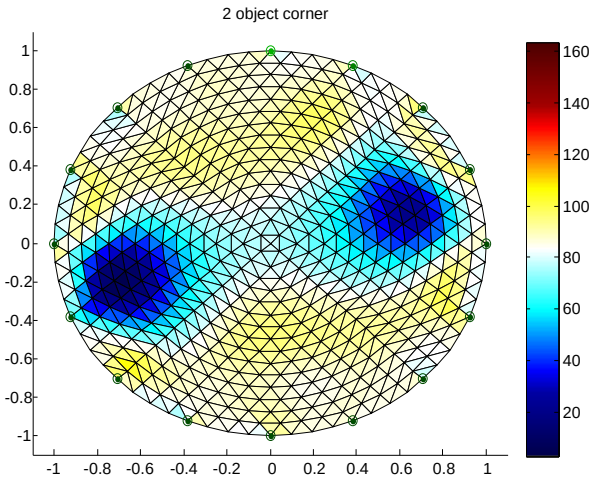

Test 4: 	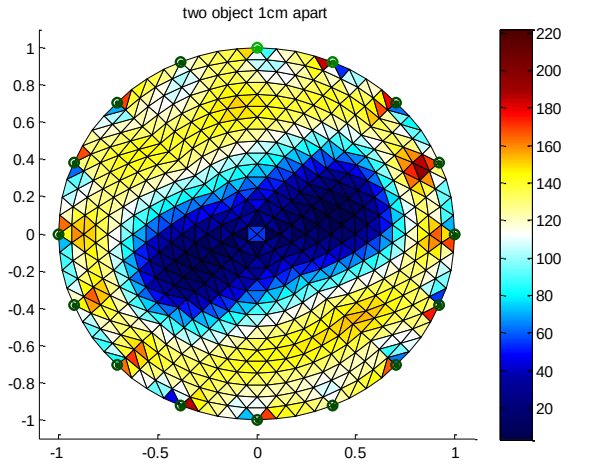
Test 5: 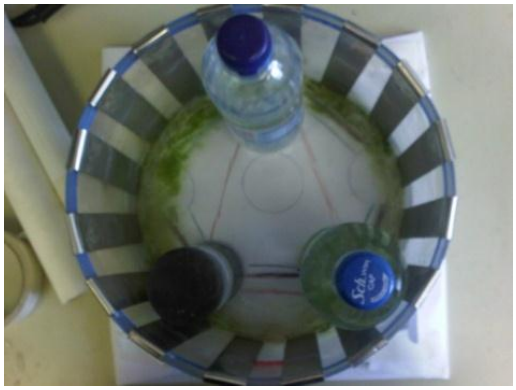	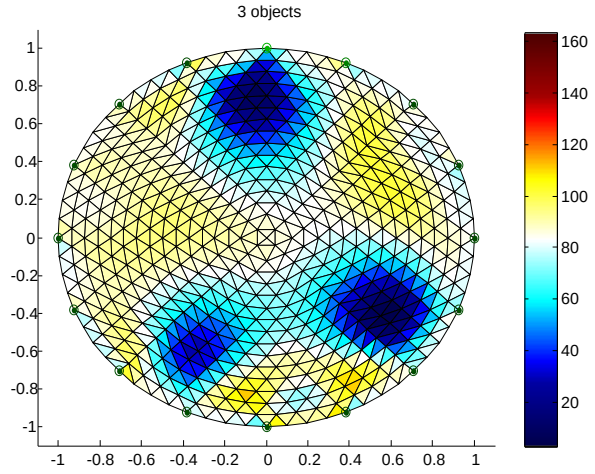
Test 6 – four objects 	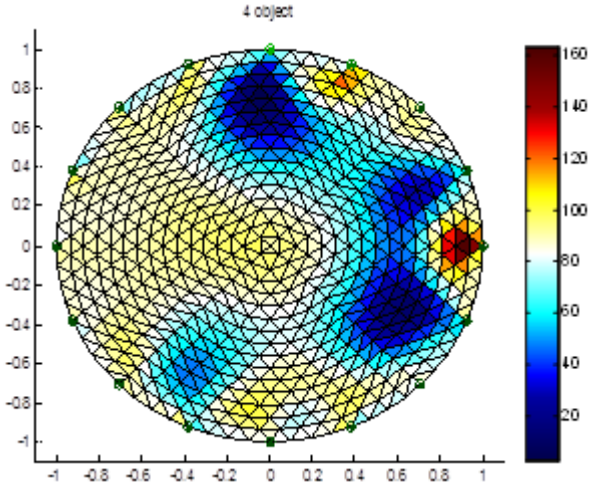

Test 7- five objects 	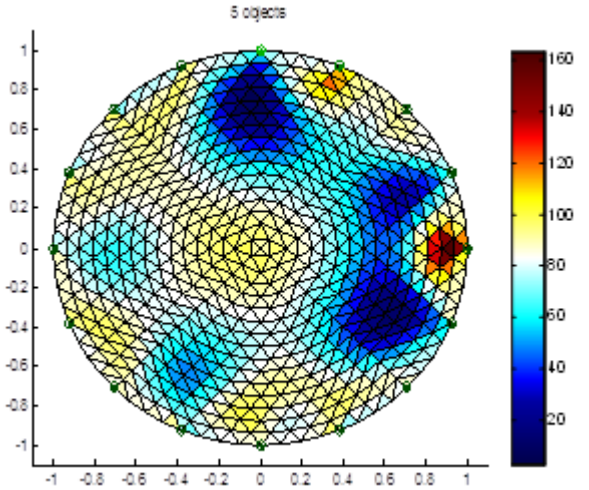

4.5 Conclusion

The results shown in this chapter matches our theory, which states that an increasing of excitation voltage or current would result in an increase in the measured voltage, hence a stronger detectability of testing objects. The result of Test 4 under both experiment conditions shows that the system is incapable of separating two objects if they are too close (1cm apart). Although the image quality can be improved by increasing the excitation current/voltage, it is limited by the Max current supply capability of our Data Acquisition Card, which is 5mA. As shown in the results, excitation voltage/current has an influence on detectability of objects as their number increases in the phantom. In the results of current source at 1mA, 5 objects were placed but noise was also contained and the image result was not satisfied unless regularisation parameters on EIDORS software were altered. The images produced at 1mA current level were unreliable and accuracy was low due to low SNR, therefore the idea arose to use the maximum current level. Also, the size of the testing objects was vital for image reconstruction as seen from result of 5 objects; the smallest tube was scarcely visible even at 5mA current level. In general, all

results were very similar but the LabVIEW-based voltage source was limited to the maximum current supply of 5mA, therefore, in order to operate at higher currents, it is essential to use a current source circuit. The phantom experiment in here was used in dual EIT-CT combination presented in [100], in which a motion compensated CT image was created by using this EIT system.

Chapter 5

5. Deformation Sensitive Fabric Sensor

This chapter presents the application of a wearable EIT system that works by imaging textile structures made of electrical conductive areas (ECA)[101]. The current generation of textiles, including technical textiles, are passive [102-106]. However, the next generation of textiles will have the ability to monitor their environment and interact accordingly in order to accomplish a pre-programmed functionality. Such textiles can be considered as truly smart textiles. They will contain three basic components:

- Sensing and Measuring Ability
- Activation Capability
- Intelligence (programmable)

One way of incorporating these into a textile structure is to create electrically active zones within the structure, where its electrical characteristics can vary due to environmental changes or its structural properties can be changed by the application of an electrical signal, such as a change of dimensions when an electrical current flows through the electrically active area. Generally, textiles are made out of materials with very high electrical resistance; these structures can therefore be

considered as materials with good electrical insulating properties. Reconstructed images from test results will be shown and discussed at the end of the chapter.

5.1 Sensor Implementation

During the early stage of our design process, we looked into several different materials which could be ideal for our application since we didn't have the means to produce fabric ourselves. To be able to be used as the main structure of our sensor, this fabric needs to have a few key features:

- Conductivity
- Pressure sensitive
- Available in a large quantity

After searching the internet, we found a conductive material developed by Less EMF Inc. This material is a highly conductive medical–grade silver–plated Nylon Dorlastan fabric with the ability to stretch in both directions. It has a surface resistivity of approximately 1.0Ω per square meter and this value would change if stretched or compressed.

Since the sensor will be pressed and dragged all over when testing, a wooden frame was built to accommodate the fabric so it would maintain the same position after each test. The frame is formed by two pieces, a top plate and a bottom plate. Both have the middle part cut out to fit the circular shaped sensor. Four bolts were used to clamp the plates together and 16 copper stripes were taped around the fabric to form electrodes. Figure 5.1 shows the system setup and Figure 5.2 shows the internal structure of the fabric sensor.

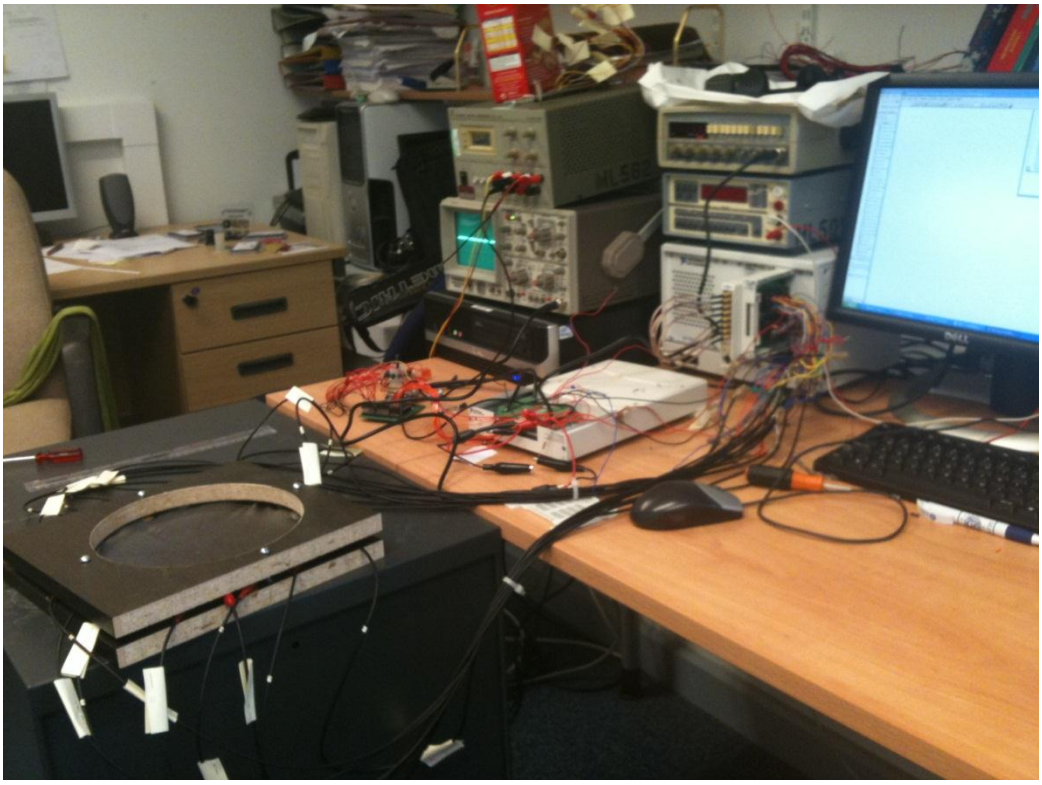

Figure 5.1: System setup

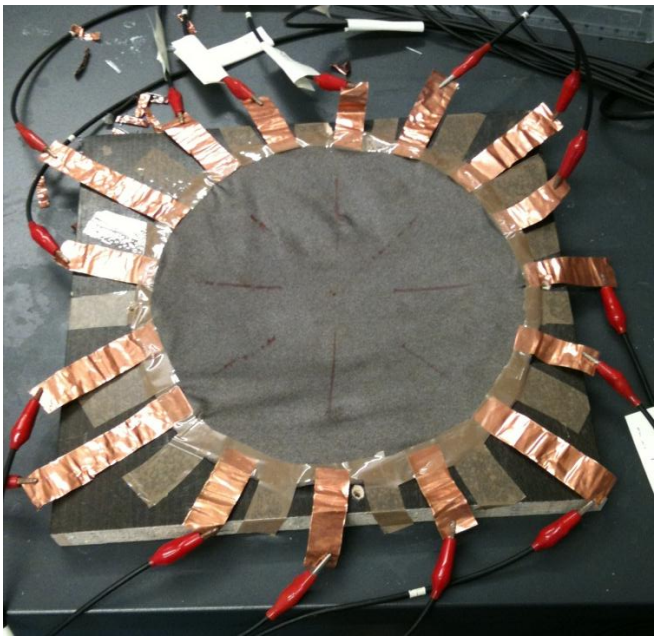

Figure 5.2: Sensor structure without the top wooden plate

5.2 Single and Multiple Object Imaging

Since this fabric is stretch sensitive, it can only detect the object when visible deformation has occurred.

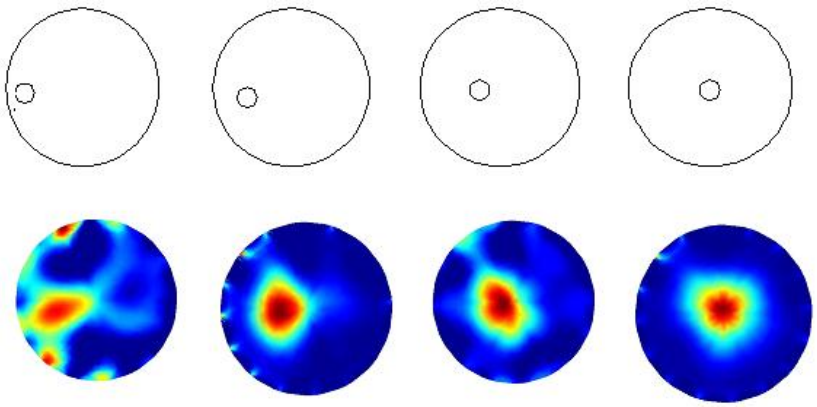

Figure 5.3: Pressure applied at four discrete points

Fig 5.3 shows a reconstruction of the location of a pressure point moving from the left-hand side to the centre of the conductive region. The pressure was applied to an area of approximately $1cm^2$. The results in Figure 5.4 show that the pressure can be detected and, as expected, show some differences in shape depending how far we are from the centre. There are also strong traces of the electrodes for pressure applied close to the boundary, suggesting that the pressure also creates deformation close to the electrodes, which are the most sensitive areas.

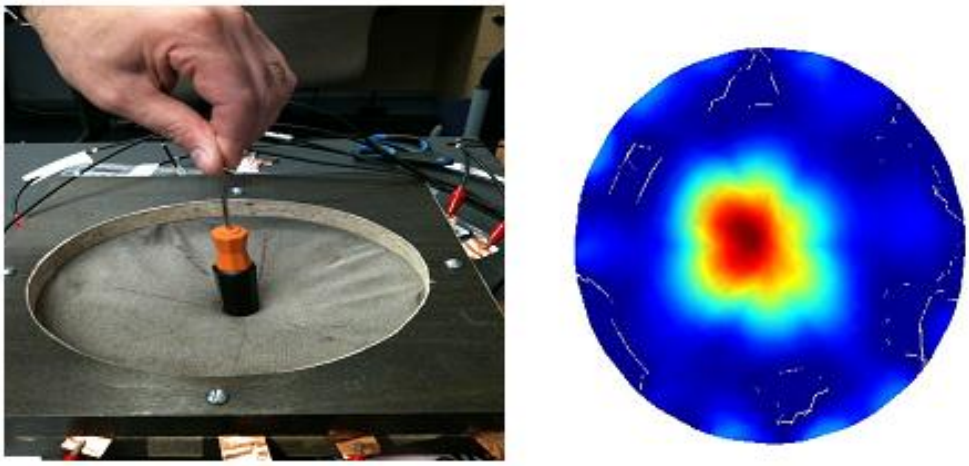

Figure 5.4: Pressure applied at the centre of the sensor

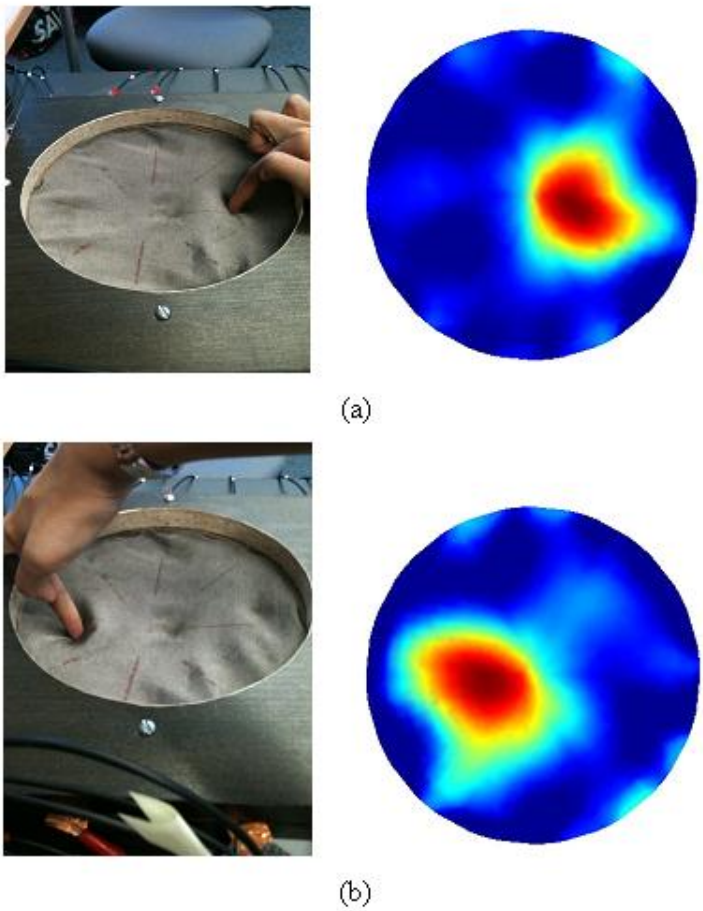

Figure 5.5: pressure applied at (a) Right-hand side and (b) Left-hand side

Figures 5.4, 5.5a and 5.5b show the reconstruction of applied pressure and the deformation of the fabric as a result of a single object.

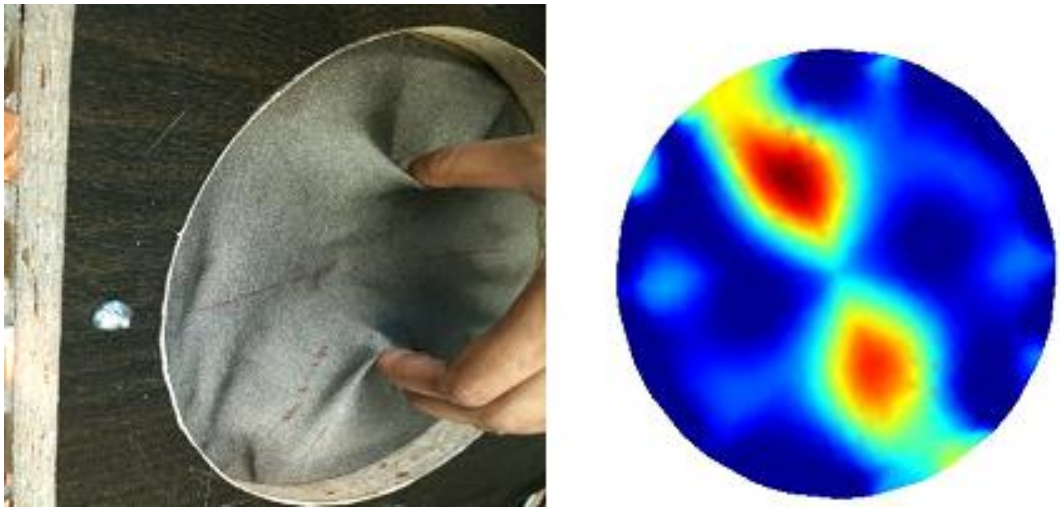

Figure 5.6: Pressure applied simultaneously at two opposite points

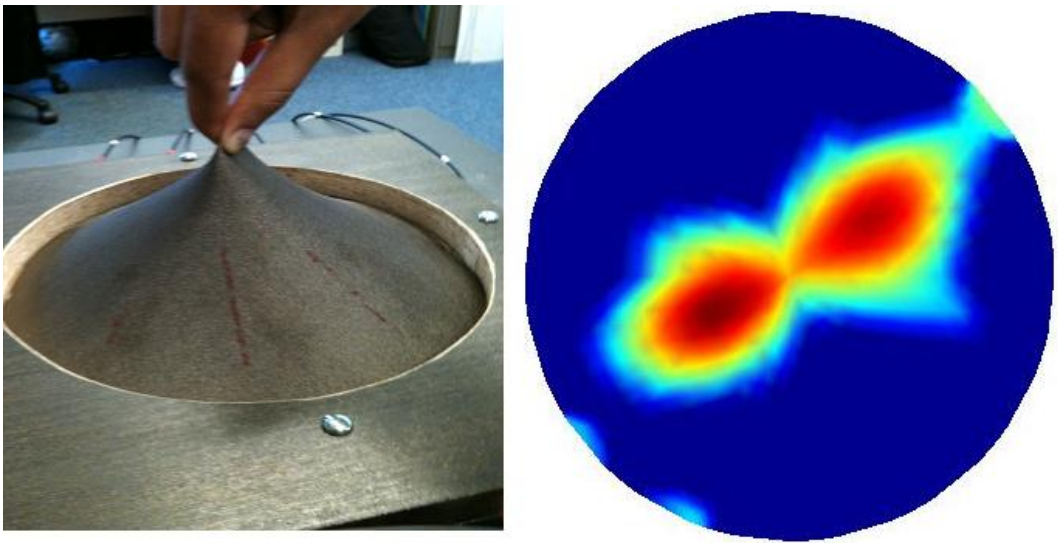

Figure 5.7: Sensor middle section been dragged upward

Figure 5.6 demonstrates a two pressure point image on the fabric sensor and, interestingly, for Figure 5.7, which is pulled updward in the middle section with two fingers, a similar result on the reconstructed image was created. We suspect this is due to the fact that the nature of this fabric is stretch sensitive, and, by pulling the middle section upward, a dragging effect is created on both sides of the point and therefore recorded by the system. This also shows that the system is ineffective when distinguishing between pushing and pulling since both actions create a similar deformation effect.

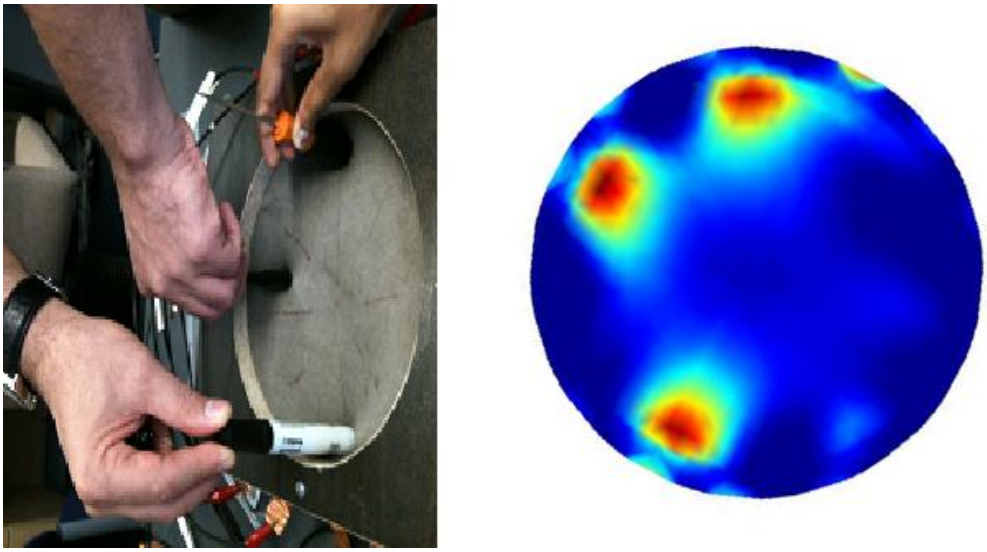

Figure 5.8: Pressure applied at three points simultaneously

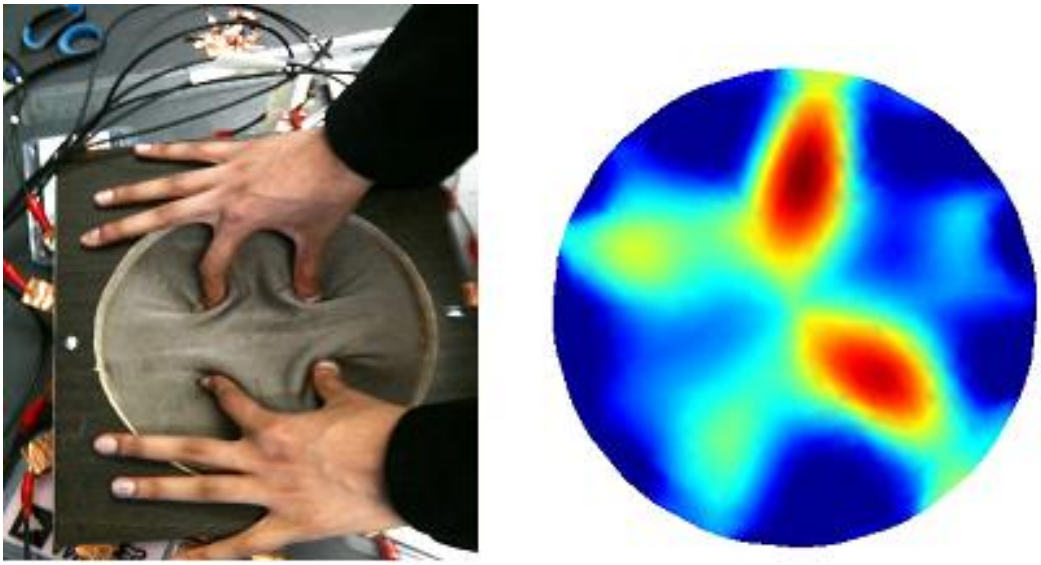

Figure 5.9: Pressure applied at four points (with varying forces)

Figures 5.8 and 5.9 are the result of multiple pressure points. Fig 5.9 also illustrates the range of pressures applied through different fingers and is able to reconstruct, for example, how much stronger pressure applied with the thumbs is.

5.3 Quantitative Analysis Test

To investigate the possible quantitative image analysis, experiments were carried out by two circular shaped scaled weights. The position of the weights is indicated in Table (a), and the quantity of the weights increased from 100g to 500g with 100g increment.

(a)	(b)100g of weight
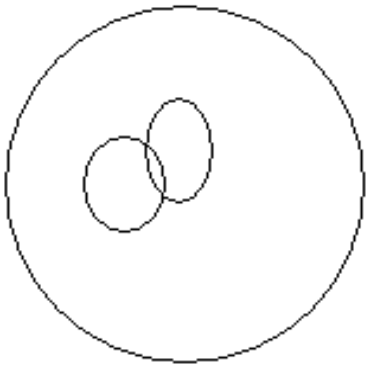	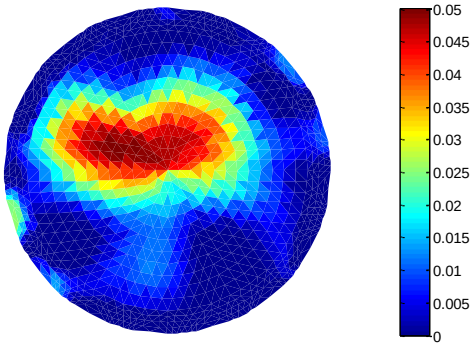
(c) 200g of weight	(d) 300g of weight
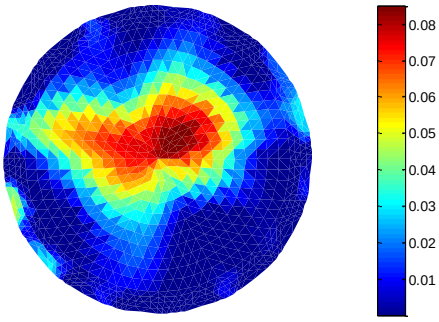	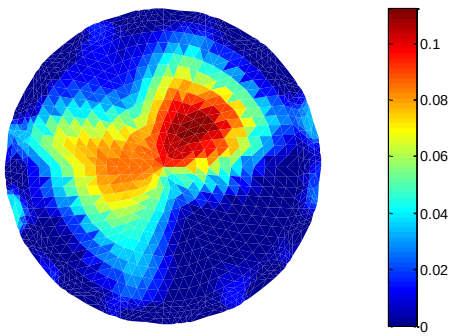

(e) 400g of weight	(f) 500g of weight
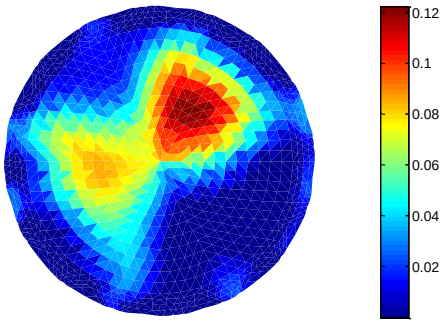	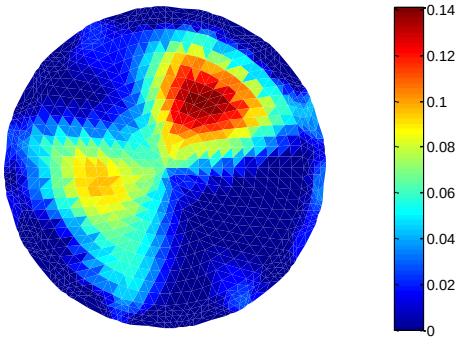

The reading on the scale bar of the resulted image shows an increase in imaging values on the location of that circle as the weight increases. The result also suggests further expansion of the deformation area which is expected with the increase of the weight applied.

5.4 Conclusion

The images produced by our system demonstrate the feasibility of the EIT system for pressure and deformation mapping imaging. In particular, the results showing reconstruction of multiple pressure points are very promising. The results suggest that quantisation of the pressure profile may be possible, but it is still very challenging. The results of image quantisation and its relationship with the pressure profile is encouraging but not sufficiently convincing.

Chapter 6

6. Pressure Sensitive Fabric Sensor

As the previous phantom tests and initial stretchable fabric sensor design have shown us how promising the result could be under the right conditions, we wanted to try another approach by building the pressure sensitive fabric sensors. Previous attempts have been made by others using silicone-based conductive glue with Ag fillers[104] or Polymer -carbon - nanotube composites[107]. Instead of following those approaches, we decided to use an off-the-shelf conductive fabric called EEONTEX^{TM} Conductive Nonwoven Fabric with the model number EeonTex^{TM} LR-SL-PA-10E5[108]. This fabric is a knitted nylon/spandex coated with a conductive formulation. The surface resistivity of this fabric is $10^5\Omega$ per square meter. This level of resistivity is suitable for our application since it provides a large contrast under pressure between the pressure point and the rest of the fabric, and hence provides a clearer image.

6.1 Sensor Implementation

To utilise this fabric, we first cut it into a circle, then attached it to a double wooden ring where the fabric was clamped in between the rings by a metal screw (Fig 6.1).

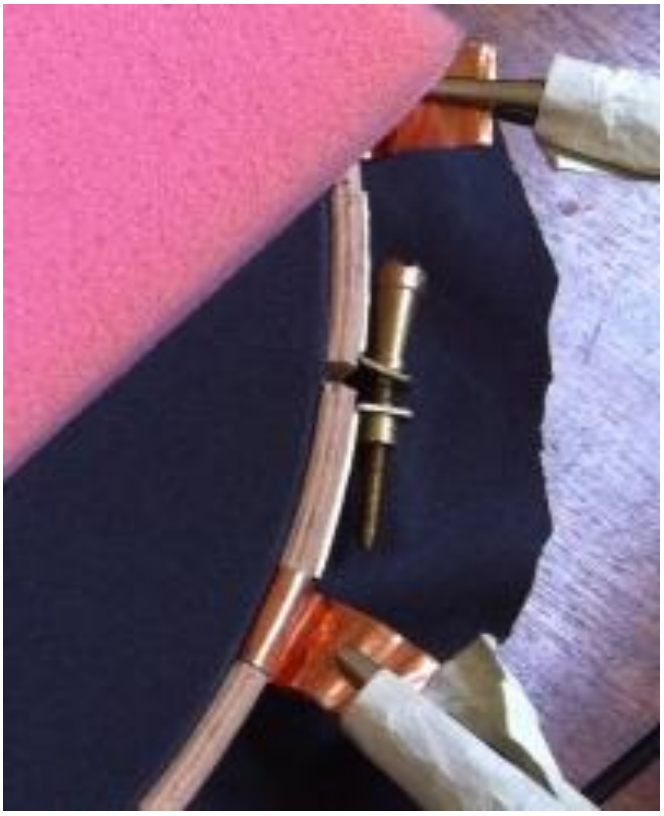

Figure 6.1: Enlarged picture for the Metal Screw that ties the clamping ring of the fabric sensor

Sixteen copper strips were wrapped around the wooden ring to form electrodes. A picture of the fabric sensor is shown below in Figure 6.2.

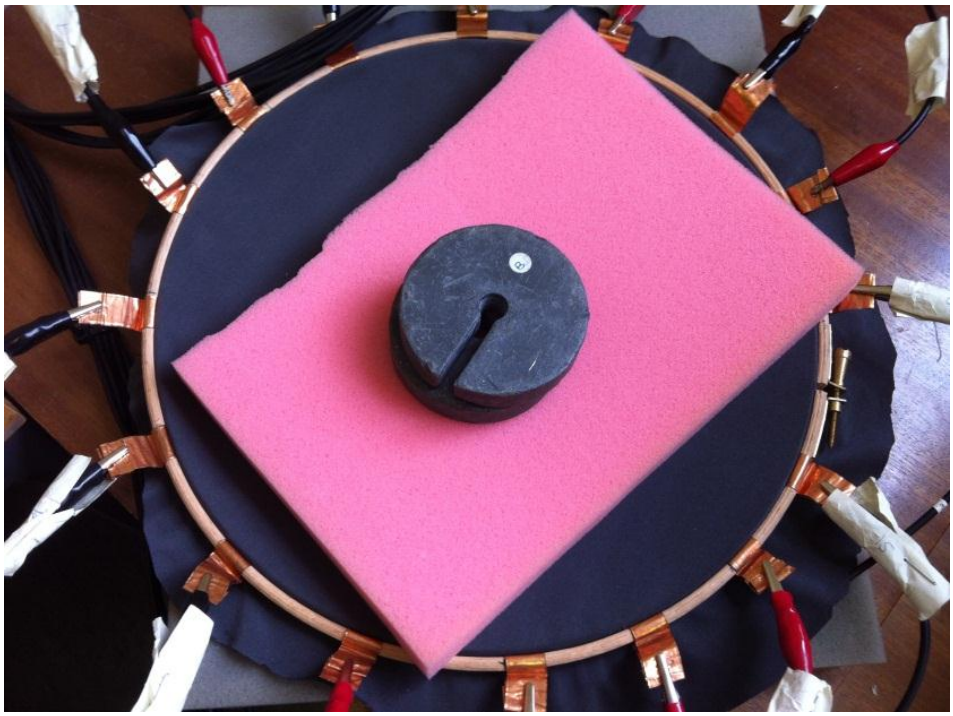

Figure 6.2: Picture of the Fabric Sensor

6.2 Sensor Performance Test

After completing the construction of the fabric sensor, a series of tests were carried out to obtain data on the sensor's performance.

6.2.1 Signal to Noise Ratio Test

Mean SNR = 31 dB

Peak SNR = 48.89 dB

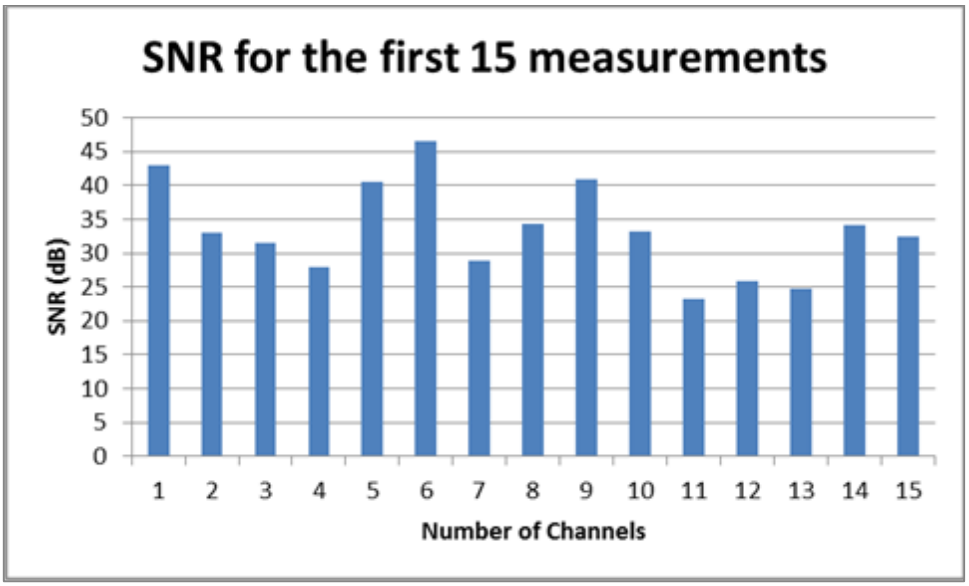

Figure 6.3: SNR of the first 15 measurement from Circular Sensor with 16 electrodes

6.2.2 Single and Multiple Object Imaging

Initial tests were aimed at reproducing similar results to those from the phantom test where testing subjects were visible within a reconstructed image. Heavy objects were placed on the sensor and previous experiences showed that heavy objects tend to lean to one side if placed directly on to the fabric. In order to ensure pressure was distributed evenly over the sensor, two sponge pads were placed both under and over the sensor. The sponge pad on top was cut to fit within the area of the sensor so weight could only be passed on to the sensing area. All weights were

placed on top of the sponge, meaning the weight would sit nicely on the sensor without leaning or sliding to the side which can cause distortion in the result image. Figure 6.4 shows the background measurement data of the fabric sensor.

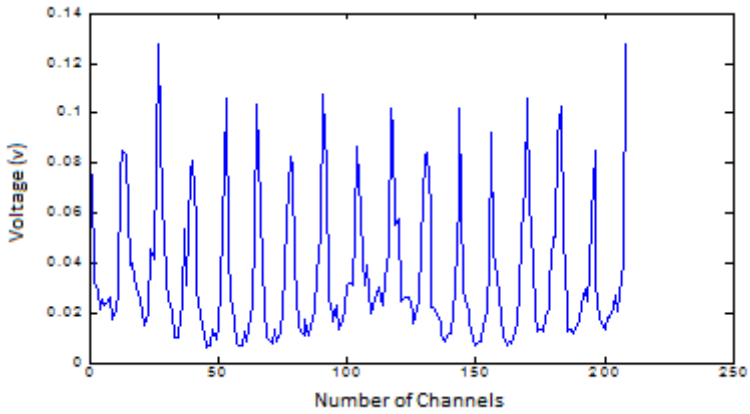

Figure 6.4: Background Measurement data of the fabric sensor

The testing sequences are:

- A single object placed on the top right corner of the sensor.
- A single object placed on the bottom left corner of the sensor.
- A single object placed on the top left corner of the sensor.
- A single object placed on the bottom right corner of the sensor.
- Three object stacking on top of each other and placed on the center of the sensor.
- Two fingers pressed on the lower right position of the sensor.
- Two objects placed at each end of the diagonal line of the sensor.

TEST	Reconstructed Image
Single object placed on top right corner 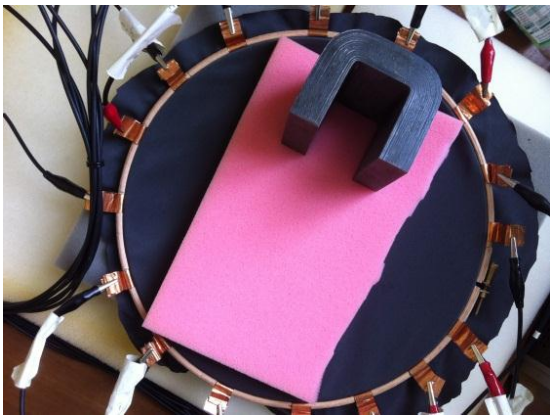	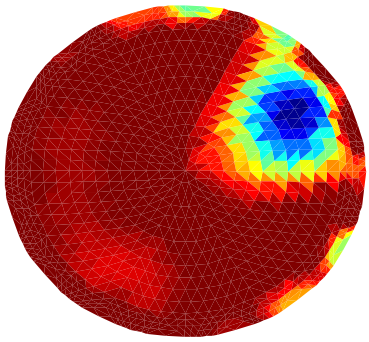
Single object placed on bottom left corner 	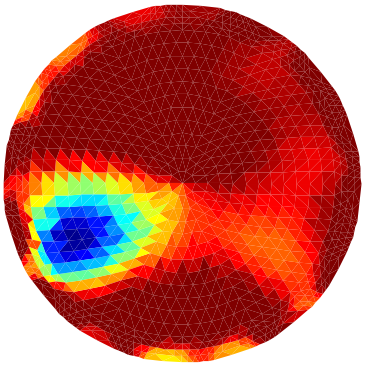
Single object placed on top left corner 	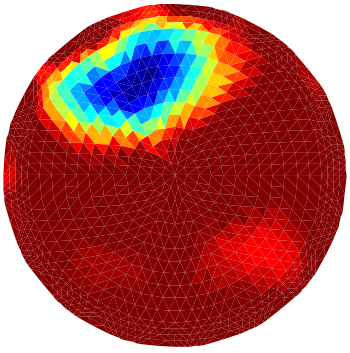

Single object placed on bottom right corner 	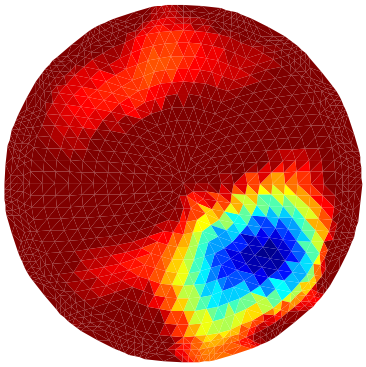
Multiple objects stacking in the middle 	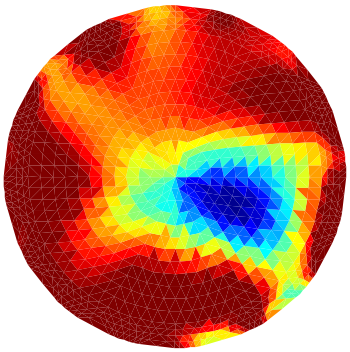
Two fingers pressed on a lower right position 	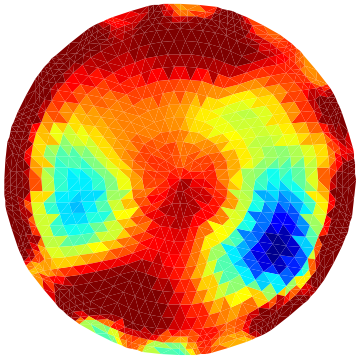

Two objects placed along the middle line 	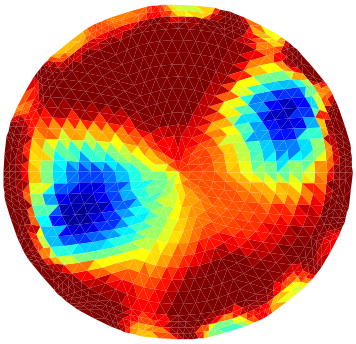

After the initial test, it is clear that the fabric sensor is capable of handling single and multiple objects. The image quality is generally better when the object is placed close to the edge where the sensitivity is high. When objects were placed in the middle, the image gets slightly distorted although the object is still visible from the reconstructed image.

6.2.3 Quantitative Pressure Sensing Test

Since the fabric used is sensitive to pressure, we designed a test to show how the sensor reacts to different pressure by applying various weights at single or multiple points ranging from 500g to 2000g. To minimise experimental error, scaled weights of 500g each were used throughout the entire pressure sensing test. Figure 6.5 shows the background measurement data of the fabric sensor.

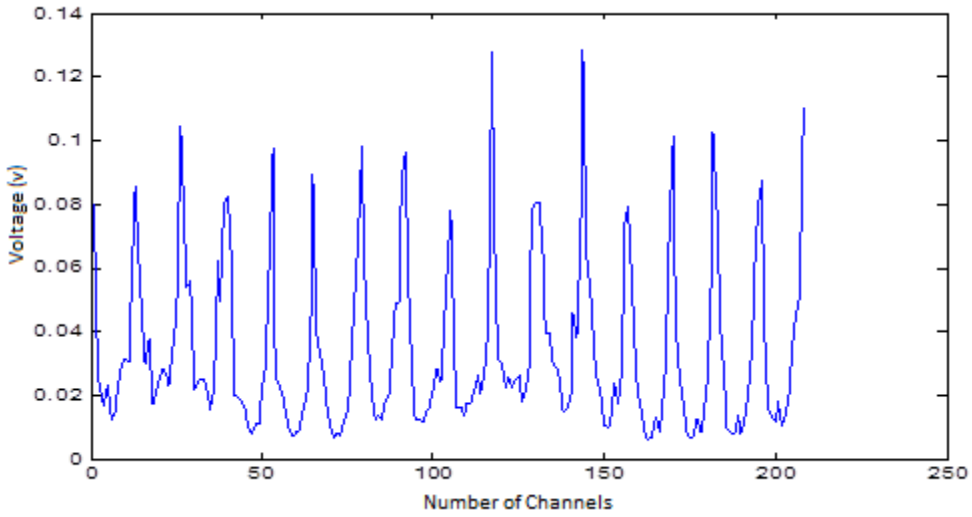

Figure 6.5: Background Measurements for Pressure sensing test

6.2.3.1 Single-Edge Position

The first sets of tests were carried out on the edge of the sensor since EIT generally has a higher sensitivity along the edges.

The testing sequences are:

- Single 500g weight placed on the top right corner of the sensor.
- Two 500g weights (1000g total) placed on the top right corner of the sensor.
- Three 500g weights (1500g total) placed on the top right corner of the sensor.
- Four 500g weights (2000g total) placed on the top right corner of the sensor.

TEST	Reconstructed Image
500g Weight on the edge of the sensor 	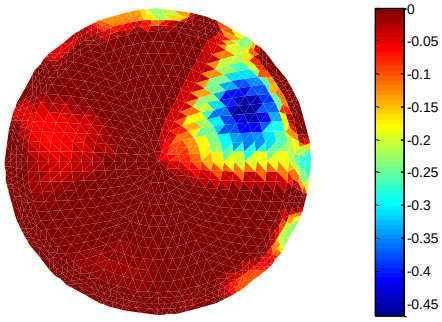
1000g Weight on the edge of the sensor 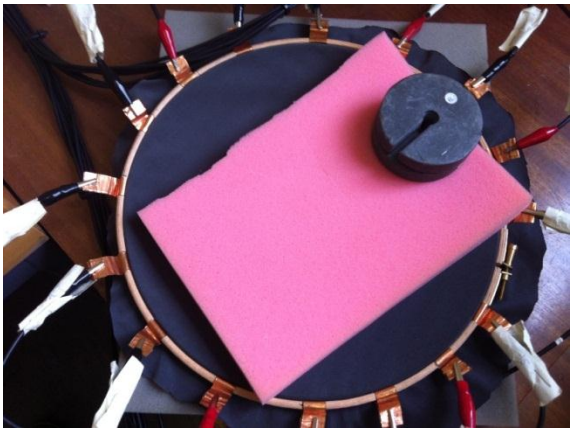	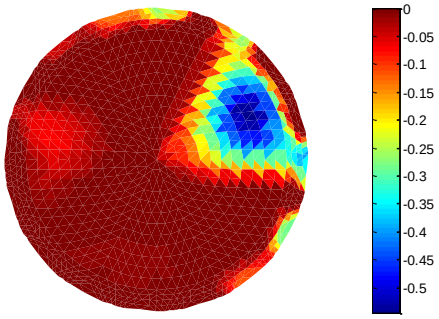
1500g Weight on the edge of the sensor 	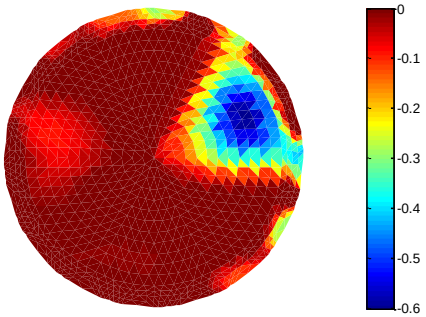

2000g Weight on the edge of the sensor 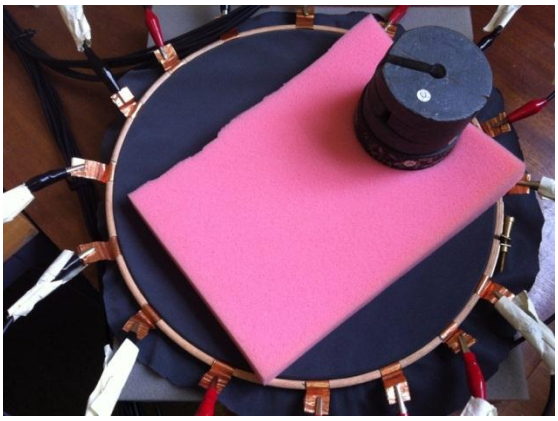	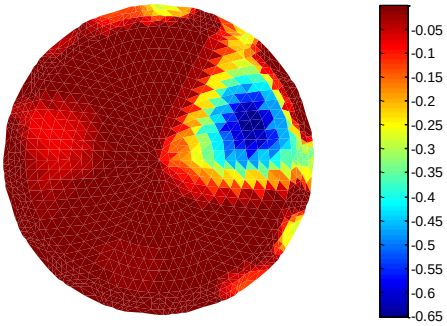

6.2.3.2 Single-Central Position

The second sets of tests were carried out in the middle of the sensor where the sensitivity is at its lowest.

The testing sequences are:

- Two 500g weights (1000g total) placed in the center of the sensor.
- Four 500g weights (2000g total) placed in the center of the sensor.

TEST	Reconstructed Image
1000g Weight in the middle of the sensor 	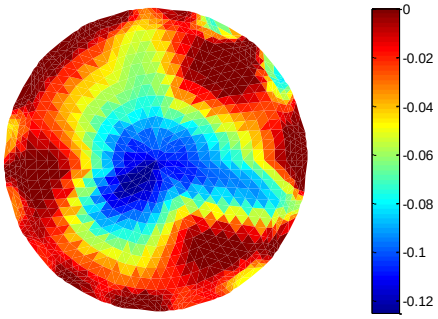

2000g Weight in the middle of the sensor 	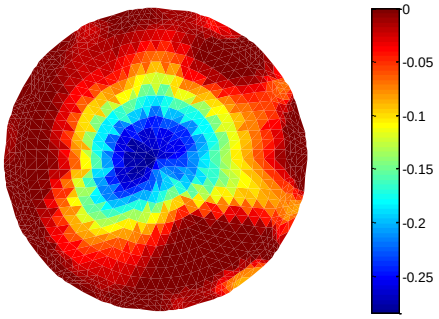

6.2.3.3 Multiple Position

So far all the pressure sensing tests were all at a single location. It would be important to see how the system performs on multiple locations.

The testing sequences are:

- Single 500g weight placed on the top right corner of the sensor.
- Two 500g weights placed at each end of the diagonal line.
- Three 500g weights placed at the top-right, bottom-right and bottom-left corner positions.
- Four 500g weights placed at the top-right, top-left, bottom-right and bottom-left corner positions.
- Four 500g weights placed at the the top-right, top-left, bottom-right, bottom-left corners and three objects stacking together on the center of the sensor.

TEST	Reconstructed Image
500g Weight on the edge of the sensor 	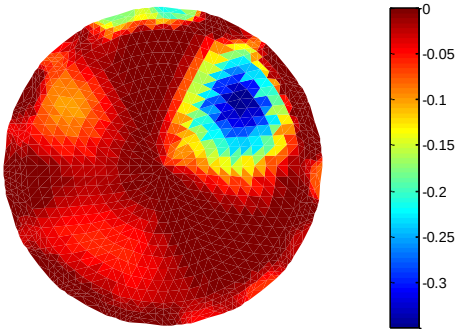
Two 500g Weight placed at both ends of the middle line 	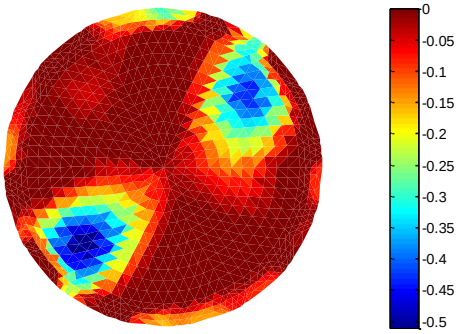
Three 500g Weight placed along the edges of the sensor 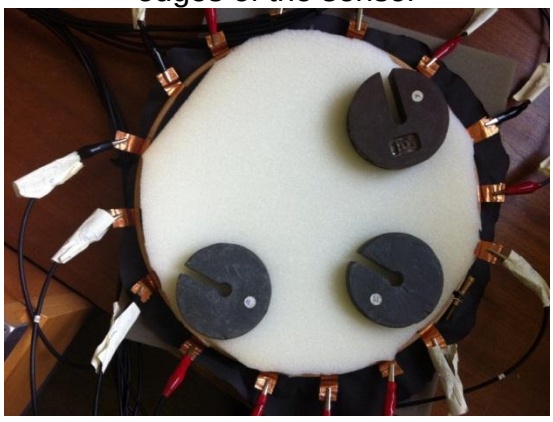	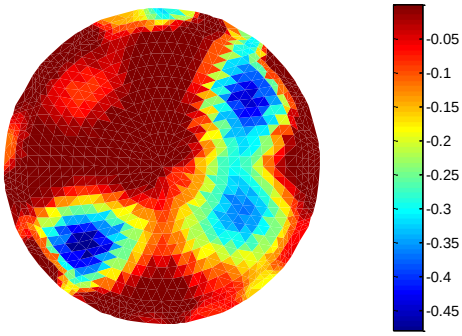

Four 500g Weight placed in the sensor 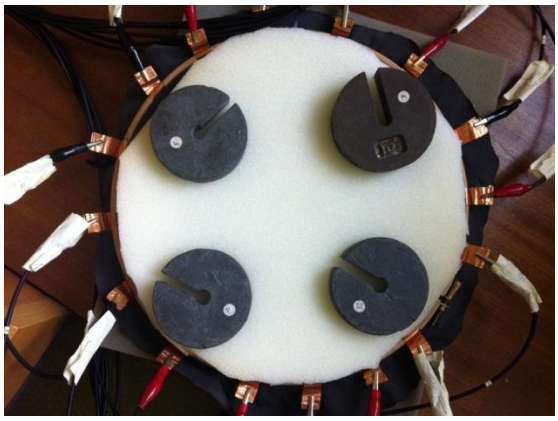	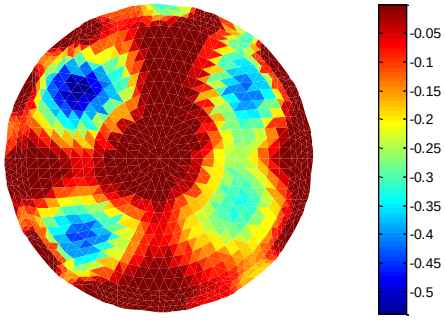
Five objects placed in the sensor 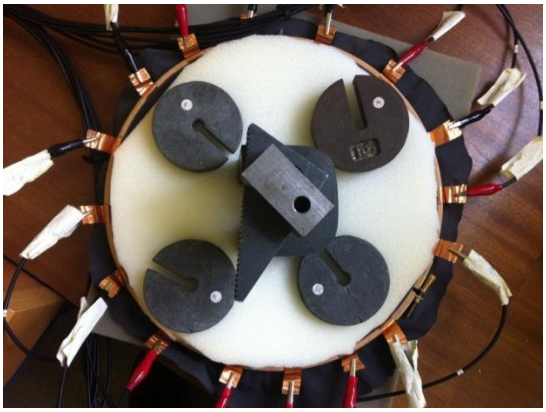	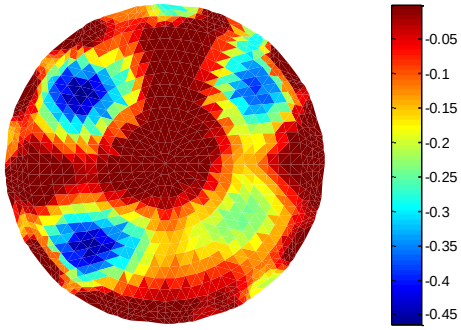

The single-edge and single-central position tests have confirmed the conclusion from the initial tests. Where the sensor is generally more sensitive along the edges, although the middle section is still detectable, the resulting image is less clear when compared to the rest of the area. While the system handles single objects quite well, it also works for multiple objects. In the fabric test, we managed to get a clear reconstructed image for up to four objects. In the five object test, items were placed very close to each other due to the size of the sensor, and the result didn't differ much compared to the four object image. As we managed to get a clear image for five objects in the phantom test but not in the fabric test, we believe this is due to the fact that the distance between those objects is simply too small. The nature of fabric

is different from water saline; since fabric tends to have a network effect, when one point is under pressure the surrounding area would share this pressure. In the five object test, four objects surrounded the middle object and all pressed downward. The middle part of the sensor will share this pressure and, since the fabric's pressure sensitivity is already at its lowest in the middle, the extra pressure applied by the middle object is simply not large enough for the system to see and therefore not detectable. In terms of the quantitative side, by reading from the scale bar on the side of the reconstructed image, it is clear that in the single positioned tests, as the weight increases (500g increment), the maximum reading on the scale bar increases roughly 0.5 each time. Although it is difficult to claim proportionality, other factors should be considered which could affect the final result. For example, the weight can be slightly different for each piece; the positioning can be slightly out, despite the effort of involving the sponge mechanism. In general, the test results had shown promising detectability of the sensor for up to 4 objects.

6.3 Conclusion

In this chapter, the pressure sensitive fabric sensor was tested. The test results had shown promising detectability for single and multiple objects. The sensor also increased the dynamic range of detectability since it no longer requires large deformation when pressure was applied. In quantitative tests, the image scale showed potential quantitative classifications.

Chapter 7

7. Square shaped Fabric Sensor

EIT is generally capable of imaging in various geometries. The sensors can come in all sorts of shapes, the circled shape is always the most commonly used since the distance that current travels between electrodes is always same. To test if the sensor works in different geometry, we decided to build a square shaped sensor. Learning from the previous sensor designs, the surface resistivity of a fabric based sensor needs to be high, which creates a large contrast when pressure is applied. We also extended the 16 channel system to 32 channel system so that larger area imaging could be carried out.

7.1 32 Channel System

The main concept of the 32-channel system is mostly same as the 16-channel system. It has a Multiplexing Circuit, which performs the adjacent switching pattern, and is controlled by the PC-based LabVIEW programme via the Data Acquisition Card.

7.1.1 Multiplexing Circuit

Since we doubled the number of electrodes, the multiplexing circuit had to be redesigned to match this requirement. The new design consisted of two identical

circuits, each with 4 Multiplexing chips (ADG406) and a Hex Inverter (74AC04N). Figure 7.1 shows the PCB layout of one circuit.

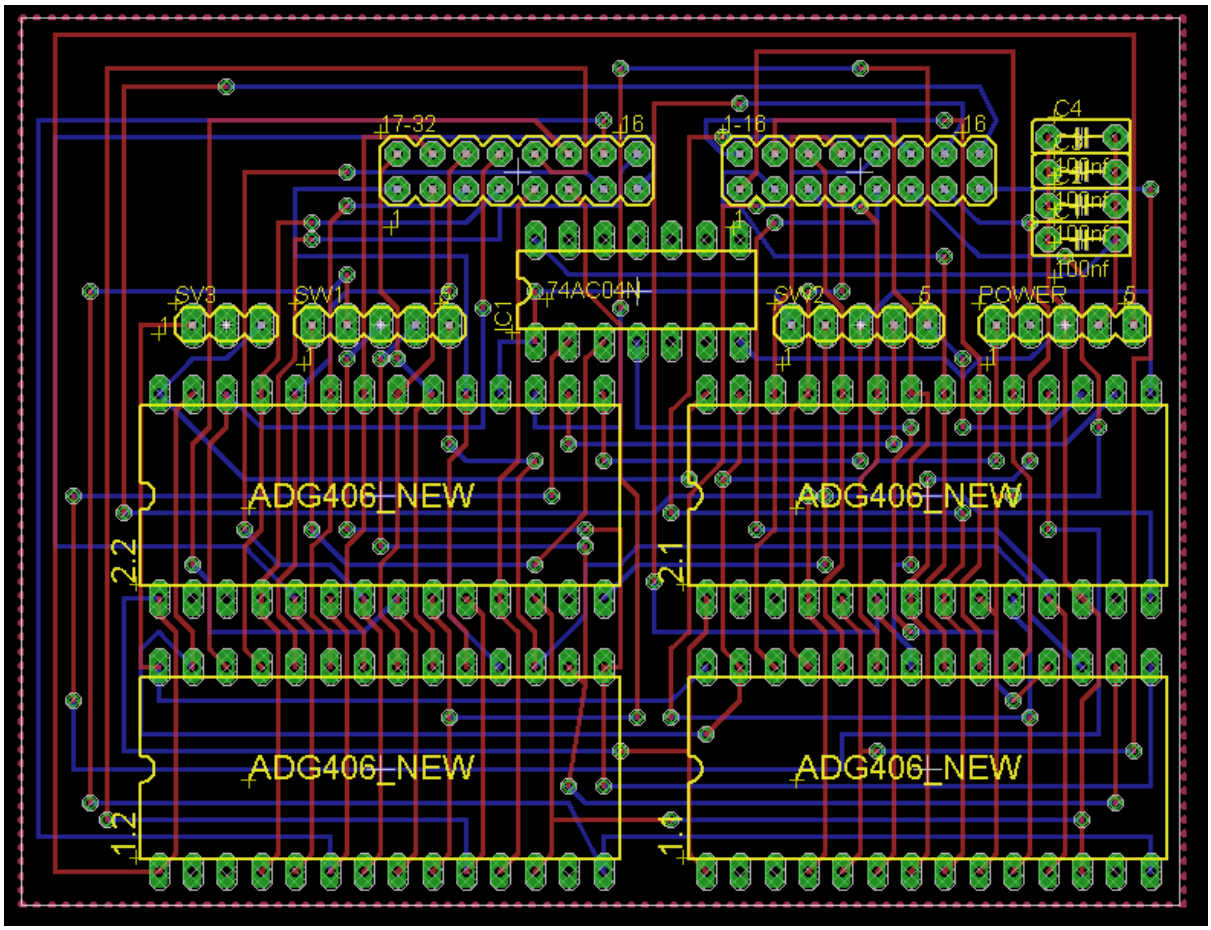

Figure 7.1: 32 channel multiplexer PCB layout

Figures 7.2 and 7.3 show the schematic diagram of the 32-channel Multiplexing circuit.

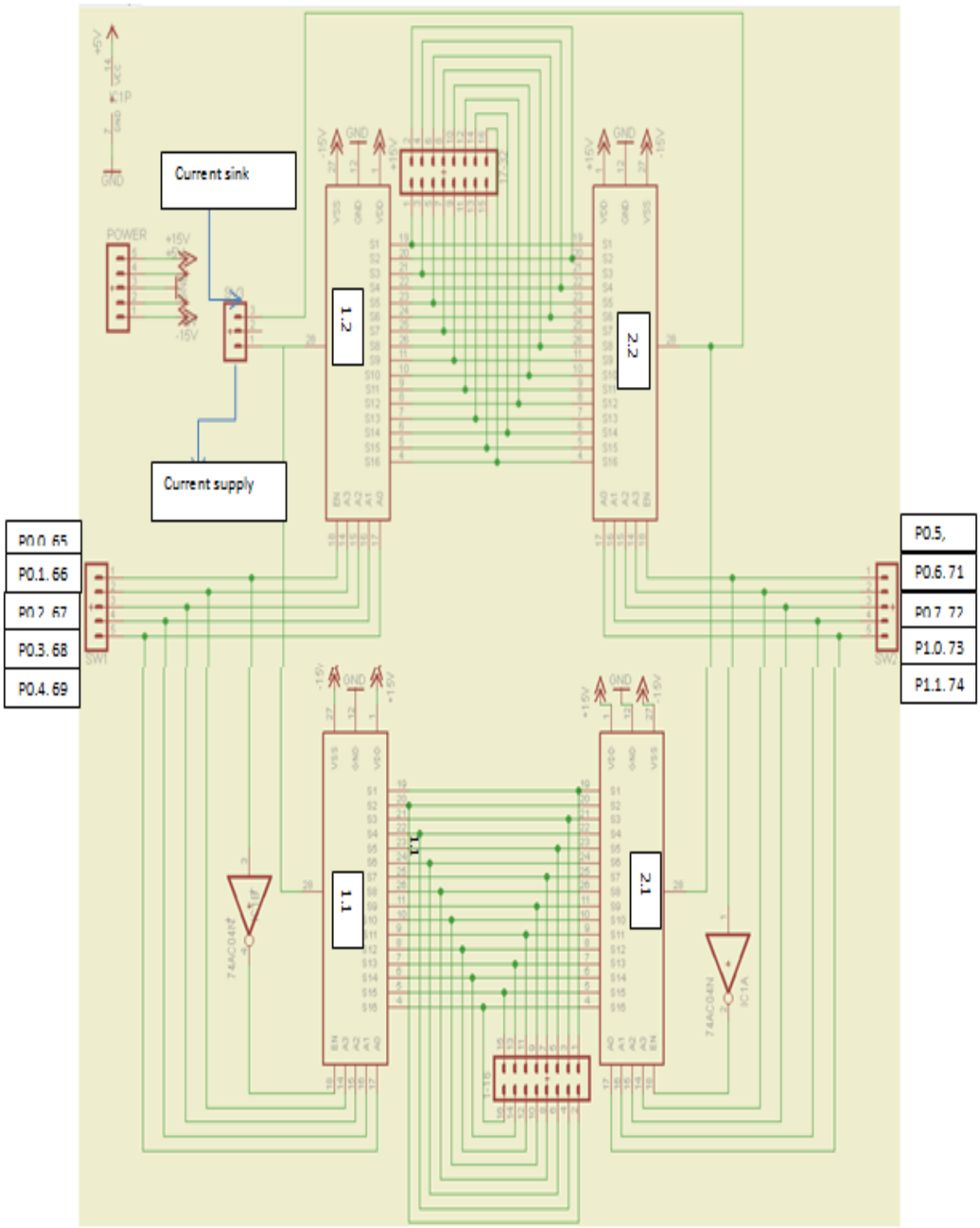

Figure 7.2: 32 channel multiplexer circuit 1

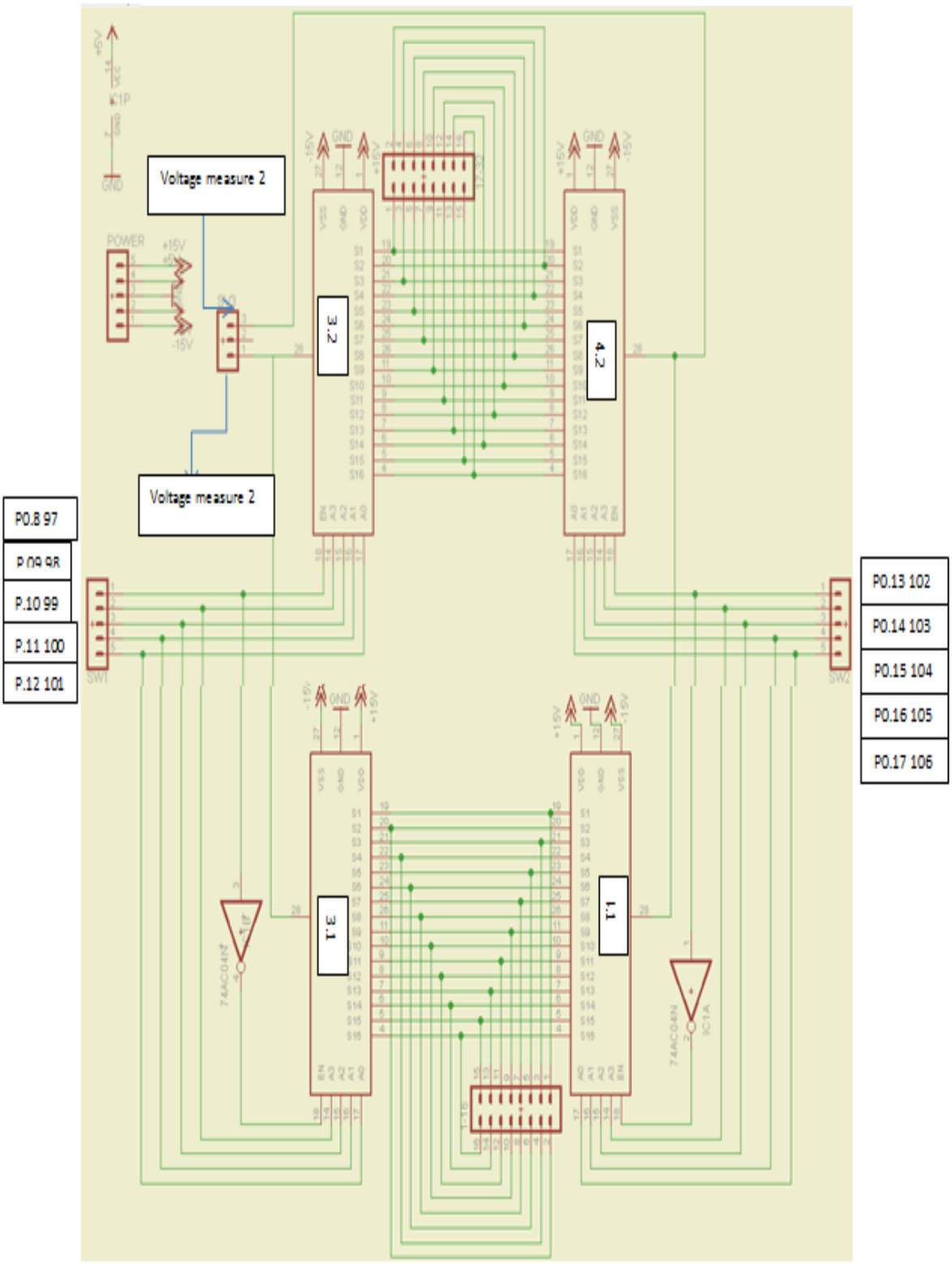

Figure 7.3: 32 channel multiplexer circuit 2

7.2 Square shaped sensor concept

The material used in the square sensor is NW170-SL-PA-1500[109], which is also developed by the Eeonyx Corporation. It is a microfiber nonwoven coated with conductive formulation and, by the description on the product information sheet, it is designed for application with a dynamic pressure sensing requirement. The surface resistivity of this material is 1500Ω per square meter +/-15%. The reduced stretch ability reduces potential hysteresis effect since no large scaled deformation could occur when pressure is applied. As always, the material needs a frame for correct positioning and attaching electrodes, therefore similar concepts have been implemented. Since our sensor is square shaped, the frame naturally comes in squares. Two square wooden plates were used and both of their middle sections were cut out to fit the fabric which creates room for deformation. In terms of size, the squared sensor is doubled to maximise the detectable area. Since the area has been doubled, we have to increase the number of electrodes to compensate for the loss of pixel, so 32 stainless steel strips, identical in size, were cut to form the electrodes. These electrodes were equally spaced in between and 8 were placed on each side of the sensor (Fig 7.4).

Since we have developed a new multiplexer for the system, by adding an extra set of switching pattern/look-up tables in the multiplexing programme (LabVIEW), the system is then capable of running both 16-channel mode and 32-channel mode without changing or removing the attached electrodes.

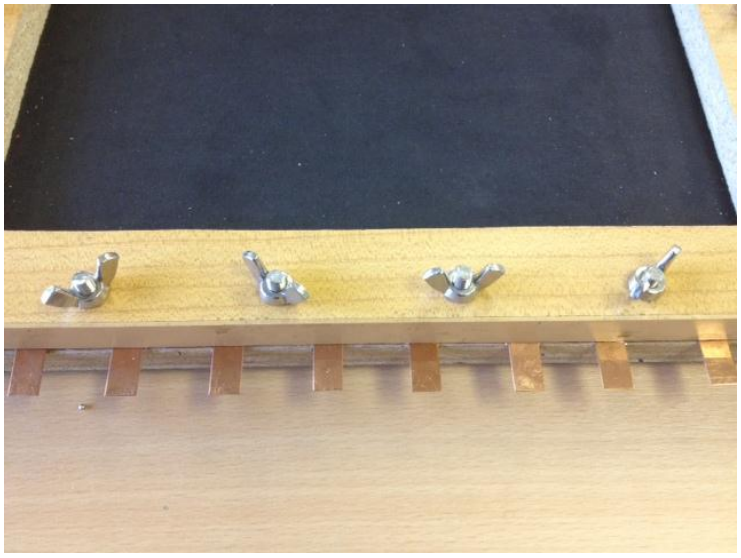

Figure 7.4: Demonstration of 8 electrodes on each side

Figure 7.5 shows the structure of the square sensor.

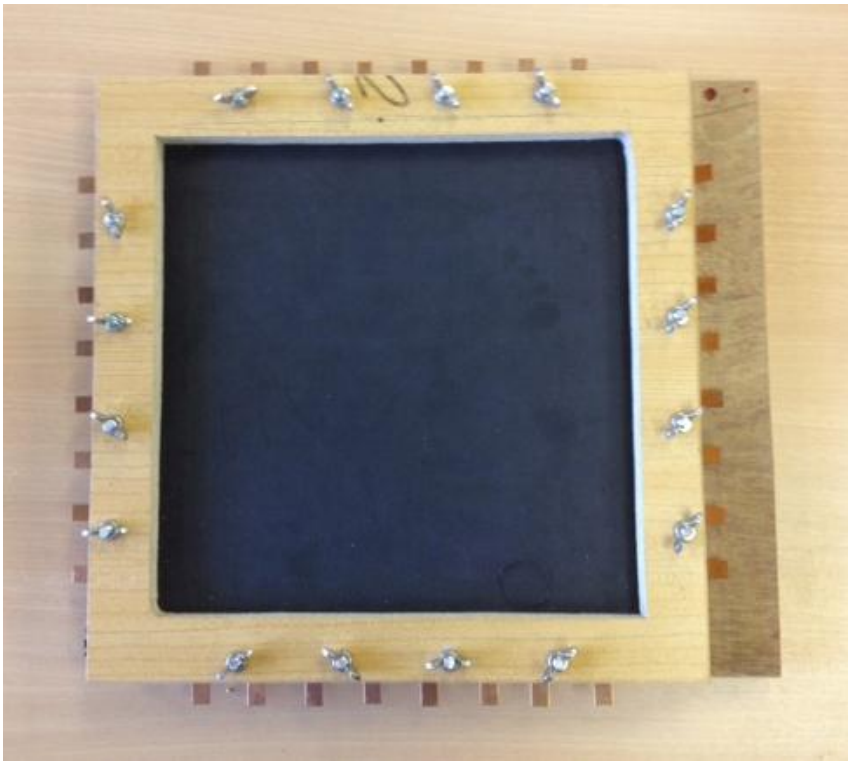

Figure 7.5: Square shaped Fabric Sensor

7.3 Sensor Performance Evaluation

One of the most important parts of the design procedure is the evaluation test where the sensor's performance is put through a series of tests. To maintain the

consistency of the research, it is vital that the squared sensor goes through the same tests.

7.3.1 Signal-to-Noise Ratio Test on 16-channel mode

Mean SNR = 47.5 dB

Peak SNR = 58.3 dB

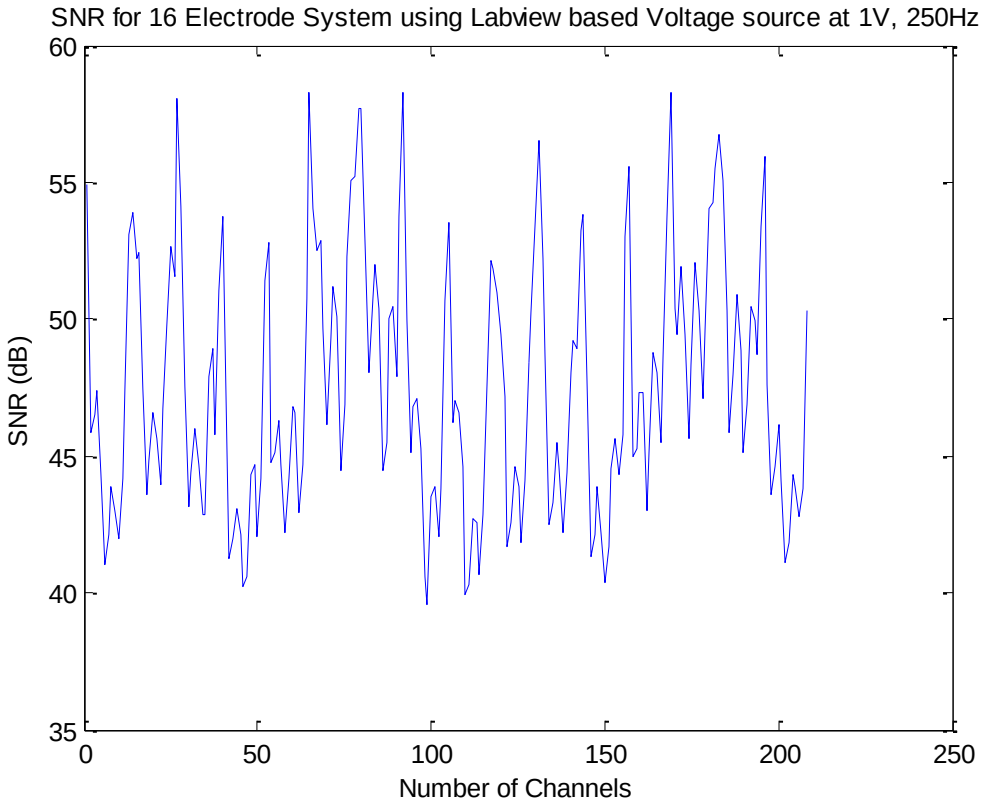

Figure 7.6: SNR for 16 channel mode

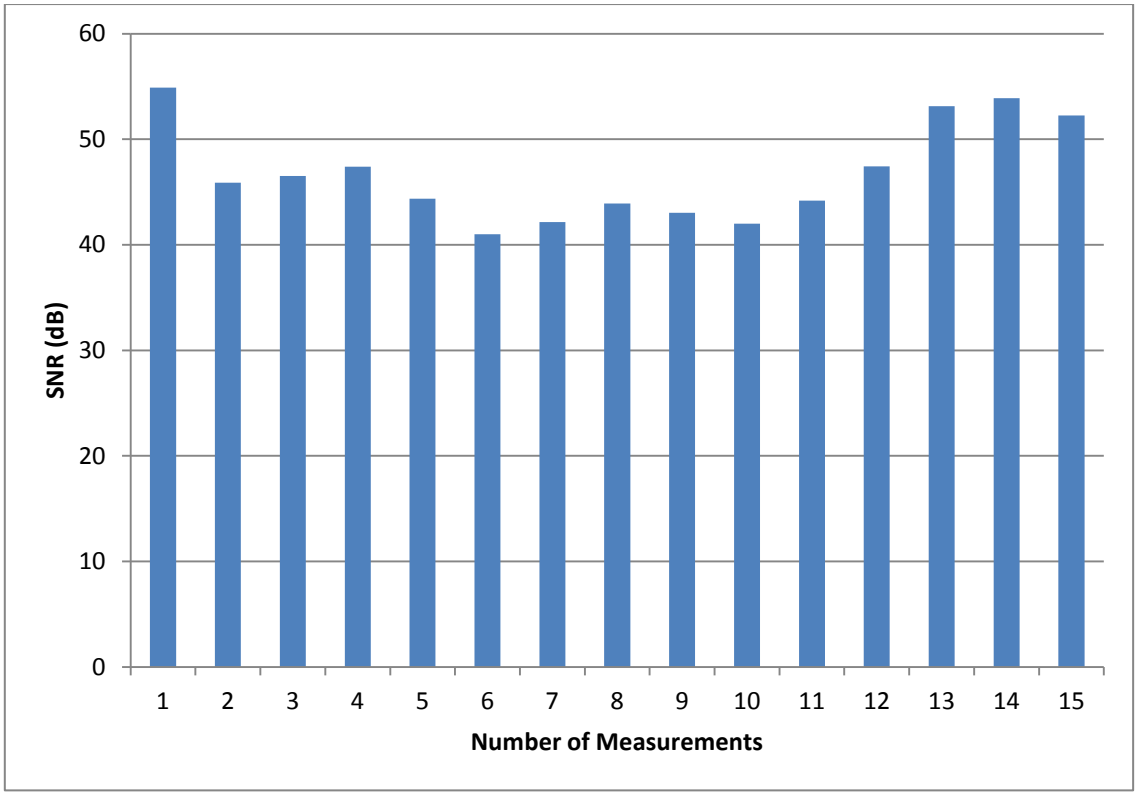

Figure 7.7: SNR trend for the first 15 measurements

7.3.2 Signal-to-Noise Ratio Test on 32-channel mode

Mean SNR = 41.09 dB

Peak SNR = 59.5 dB

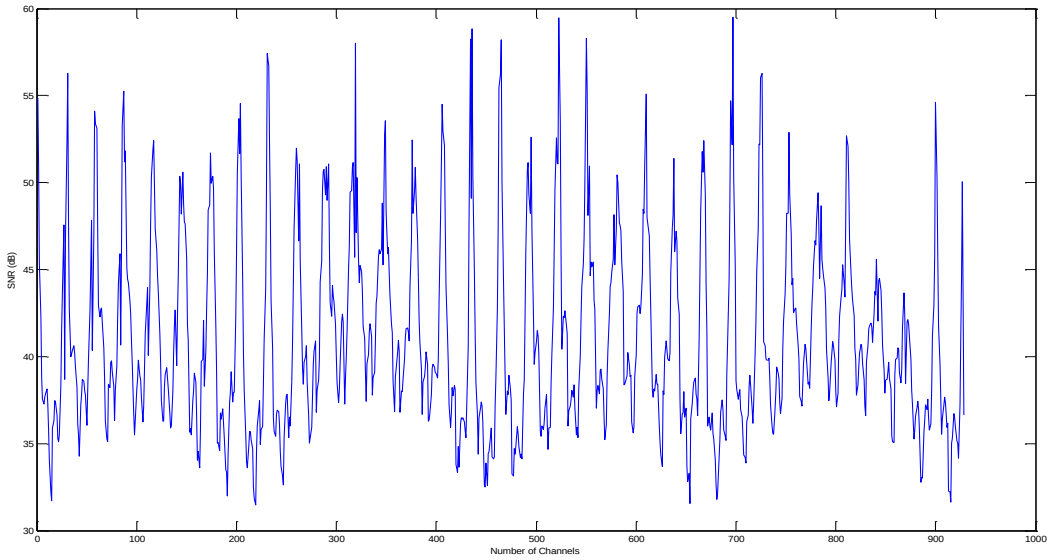

Figure 7.8: SNR for 32 channel mode

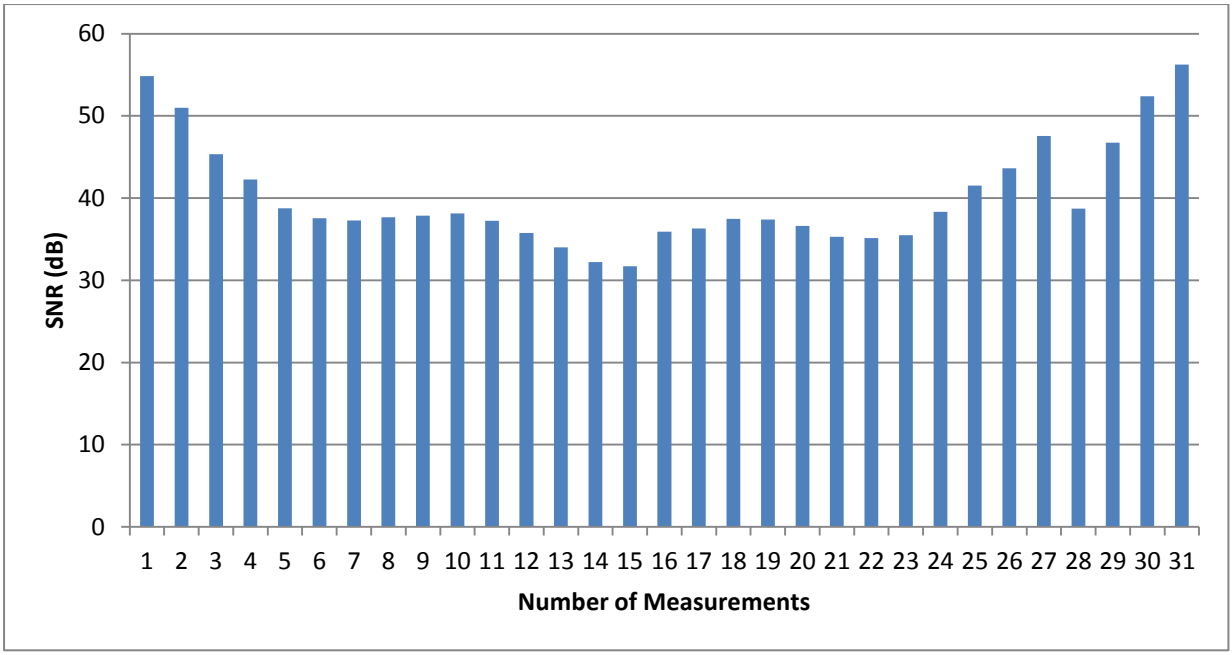

Figure 7.9: SNR trend for the first 32 measurements

7.3.3 Single and Multiple Object Imaging

The test begins by placing one metal object at the lower left corner, then two objects on the upper right and lower corner, and finally three objects on upper left, upper right and lower right corners.

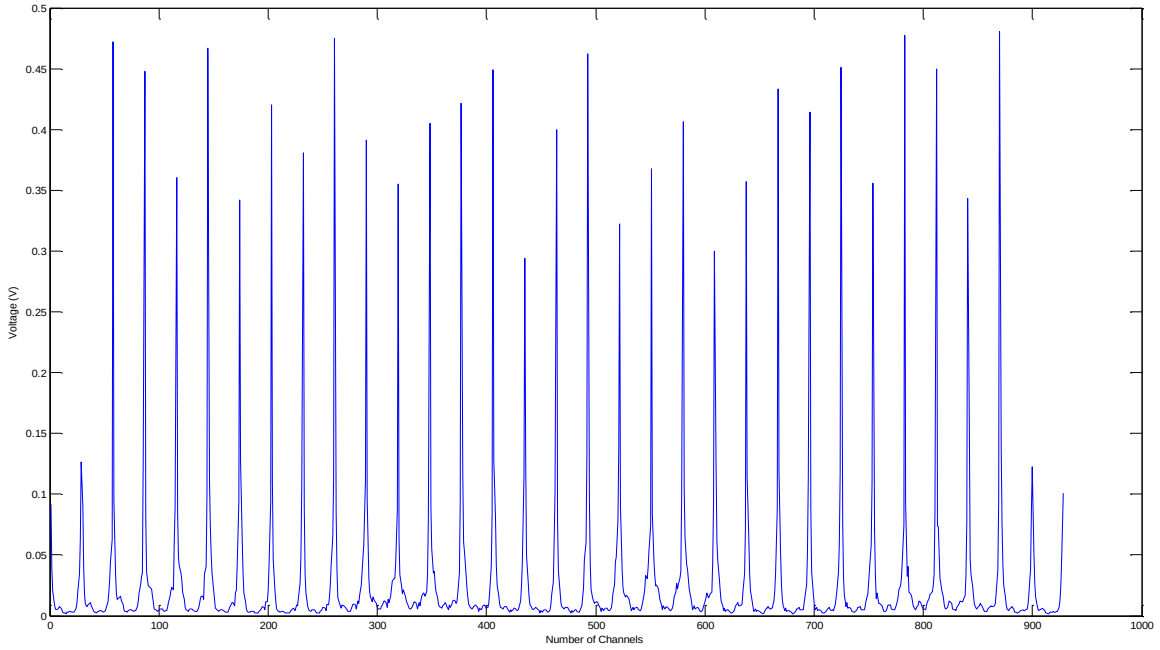

Figure 7.10: Background Measurement of the Square Sensor in 32 electrode mode

TEST	Reconstructed Image
Single Weight on the Square Sensor 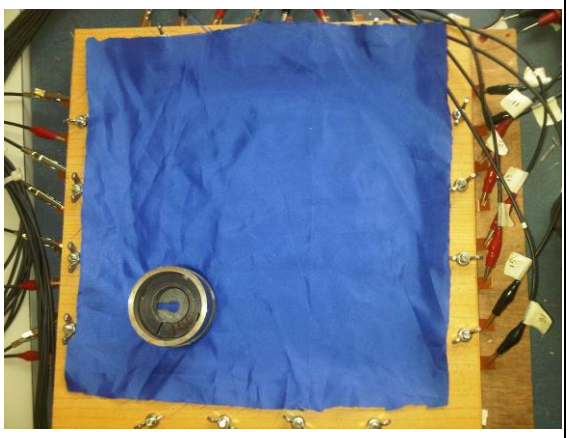	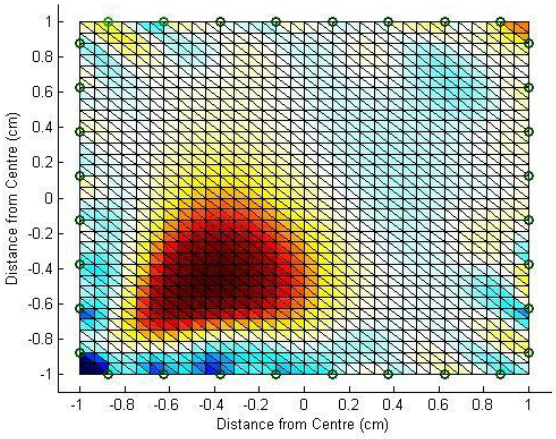
Two Weight on the Square Sensor 	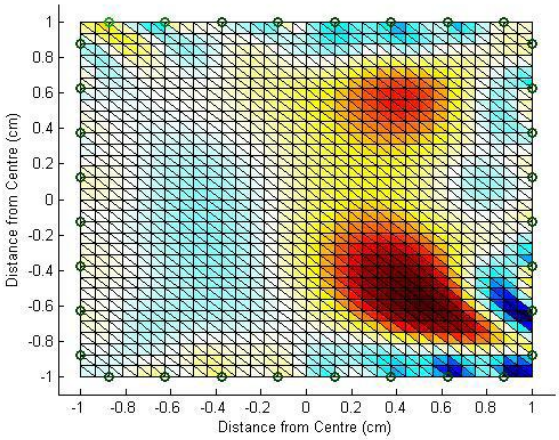
Three Weight on the Square Sensor 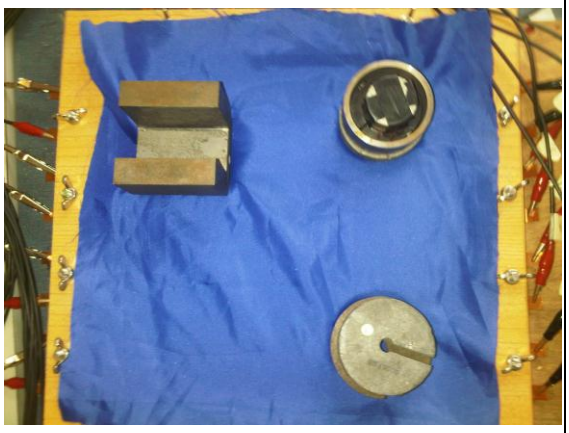	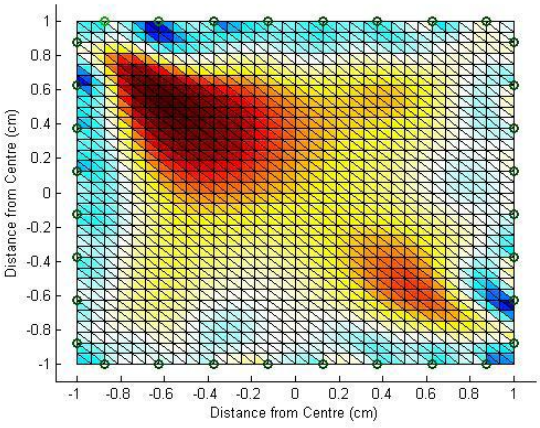

Single Weight in the middle of the Square Sensor	
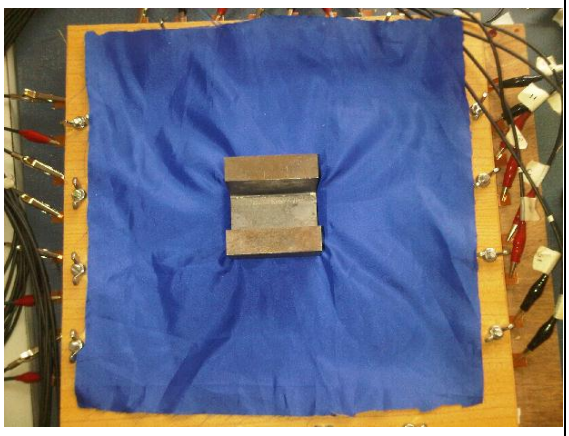	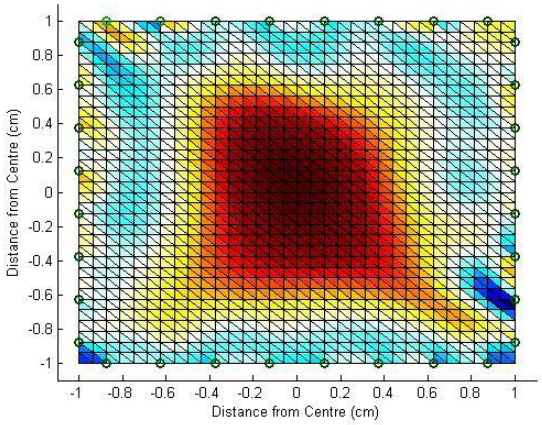

7.3.4 Quantitative Sensing Test

The quantitative test consists of up to three 500g weights at a single location. Here we tested both the center and lower left corner.

TEST	Reconstructed Image
500g Weight in the Center 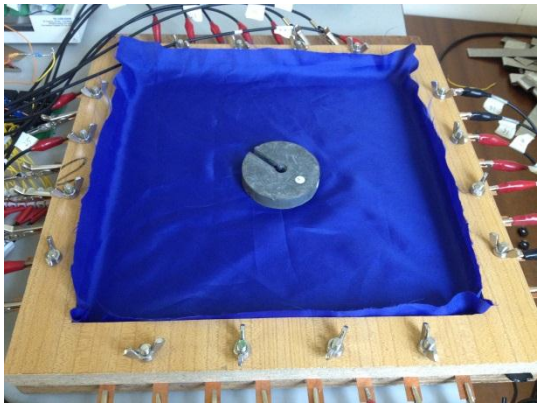	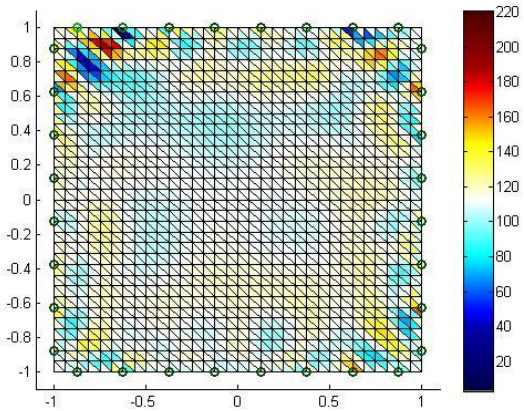

1000g Weight in the Center

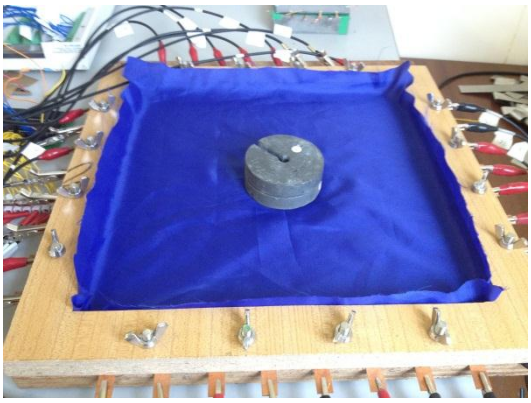

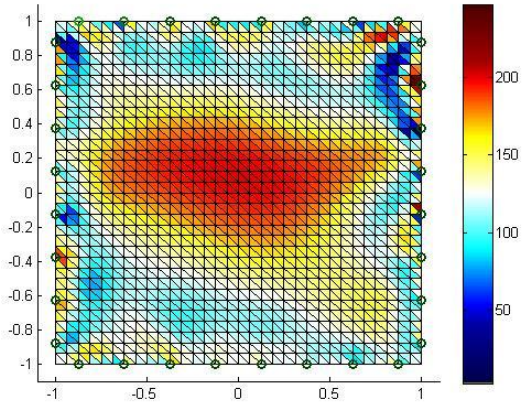

1500g Weight in the Center

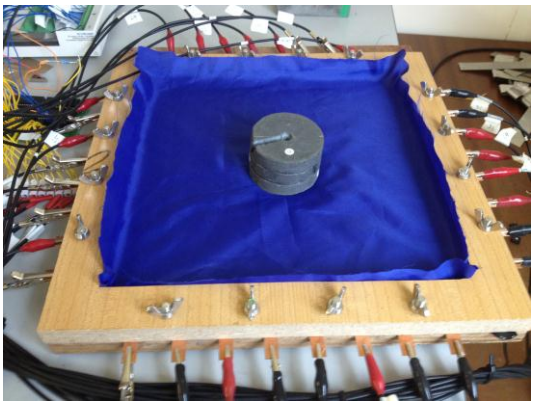

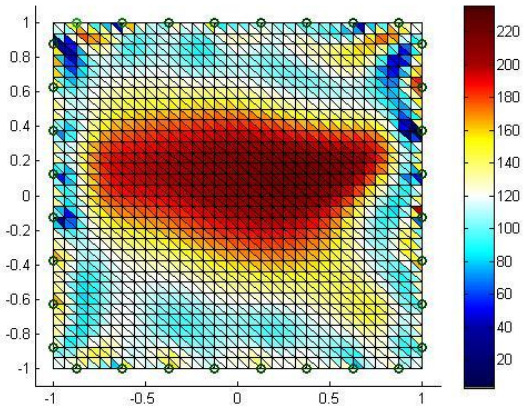

500g Weight in the Lower Left Corner

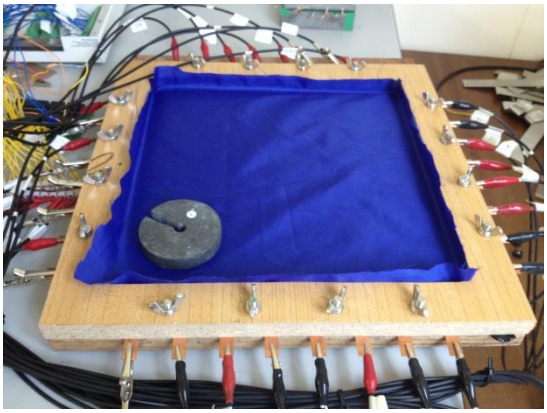

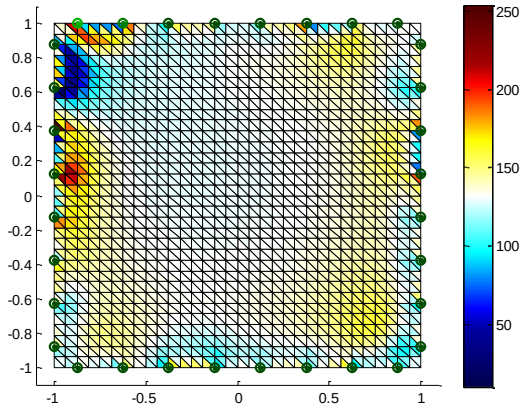

1000g Weight in the Lower Left Corner 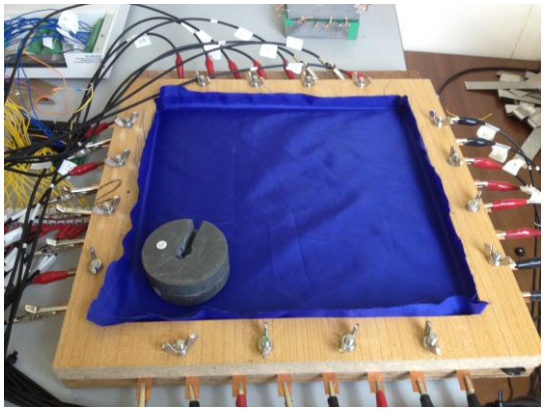	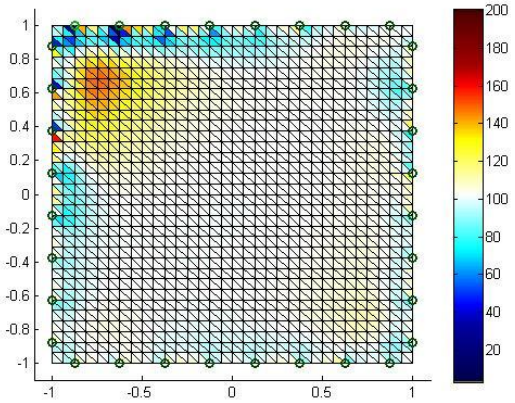
1500g Weight in the Lower Left Corner 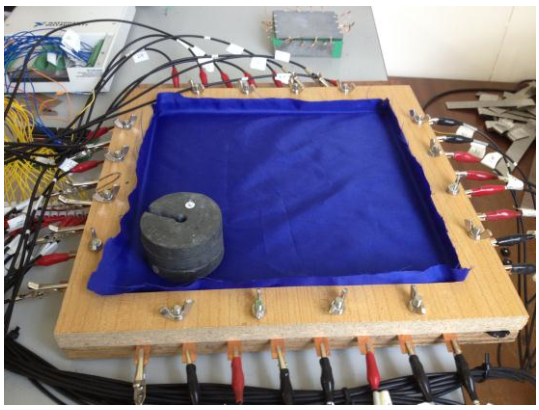	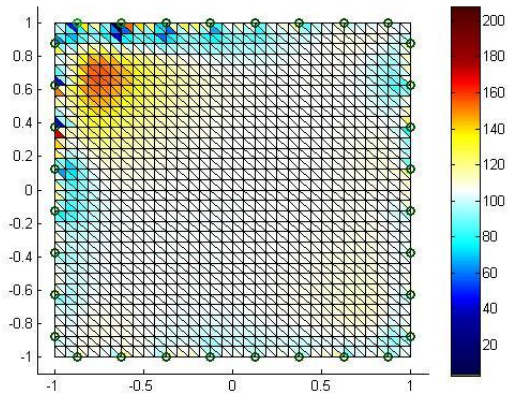

7.3.5 Preliminary Human Application Test

Apart from the quantitative and multi-object imaging test, the ultimate purpose of the system is for human application. Therefore, a young volunteer was invited to aid in the application test. The sensor does not need to be in direct contact with the person so it is entirely safe to test. The results are shown below:

TEST	Reconstructed Image
Single Foot on the Sensor 	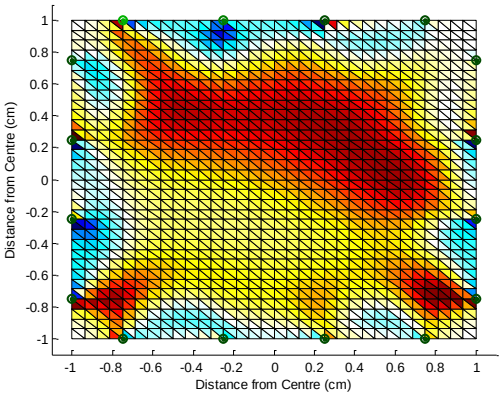
Both Feet on the Sensor 	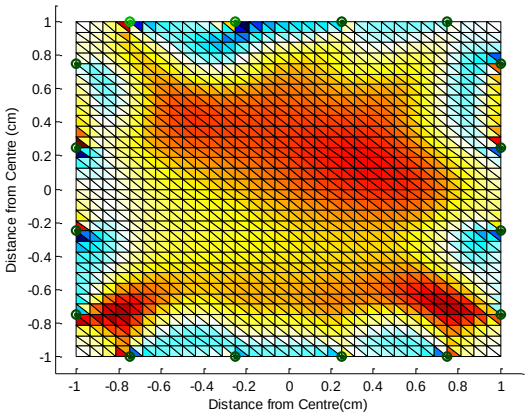

Both feet on the sensor and facing right 	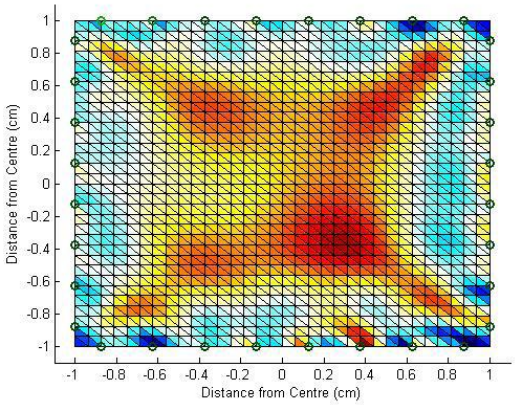

In this chapter, the square shaped fabric sensor was introduced. With the additional hardware improvement, it is capable of performing both 16- and 32-channel measurements. The signal-to-noise ratio tests showed a reasonable SNR at an average of 41dB and 47dB for the 32- and 16- channel modes respectively. In terms of the imaging capability, results from the single and multiple object tests have proved it is more than capable of detecting single and multiple pressure points where localised errors were still affecting the quality of the reconstructed image. This is due to its nature as a fabric, despite our effort of placing thick sponges underneath the fabric as a support to avoid non-localised displacement. The quantitative tests have shown an interesting fact that there is a minimum threshold pressure to actually produce an image with this fabric sensor as the result of a single 500g weight in the middle and corner did not produce any change in the resulting image. It only started to show changes as another 500g weight was added and so on. Once the applied pressure was above the minimum threshold, which we believe is around 750g, the resulting image started to follow a proportional trend as the level of signal starts to

increase as the more pressure was applied. This is shown the colour coded side bar is referred to. The last experiment, which was a human application test that involves a young person's feet, was imaged by the square sensor using 16-channel mode. The tests were performed on single and both feet. As the reader may notice, the top part of the first two images of the single and both feet experiments look almost identical. We believe this is because the young person was putting most of his body weight on to his right foot for balance during both tests. In the second image, where both of the young person's feet were placed, pressure is shown on the lower part of the image as a result from the young person's left foot. The third image was done in 32-channel mode for the purpose of a repeatability test of our imaging system as well as to determine whether a 32-channel mode performs better in this case. The result was considered an improvement since the young person's feet were almost recognisable in the image.

In general, the square shaped fabric sensor showed promising results after it went through the standard testing procedure. With the improved hardware for 32 channels, it opens up a lot of possibilities as it allows us to do more tests using the 32-channel mode.

7.4 Conclusion

In this chapter, the square shaped fabric sensor was tested. The fabric is more pressure sensitive and since we increased the number of electrodes to 32, it allowed us to increase the size of the sensor as well. The change from circular shape to square shape was a testing case for geometrical flexibility of the EIT mapping system. In many applications we may need to use a square shaped sensor. In terms of the performance, this sensor was able to match the circular pressure sensor.

Chapter 8

8. Conclusions and Future Work

Tomography in general is a technique that reconstructs 2D or 3D images of the internal properties from a given subject. The data is measured through a set of sensors surrounding the subject and, based on certain mathematical reconstruction algorithms, the image was produced. Over the years, different types of tomography techniques became available, such as X-ray tomography, γ -ray tomography, computational tomography (CT), ultrasound B – scan, magnetic resonance imaging, and electrical tomography. In terms of application, tomography techniques are widely used in various fields, including industrial process monitoring, geophysical probing, non-invasive testing and medical diagnostic imaging. Recent developments have also shown potential applications for pressure monitoring in clinical care. In this thesis, the main research focus is on one of the tomography techniques called electrical impedance tomography (EIT). EIT is a member of the electrical tomography family. It is a relatively new and emerging tomography technique, which utilises electro impedance principles. In this thesis, an in-depth study of EIT techniques has been carried out, focusing on developing the required hardware and software for pressure monitoring applications.

8.1 Conclusion

Over the period of this PhD study, two different models of 2D EIT systems (16-channel system and 32-channel system) have been developed and discussed, where three different types of fabric sensors have also been developed and tested, namely the circular shaped deformation sensitive fabric sensor, the circular shaped pressure sensitive fabric sensor and the square shaped fabric sensor (also sensitive to pressure). The system development process was discussed in detail in Chapter 2 and Chapter 3, including the reconstruction software development and the multiplexing circuit design, as well as the selection of the data acquisition card from National Instruments (NI). The 16-channel system that was built originally was later modified to accommodate a 32-channel sensing capability (introduced in the beginning of chapter 7) as the sensor design evolves.

In order to justify the performance of our hardware system, a test phantom was built and a set of tests were performed and discussed in Chapter 4, including the signal-to-noise ratio of both systems. The phantom test results shown in Chapter 4 matches the theory that an increase of excitation voltage or current would result in an increase of the measured voltage and hence a stronger detectability of testing objects. Although the image quality can be improved by increasing the excitation current/voltage, it is limited by the maximum current supply capability of our Data Acquisition Card, which is 5mA. As shown in the results, excitation voltage/current has an influence on the detectability of objects as their number increases in the phantom. In general, all phantom test results were very similar but the LabVIEW based voltage source was limited to the maximum current supply of 5mA, therefore,

in order to operate at higher currents, it is essential to use a current source circuit and so it was developed later.

All three sensors that were developed went through the same standard testing procedure as illustrated in Chapters 5, 6 and 7. The results showed improvement as more experience was gained in both sensor building techniques and reconstruction software development. The images produced by our deformation sensitive sensor demonstrate the feasibility of the EIT system for pressure and deformation mapping imaging. In particular, the results showing reconstruction of multiple pressure points were very promising. The results also suggested that quantisation of the pressure profile may be possible, but it was still very challenging. By taking the experiences from the first sensor, we went in a different direction in terms of material selection when the pressure sensitive sensors were developed.

The circular shaped pressure sensor showed improved image quality as less hysteresis effect was found. The reason for this being, in order for the pressure sensitive material to detect pressure, large scaled deformation was not required.

Other studies suggest that an increase in electrode numbers at the boundary would enhance the system's overall performance; hence a 32-channel concept was formed and implemented into the square shaped pressure sensor. The square shaped pressure sensor was developed using a different pressure sensitive material where the stretch ability was limited. In general, the square shaped fabric sensor showed promising results after it went through the standard testing procedure, as the average signal-to-noise ratio had increased to almost 10dB compared to the circular shaped pressure sensor. With the improved hardware for 32-channel mode, the system produces even better results as shown in the human application test section.

8.2 Future Work

This thesis has explored the fundamental principles of EIT while achieving several improvements with regard to EIT pressure sensing techniques. Based on these findings, many interesting new research projects could be initiated.

- Complex conductivity imaging Multi-frequency imaging: So far, the project has focused on developing a pressure monitoring system based on a single–frequency difference imaging EIT system. Since the modal structure of the fabric-based sensor is not entirely pure resistance, measurement of permittivity can be useful, particularly for capacitive effect in the contact nodes, and the change due to the deformation of the structure can provide valuable information.

  By applying current or voltage at continuously selectable driving frequencies of up to 100 KHz (limited by the digital Analogue Converter), the driving current patterns need to be simultaneously supplied to each electrode, while taking voltage measurements at those electrodes simultaneously.

  So far, our group and others considered the resistivity component of complex conductivity in a single-frequency aspect. This opens up the opportunity for multiple-frequency imaging of the fabric-based EIT, as well as complex conductivity imaging since complex conductivity will provide information on the capacitive component of the electrical impedance.
- Nonlinear image reconstruction: Difference imaging has the advantage of being more reliable. In a difference imaging mode, two sets of measurements are used and subtracted, which will reduce the impact of systematic error in the system, and that is why we have been relying on this technique

throughout our research. However, in many practical applications it is sometimes impossible to obtain a reference condition beforehand, which is often the case in medical applications. Therefore, a more challenging imaging for a fabric-based system is absolute image reconstruction.

Absolute image reconstruction requires a nonlinear inversion algorithm. If it can be implemented, this will greatly enhance the application of a wearable EIT and brings a number of new applications. This means that the system can measure any shape without the need for a reference shape.

The tasks above are suggestions for future EIT research.

In summary, EIT's low cost and non-invasiveness offers great excitement and potential for many challenging problems that currently exist in both industrial and medical applications. This thesis proposed a new application for the EIT imaging and we have demonstrated in laboratory prototype the work of these sensors. For any future application, many more factors are needed to be considered, but the prototype results are showing great deal of promise.

Appendix A

Multiplexing sequence table – Adjacent current pattern:

Mux1	Mux 2	Mux 3	Mux4	Excitation, measurement
0000	0001	0010	0011	1 - 2 , 3 – 4
		0011	0100	4 – 5
		0100	0101	5 – 6
		0101	0110	6 – 7
		0110	0111	7 – 8
		0111	1000	8 – 9
		1000	1001	9 – 10
		1001	1010	10 – 11
		1010	1011	11 – 12
		1011	1100	12 – 13
		1100	1101	13 – 14
		1101	1110	14 – 15
		1110	1111	15 – 16

0001	0010	0011	0100	2 - 3 , 4 – 5
		0100	0101	5 - 6
		-	-	--
		-	-	--
		1110	1111	15 – 16
		1111	0000	16 – 1
0010	0011	0100	0101	3 – 4, 5 – 6
		0101	0110	6 – 7
		-	-	-- ----------
		--	--	----------
		0000	0001	1 – 2
0011	0100			4 – 5
0100	0101			5 – 6
0101	0110			6 – 7
0110	0111			7 – 8
0111	1000			8 – 9
1000	1001			9 – 10

1001	1010			10 – 11
1010	1011			11 – 12
1011	1100			12 – 13
1100	1101			13 – 14
1101	1110			14 – 15,
1110	1111	0000	0001	15 – 16, 1 – 2
		0001	0010	2 – 3

		1100	1101	13 – 14
1111	0000	0001	0010	16 – 1 , 2 – 3
		0010	0011	3 – 4
		0011	0100	4 – 5
		0100	0101	5 – 6
		0101	0110	6 – 7
		0110	0111	7 – 8
		0111	1000	8 – 9
		1000	1001	9 – 10
		1001	1010	10 – 11

		1010	1011	11 – 12
		1011	1100	12 – 13
		1100	1101	13 – 14
		1101	1110	14 – 15

Table 2: Adjacent switching pattern for 16 Electrode 2D systems

Reference

1. Holder, D., *Electrical impedance tomography: methods, history, and applications*2005: Taylor & Francis.
2. Bates, R.H.T., *Overview of computerized tomography with emphasis on future developments.* Proceedings of the IEEE, 1983. **71**(3).
3. Henderson, R.P., *An impedance camera for spatially specific measurements of the thorax.* IEEE transactions on bio-medical engineering, 1978. **bme-25**(3): p. 250.
4. Bates, R.H.T., *A limitation on systems for imaging electrical conductivity distributions.* IEEE transactions on bio-medical engineering, 1980. **bme-27**(7): p. 418.
5. Barber, D.C., *Applied potential tomography.* Journal of physics. E, Scientific instruments, 1984. **17**(9): p. 723.
6. Brown, B.H., *The Sheffield data collection system.* Clinical physics and physiological measurement, 1987. **8**(4a): p. 91.
7. Goharian, M., *A DSP Based Multi-Frequency 3D Electrical Impedance Tomography System.* Annals of biomedical engineering, 2008. **36**(9): p. 1594.
8. Holder, D., *Imaging of the torax by EIT*, in *Electrical impedance tomography: methods, history, and applications*2005, Taylor & Francis. p. 109-110.
9. Hahn, G., F. Thiel, T. Dudykevych, I. Frerichs, E. Gersing, T. Schrder, C. Hartung, and G. Hellige, *Quantitative evaluation of the performance of different electrical tomography devices.* Biomedizinische Technik/Biomedical Engineering, 2001. **46**(4): p. 91-95.
10. Isaacson, D. and P. Edic. *An Algorithm for Impedance Imaging*. in *Engineering in Medicine and Biology Society, 1992. Vol.14. Proceedings of the Annual International Conference of the IEEE*. 1992.
11. Knight, R.A., *The use fo EIT techniques to measure interface pressure*, in *Department of Electronic Electrical Engineering*1991, University of Bath: Bath.
12. Muehllehner, G. and J.S. Karp, *Positron emission tomography.* Physics in Medicine and Biology, 2006. **51**(13): p. R117.
13. *Proc. of 1st European concerted Action on Process Tomography (ECAPT) Workshop*. 1992. Manchester, UK.
14. *Proc. of 2nd European concerted Action on Process Tomography (ECAPT) Workshop*. 1993. Karlsruhe, Germany.
15. *Proc. of 3rd European concerted Action on Process Tomography (ECAPT) Workshop*. 1994. Oporto, Portugal.
16. *Proc. of 4th European concerted Action on Process Tomography (ECAPT) Workshop*. 1995. Bergen, Norway.
17. Dickin, F. and M. Wang, *Electrical resistance tomography for process applications.* Measurement Science and Technology, 1996. **7**(3): p. 247.
18. Alessandrini, G. and L. Rondi, *Stable determination of a crack in a planar inhomogeneous conductor.* SIAM J. Math. Anal., 1999. **30**(2): p. 326-340.
19. Polydorides, N. and W.R.B. Lionheart, *A Matlab toolkit for three-dimensional electrical impedance tomography: a contribution to the Electrical Impedance and Diffuse Optical Reconstruction Software project.* Measurement Science and Technology, 2002. **13**(12): p. 1871.

20. Loke, M., *Electrical imaging surveys for environmental and engineering studies-A practical guide to 2D and 3D surveys*, 2000, Universitiy Sains Malaysia Penang, Malaysia.
21. Blumrosen, G., B. Rubinsky, and C.A. Gonzalez. *New Wearable Body Sensor for Continuous Diagnosis of Internal Tissue Bleeding*. in *Wearable and Implantable Body Sensor Networks, 2009. BSN 2009. Sixth International Workshop on*. 2009.
22. Eyuboglu, B.M., B.H. Brown, and D.C. Barber, *In vivo imaging of cardiac related impedance changes.* Engineering in Medicine and Biology Magazine, IEEE, 1989. **8**(1): p. 39-45.
23. Frerichs, I., G. Hahn, and G. Hellige, *Thoracic electrical impedance tomographic measurements during volume controlled ventilation-effects of tidal volume and positive end-expiratory pressure.* Medical Imaging, IEEE Transactions on, 1999. **18**(9): p. 764-773.
24. Gibson, A., R.H. Bayford, and D.S. Holder, *Two-dimensional finite element modelling of the neonatal head.* Physiological Measurement, 2000. **21**(1): p. 45.
25. Harris, N.D., B.H. Brown, and D.C. Barber. *Continuous monitoring of lung ventilation with electrical impedance tomography*. in *Engineering in Medicine and Biology Society, 1992 14th Annual International Conference of the IEEE*. 1992.
26. Holder, D.S., *Electrical impedance tomography (EIT) of brain function.* Brain Topography, 1992. **5**(2): p. 87-93.
27. Kerrouche, N., C.N. McLeod, and W.R. Lionheart, *Time series of EIT chest images using singular value decomposition and Fourier transform*. Vol. 22. 2001. 147-57.
28. Kunst, P.W.A., A.V. Noordegraaf, O.S. Hoekstra, P.E. Postmus, and P.M.J.M.d. Vries, *Ventilation and perfusion imaging by electrical impedance tomography: a comparison with radionuclide scanning.* Physiological Measurement, 1998. **19**(4): p. 481.
29. Smallwood, R.H., Y.F. Mangnall, and A.D. Leathard, *Transport of gastric contents (electric impedance imaging).* Physiological Measurement, 1994. **15**(2A): p. A175.
30. Beck, M.S., *Tomographic techniques for process design and operation*, 1993. p. 490 p.
31. M. Soleimani, C.N.M., R. Banasiak, R. Wajman, , A. Adler, *Four-dimensional electrical capacitance tomography imaging using experimental data.* Progress in Electromagnetics Research-PIER, 2009: p. 171-186.
32. Kourunen, J., R. Käyhkö, J. Matula, J. Käyhkö, M. Vauhkonen, and L.M. Heikkinen, *Imaging of mixing of two miscible liquids using electrical impedance tomography and linear impedance sensor.* Flow Measurement and Instrumentation, 2008. **19**(6): p. 391-396.
33. Razzak, S.A., S. Barghi, J.X. Zhu, and Y. Mi, *Phase holdup measurement in a gas–liquid–solid circulating fluidized bed (GLSCFB) riser using electrical resistance tomography and optical fibre probe.* Chemical Engineering Journal, 2009. **147**(2–3): p. 210-218.
34. Tapp, H.S., A.J. Peyton, E.K. Kemsley, and R.H. Wilson, *Chemical engineering applications of electrical process tomography.* Sensors and Actuators B: Chemical, 2003. **92**(1–2): p. 17-24.
35. J.A. Olowofela, O.D.A.a.A.S.O., *Application of Electrical Impedance Tomography (EIT) in the Investigation of the Impact of Solid Waste Leachate Contaminant Plumes on Groundwater.* Academia Arena, 2012. **4**(6): p. 37-47.
36. Schwan, H.P. *Electrical properties of tissues and cell suspensions: mechanisms and models*. in *Engineering in Medicine and Biology Society, 1994. Engineering Advances: New Opportunities for Biomedical Engineers. Proceedings of the 16th Annual International Conference of the IEEE*. 1994.
37. Stoy, R.D., K.R. Foster, and H.P. Schwan, *Dielectric properties of mammalian tissues from 0.1 to 100 MHz; a summary of recent data.* Physics in Medicine and Biology, 1982. **27**(4): p. 501.
38. Kyriacou, G.A., P.M. Bonovas, C.S. Koukourlis, and J.N. Sahalos. *A step-by-step development of an electrical impedance tomography system*. in *Applied Electromagnetism, 2000. Proceedings of the Second International Symposium of Trans Black Sea Region on*. 2000.
39. Jossinet, J., *Variability of impedivity in normal and pathological breast tissue.* Medical and Biological Engineering and Computing, 1996. **34**(5): p. 346-350.

40. Surowiec, A.J., S.S. Stuchly, J.R. Barr, and A. Swarup, *Dielectric properties of breast carcinoma and the surrounding tissues.* Biomedical Engineering, IEEE Transactions on, 1988. **35**(4): p. 257-263.
41. SHARPLES, T.S.E.N.A., *Dielectric properties of the human body in the microwave region of the spectrum.* Nature, 1949(163): p. 487-488.
42. LAWN, J.R.M.D.G., *Dielectric absorption of microwaves in human tissues.* Nature, 1968(218): p. 366-367.
43. Singh, B., C. Smith, and R. Hughes, *In vivo dielectric spectrometer.* Medical and Biological Engineering and Computing, 1979. **17**(1): p. 45-60.
44. Chaudhary SS, M.R., Swarup A, Thomas JM., *Dielectric properties of normal & malignant human breast tissues at radiowave & microwave frequencies.* Indian J Biochem Biophys, 1984(21): p. 76-79.
45. Kinouchi, Y., T. Iritani, T. Morimoto, and S. Ohyama, *Fast in vivo measurements of local tissue impedances using needle electrodes.* Medical and Biological Engineering and Computing, 1997. **35**(5): p. 486-492.
46. Morimoto T, K.S., Konishi Y, Komaki K, Uyama T, Monden Y, Kinouchi Y, Iritani T, *A study of the electrical bio-impedance of tumors.* J Invest Surg, 1993(6): p. 25-32.
47. Kimura, S., T. Morimoto, T. Uyama, Y. Monden, Y. Kinouchi, and T. Iritani, *Application of electrical impedance analysis for diagnosis of a pulmonary mass.* CHEST Journal, 1994. **105**(6): p. 1679-1682.
48. Konishi, Y., T. Morimoto, Y. Kinouchi, T. Iritani, and Y. Monden, *Electrical properties of extracted rat liver tissue.* Research in Experimental Medicine, 1995. **195**(1): p. 183-192.
49. Denai, M.A., M. Mahfouf, S. Mohamad-Samuri, G. Panoutsos, B.H. Brown, and G.H. Mills, *Absolute Electrical Impedance Tomography (aEIT) Guided Ventilation Therapy in Critical Care Patients: Simulations and Future Trends.* Information Technology in Biomedicine, IEEE Transactions on, 2010. **14**(3): p. 641-649.
50. Soleimani, M., C. Gómez-Laberge, and A. Adler, *Imaging of conductivity changes and electrode movement in EIT.* Physiological Measurement, 2006. **27**(5): p. S103.
51. Zhao, Z., *A lung area estimation method for analysis of ventilation inhomogeneity based on electrical impedance tomography.* Journal of X-ray science and technology. **18**(2): p. 171.
52. Barber, D.C., *A review of image reconstruction techniques for electrical impedance tomography.* Medical physics, 1989. **16**(2): p. 162.
53. Wijesiriwardana, R., K. Mitcham, W. Hurley, and T. Dias, *Capacitive fiber-meshed transducers for touch and proximity-sensing applications.* Sensors Journal, IEEE, 2005. **5**(5): p. 989-994.
54. Ueno, A., Y. Akabane, T. Kato, H. Hoshino, S. Kataoka, and Y. Ishiyama, *Capacitive Sensing of Electrocardiographic Potential Through Cloth From the Dorsal Surface of the Body in a Supine Position: A Preliminary Study.* Biomedical Engineering, IEEE Transactions on, 2007. **54**(4): p. 759-766.
55. Doll, J.C., S.-J. Park, and B.L. Pruitt, *Design optimization of piezoresistive cantilevers for force sensing in air and water.* Journal of Applied Physics, 2009. **106**(6): p. 064310-064310-12.
56. Gharib, H.H. and W.A. Moussa, *On the Feasibility of a New Approach for Developing a Piezoresistive 3D Stress Sensing Rosette.* Sensors Journal, IEEE, 2011. **11**(9): p. 1861-1871.
57. Feneberg, M., K. Thonke, T. Wunderer, F. Lipski, and F. Scholz, *Piezoelectric polarization of semipolar and polar GaInN quantum wells grown on strained GaN templates.* Journal of Applied Physics, 2010. **107**(10): p. 103517-103517-6.
58. Willatzen, M., B. Lassen, L.C. Lew Yan Voon, and R.V.N. Melnik, *Dynamic coupling of piezoelectric effects, spontaneous polarization, and strain in lattice-mismatched semiconductor quantum-well heterostructures.* Journal of Applied Physics, 2006. **100**(2): p. 024302-024302-6.

59. Dong-June, C., R. Chun-Taek, K. Soohyun, and K. Yoon Keun. *High sensitivity inductive sensing system for position measurement*. in *Instrumentation and Measurement Technology Conference, 2000. IMTC 2000. Proceedings of the 17th IEEE*. 2000.
60. Drumea, A., P. Svasta, and M. Blejan. *Modelling and simulation of an inductive displacement sensor for mechatronic systems*. in *Electronics Technology (ISSE), 2010 33rd International Spring Seminar on*. 2010.
61. Lebar, A.M., G.F. Harris, J.J. Wertsch, and Z. Hongsheng, *An optoelectric plantar “shear” sensing transducer: design, validation, and preliminary subject tests.* Rehabilitation Engineering, IEEE Transactions on, 1996. **4**(4): p. 310-319.
62. Wen, Y.H., G.Y. Yang, V.J. Bailey, G. Lin, W.C. Tang, and J.H. Keyak. *Mechanically robust micro-fabricated strain gauges for use on bones*. in *Microtechnology in Medicine and Biology, 2005. 3rd IEEE/EMBS Special Topic Conference on*. 2005.
63. Yongdae, K., K. Youngdeok, L. Chulsub, and K. Sejin, *Thin Polysilicon Gauge for Strain Measurement of Structural Elements.* Sensors Journal, IEEE, 2010. **10**(8): p. 1320-1327.
64. Jaichandar, K.S. and E.A.M. Garcia. *Intelli-sense bed patient movement sensing and anti-sweating system for bed sore prevention in a clinical environment*. in *Information, Communications and Signal Processing (ICICS) 2011 8th International Conference on*. 2011.
65. Heinrich, R. *Smartlow-cost weather sensor as an example for `multi-component' sensors*. in *Multisensor Fusion and Integration for Intelligent Systems, 2006 IEEE International Conference on*. 2006.
66. Cho, J.H., M. Kothare, and M.G. Arnold. *Reconfigurable multi-component sensors built from MEMS payloads carried by micro-robots*. in *Sensors Applications Symposium (SAS), 2010 IEEE*. 2010.
67. Yao, A. and M. Soleimani, *A pressure mapping imaging device based on electrical impedance tomography of conductive fabrics.* Sensor Review, 2012. **32**(4): p. 310-317.
68. Reddy M, G.S.S.R.P.A., *Preventing pressure ulcers: A systematic review.* JAMA: The Journal of the American Medical Association, 2006. **296**(8): p. 974-984.
69. Fulton, W.S. and R.T. Lipczynski. *Body-support pressure measurement using electrical impedance tomography*. in *Engineering in Medicine and Biology Society, 1993. Proceedings of the 15th Annual International Conference of the IEEE*. 1993.
70. Alirezaei, H., *A tactile distribution sensor which enables stable measurement under high and dynamic stretch 2009 IEEE Symposium on 3D User Interfaces*2009. 87.
71. katsuhiko Kanamori, H., Japan, *Pressure-sensitive electrically conductive elastomeric composition*, 1981, The Yokohama Rubber Co., Ltd., Tokyo, Japan: Japan. p. 11.
72. Alirezaei, H., A. Nagakubo, and Y. Kuniyoshi, *A highly stretchable tactile distribution sensor for smooth surfaced humanoids*, in *2007 7th IEEERAS International Conference on Humanoid Robots*2007, IEEE. p. 167-173.
73. Ahmed Elsanadedy, Y.M., Mojtaba Ahmadi, Andy Adler, *Characterisation of Conductive Polymer for EIT based Sensor*, in *Proceedings of the International Conference on Electrical and Computer Systems*2012: Ottawa, Ontario, Canada.
74. Yousef, H., M. Boukallel, and K. Althoefer, *Tactile sensing for dexterous in-hand manipulation in robotics—A review.* Sensors and Actuators A: Physical, 2011. **167**(2): p. 171-187.
75. Adler, A. and R. Guardo, *Electrical impedance tomography: regularized imaging and contrast detection.* Medical Imaging, IEEE Transactions on, 1996. **15**(2): p. 170-179.
76. Adler, A., R. Guardo, and Y. Berthiaume, *Impedance imaging of lung ventilation: do we need to account for chest expansion?* Biomedical Engineering, IEEE Transactions on, 1996. **43**(4): p. 414-420.
77. Barber DC, B.B., *Errors in reconstruction of resistivity images using a linear reconstruction technique.* Clin Phys Physiol Meas, 1988. **9**: p. 101-4.
78. Lionheart, W.R.B., *EIT reconstruction algorithms: pitfalls, challenges and recent developments.* Physiological Measurement, 2004. **25**(1): p. 125.

79. Griffiths, H. and Z. Zhang, *A dual-frequency electrical impedance tomography system.* Phys Med Biol, 1989. **34**(10): p. 1465-76.
80. Brown, B.H., A.D. Leathard, L. Lu, W. Wang, and A. Hampshire, *Measured and expected Cole parameters from electrical impedance tomographic spectroscopy images of the human thorax.* Physiological Measurement, 1995. **16**(3A): p. A57.
81. Vauhkonen M, *Electrical Impedance Tomography and Prior Information*, in *Department of Applied Physics*1997, Kuopio University.
82. Wijesiriwardana, R., T. Dias, and S. Mukhopadhyay. *Resistive fibre-meshed transducers*. 2003.
83. Soleimani, M., *Knitted switches for smart clothing using double electrode technology.* Sensor Review, 2008. **28**.
84. Vauhkonen, M., W.R.B. Lionheart, L.M. Heikkinen, P.J. Vauhkonen, and J.P. Kaipio, *A MATLAB package for the EIDORS project to reconstruct two-dimensional EIT images.* Physiological Measurement, 2001. **22**(1): p. 107-111.
85. Silvester, P.P. and R.L. Ferrari, *Finite elements for electrical engineers*. 3rd ed1996, New York: Cambridge University Press. xvi, 494 p.
86. Murai, T. and Y. Kagawa, *Electrical Impedance Computed Tomography Based on a Finite Element Model.* Biomedical Engineering, IEEE Transactions on, 1985. **BME-32**(3): p. 177-184.
87. Pilkington, T.C., M.N. Morrow, and P.C. Stanley, *A Comparison of Finite Element and Integral Equation Formulations for the Calculation of Electrocardiographic Potentials.* Biomedical Engineering, IEEE Transactions on, 1985. **BME-32**(2): p. 166-173.
88. Huebner KH, D.D., Smith DE, Byrom TG,, *The Finite Element Method for Engineers*. 4th ed2001: Wiley.
89. Bera, T.K. and J. Nagaraju. *A FEM-Based Forward Solver for Studying the Forward Problem of Electrical Impedance Tomography (EIT) with A Practical Biological Phantom*. in *Advance Computing Conference, 2009. IACC 2009. IEEE International*. 2009.
90. Cheney, M. and D. Isaacson, *Issues in electrical impedance imaging.* Computational Science & Engineering, IEEE, 1995. **2**(4): p. 53-62.
91. Holder, D., *Solving the forward problem: The finite element method*, in *Electrical impedance tomography: methods, history, and applications*2005, Taylor & Francis. p. 32-42.
92. Gagnon, H., M. Cousineau, A. adler, and A. Hartinger, *A Resistive Mesh Phantom for Assessing the Performance of EIT Systems.* Biomedical Engineering, IEEE Transactions on, 2010. **57**(99): p. 2257-2266.
93. Ross, A.S., G.J. Saulnier, J.C. Newell, and D. Isaacson, *Current source design for electrical impedance tomography.* Physiological Measurement, 2003. **24**(2): p. 509.
94. Al-Obaidi, A.A. and M. Meribout. *A new enhanced Howland voltage controlled current source circuit for EIT applications*. in *GCC Conference and Exhibition (GCC), 2011 IEEE*. 2011.
95. Filho, P.B., *Tissue Characterisation using an Impedance Spectroscopy Probe*, in *Department of Medical Physics and Clinical Engineering*2002, University of Sheffield.
96. Hongwei, H., M. Rahal, A. Demosthenous, and R.H. Bayford. *Floating voltage-controlled current sources for electrical impedance tomography*. in *Circuit Theory and Design, 2007. ECCTD 2007. 18th European Conference on*. 2007.
97. Charles F. Wojslaw, E.A.M., *Operational amplifiers: the devices and their applications*1985: John Wiley & Sons.
98. Khalighi, M., B. Vosoughi Vahdat, M. Mortazavi, M. Soleimani, and C.L. Yang, *A practical voltage-controlled current source design for electrical impedance tomography*, in *13th International Conference in Electrical Impedance Tomography (EIT 2012)*2012: Tianjin University, Tianjin, China.
99. AD844, *High Speed Monolithic Op Amp*, 2003, Analog Devices.
100. Pengpan, T., N.D. Smith, W. Qiu, A. Yao, C.N. Mitchell, and M. Soleimani, *A motion-compensated cone-beam CT using electrical impedance tomography imaging.* Physiological Measurement, 2011. **32**(1): p. 19.

101. Isaacson, D., *Distinguishability of Conductivities by Electric Current Computed Tomography.* Medical Imaging, IEEE Transactions on, 1986. **5**(2): p. 91-95.
102. Tao, X., *WoodHead Publishing, Cambridge*2005: WoodHead Publishing, Cambridge.
103. Teller, A., *A platform for wearable physiological computing.* Interacting with computers, 2004. **16**(5): p. 917.
104. Carpi, F. and D. De Rossi, *Electroactive Polymer-Based Devices for e-Textiles in Biomedicine.* IEEE transactions on information technology in biomedicine, 2005. **9**(3): p. 295-318.
105. Soleimani, M., *Electromechanical properties of wearable strain gauge transducers.* Electronics letters, 2008. **44**(21): p. 1236.
106. Ozanyan, K.B., *Guided-path tomography sensors for nonplanar mapping.* IEEE sensors journal, 2005. **5**(2): p. 167.
107. Tada, Y. and T. Yasunori, *A flexible and stretchable tactile sensor utilizing static electricity 2007 IEEE/RSJ International Conference on Intelligent Robots and Systems*2007. 684.
108. LR-SL-PA-10E5, *EEONTEX™ CONDUCTIVE STRETCHABLE FABRIC* 2009, Eeonyx corporation.
109. NW170-SL-PA-1500, *EEONTEX™ CONDUCTIVE NONWOVEN FABRIC*, 2009, Eeonyx Corporation.